OPTICAL SENSORS AND DEVICES BASED ON HIGHLY BIREFRINGENT MICRO/NANOFIBERS

JIN WA

Ph.D

The Hong Kong Polytechnic University

2014

The Hong Kong Polytechnic University

Department of Electrical Engineering

OPTICAL SENSORS AND DEVICES BASED ON HIGHLY BIREFRINGENT MICRO/NANOFIBERS

JIN WA

A thesis submitted in partial fulfillment of the requirements for the degree of Doctor of Philosophy

NOVEMBER 2013

CERTIFICATE OF ORIGINALITY

I hereby declare that this thesis is my own work and that, to the best of my knowledge and belief, it reproduces no material previously published or written, nor material that has been accepted for the award of any other degree or diploma, except where due acknowledgement has been made in the text.

__________(Signed)

JIN WA___(Name of Student)

Abstract

Optical micro/nanofibers (MNFs) have attracted significant attention recently for their potential applications in micro/nano-scale photonic systems. Various MNF devices have been reported, and most of them are based on MNFs with circular cross-sections. The circular MNFs have little or no capability of maintaining the state of polarization during transmission, which cause instability in phase and polarization sensitive devices and systems.

We proposed a simple and effective technique for fabricating air-cladding elliptical MNFs with wavelength and sub-wavelength scale diameters. The technique involves the use of a femtosecond infrared laser to cut away parts of the fiber cladding on opposite sides of a single mode fiber (SMF), and tapering-drawn the SMF by use of a flame-brushing technique. The cross-sectional shape of the “cut” region is well preserved during initial taper-drawn process and eventually turns to an approximately elliptical shape when it is drawn down to micrometer scales. These elliptical MNFs have demonstrated very large birefringence of the order of 10^{-2}, much larger than the conventional highly birefringent (Hi-Bi) fibers. The elliptical MNFs have SMF pigtails from which they are made, and hence can be easily integrated into conventional optical fiber systems with low loss.

We also explored the potential applications of the Hi-Bi MNFs. By splicing Hi-Bi MNFs into fiber Sagnac loops, all-fiber comb filters with flat-top passing bands are demonstrated. Two different configurations are studied, one incorporates a single piece of twisted Hi-Bi MNF in the Sagnac loop, while the other includes two pieces of Hi-Bi MNFs cascaded along a fiber with a rotation of their birefringence axes. The lengths of Hi-Bi MNFs used are on the order of centimeters, one to two orders of magnitude shorter than the conventional Hi-Bi fiber-based comb filters.

The birefringence of the MNFs may be tuned by varying the dimension of MNFs and the refractive index surrounding the MNFs, which provides more flexibility in designing comb-filter with desired properties. The comb filters might be used for multi-wavelength fiber lasers, optical signal processing and switching, and management for wavelength divided multiplexing networks, especially for photonic integration, computing, and nano-scale sensing.

Many device and sensor applications exploited the large external evanescent field associated with the thin MNF. However, the optical performance of MNFs quickly degrades after fabrication due to surface light scattering from dust particles and from cracks induced by water vapor, resulting in large irrecoverable increases in loss and eventual mechanical failure. We developed a technique to fabricate in-line fiber-optic photonic microcells by encapsulating MNFs with glass tubes. The encapsulation isolates MNFs from external contamination and makes them more robust for real-world applications. By splicing the encapsulated Hi-Bi MNFs into fiber Sagnac loops, gas pressure, temperature and refractive index sensors were developed. A Sagnac loop interferometer with a Hi-Bi MNF microcell demonstrated a refractive index sensitivity of ~2024 nm per refractive index unit (RIU) in gaseous environment (refractive index ~1) and 21231 nm/RIU when it is surrounded by water (refractive index ~1.33). Such microcells may be used as low loss evanescent-wave-coupled optical absorption and amplifying cells, as well as florescent and photo-acoustic cells.

Long period gratings (LPGs) exploit the resonant coupling between the fiber modes and have been studied extensively for sensing and communication applications. We fabricated LPGs directly on an encapsulated Hi-Bi MNF by periodically modifying the surface along one side of the MNF with a femtosecond laser. One such made LPG exhibits resonance dips at 1532.7 and 1614.2 nm for two orthogonal principal polarization states, and the corresponding grating strengths are

19.2 and 15.2 dB respectively. Higher order LPGs based on the encapsulated Hi-Bi MNF was also realized and used as a refractive index sensor in water with the sensitivity of ~4623 nm/RIU. We also fabricated LPGs by use of focused high frequency CO_2 laser pulses to periodically modify the transverse dimension of a bare Hi-Bi MNFs, and then encapsulated them within a glass capillary afterward. These LPGs may be used as robust wavelength selective polarization filters and sensors.

Polarization rocking filters (PRFs) are a special type of LPGs that couple light resonantly between two principle states of polarizations in a Hi-Bi fiber. They are essential functional components in guided wave optical systems such as polarization diversity heterodyne receivers and highly sensitive fiber sensors. We have successfully fabricated PRFs in Hi-Bi MNFs. A MNF with a slight ellipticity can have very large birefringence and hence much shorter polarization beat length than the conventional Hi-Bi fibers. This means that a smaller pitch or “rocking period” and hence shorter device length to produce reasonable polarization coupling. The PRFs were fabricated by introducing permanent twist at particular locations along the MNF by heating up the twisted fiber with a CO_2 laser. High polarization extinction of ~20 dB was achieved for a device length of 3.12 mm. A high order PRF was tested for refractive index sensing and demonstrated a refractive index sensitivity of 32036 nm/RIU.

Publications

Journal articles

1. W. Jin, H. Xuan, and W. Jin, "Robust microfiber photonic microcells for sensor and device applications," Opt. Express (accepted).
2. W. Jin, H. Xuan, and W. Jin, "Structural polarization-rocking filters in highly birefringent microfibers," Opt. Lett., Vol. 39, pp. 3363-3366 (2014).
3. W. Jin, H. Xuan, W. Jin, and L. Jin, "Rocking long period gratings in single mode fibers," J. Lightwave Technol., Vol.31, pp.3117-3122 (2013).
4. W. Jin, C. Wang, H. Xuan, and W. Jin, "Tunable comb filters and refractive index sensors based on fiber loop mirror with inline high birefringence MNF," Opt. Lett., Vol. 38, pp. 4277-4280 (2013).
5. H. Xuan, J. Ma, W. Jin, and W. Jin, "Polarization converters in highly birefringent microfibers," Opt. Express, Vol. 22, pp. 3648-3660 (2014).

Conference proceedings

1. W. Jin, H. F. Xuan, and W. Jin, “Long period grating made by rocking a single mode fiber,” OFS2012 22nd International Conference on Optical Fiber Sensors, Beijing, Proc. SPIE 8421, 84214X (17 October 2012); DOI:10.1117/12.975115.
2. W. Jin, H. F. Xuan, and W. Jin, “Birefringent microfiber-based fiber loop mirrors for tunable filters and refractive index sensors,” Fifth European Workshop on Optical Fibre Sensors, Krakow, Proc. SPIE 8794, 87943W (May 20, 2013), DOI: 10.1117/12.2026655.
3. W. Jin, H. F. Xuan, and W. Jin, “High Sensitivity pressure Sensor Based on Birefringent Microfiber Loop Mirrors,” Fourth Asia Pacific Optical Sensors Conference, Wuhan, Proc. SPIE 8924, 89242Z (October 15, 2013); DOI:10.1117/12.2036196.

4. W. Jin, H. F. Xuan, and W. Jin, “Long period gratings in highly birefringent microfibers, ” 23rd International Conference on Optical Fibre Sensors, Stander, Proc. SPIE 9157, 91577N (June 2, 2014); doi:10.1117/12.2059025.
5. H. Xuan, W. Jin, J. Ma, and W. Jin, “Polarization converters based on elliptical micro/nano optical fibers,” 2013 International Conference on Optical Instruments and Technology: Optical Sensors and Applications, Beijing, Proc. SPIE 9044, 904403 (December 20, 2013); DOI:10.1117/12.2037474.
6. C. Wang, W. Jin, W. Jin, J. Ma, H. L. Ho., “Highly birefringent suspended core photonic microcells for sensing applications,” 23rd International Conference on Optical Fibre Sensors, Stander, Proc. SPIE 9157, 915776 (June 2, 2014); DOI:10.1117/12.2059320.
7. C. Wang, W. Jin, J. Ma, W. Jin, H. L. Ho., “Photonic microcells for novel devices and sensor applications,” Fourth Asia Pacific Optical Sensors Conference, Wuhan, Proc. SPIE 8924, 892427 (15 October 2013); DOI: 10.1117/12.2036195.

Acknowledgements

First and foremost, I would like to show my deepest gratitude to my supervisor, Dr. Wei Jin, a respectable, responsible and resourceful scholar, who has provided me with valuable guidance in every stage of my research works. Without his enlightening instruction, impressive kindness and patience, I could not have completed my research work. His keen and vigorous academic observation enlightens me not only in my research work but also in my future study.

I shall extend my thanks to Dr. Xuan for all his kindness and help in developing the fundamental and essential academic competence. I would also like to thank all my colleagues who have helped me a lot in conducting experiments and preparing my thesis and presentation.

I would also like to give my thanks to my beloved family. The endless support and care from my parents makes me full of gratitude. The encouragement from my family, gives me the biggest confidence and motivation.

Contents

List of Figures

Chapter 1

Introduction

1.1 Literature review

Mirco/nanofibers (MNFs) refer to a class of optical fibers with diameters ranging from a few hundred nanometers to a few micrometers. An optical microfiber (MF) typically has micron size diameter, and a MNF with a diameter significantly less than one micron is often called a nanofiber (NF) [1]. The researches in the fabrication, characterization, and applications of MNFs may be resulted in novel applications such as wavelength-scale light transmission and interconnection which are useful for photonic integration, computing, and nano-scale sensing.

1.1.1 Fiber tapering techniques

Generally, MNFs have been fabricated from conventional single mode fibers (SMFs) by use of flame-assisted [2, 3], CO_2 laser assisted [4], or a two-step tapering-drawing process [5], so called "heating and stretching" method [5, 6] where the fiber is locally heated and then axially stretched. The heated region would experience a diameter decrease due to the mass conservation.

In the "flame-brushing" method [2, 3], a hydrogen gas torch is usually used due to its cleanness, easy control and high temperature. Fig. 1.1 shows a schematic illustration of the tapered fiber fabrication based on the flame brushing technique. A coating length of several centimeters is removed from the SMF prior to the fabrication of the tapered fiber, then the fiber is clamped horizontally on the translation stage, held by two fiber holders and heated by a high temperature gas flame. During the tapering, the torch moves and heats along the uncoated segment of the fiber while the two translation stages moving to the opposite direction. The moving torch provides a uniform heat to the fiber and the tapered fiber is produced with good uniformity along the heat region.

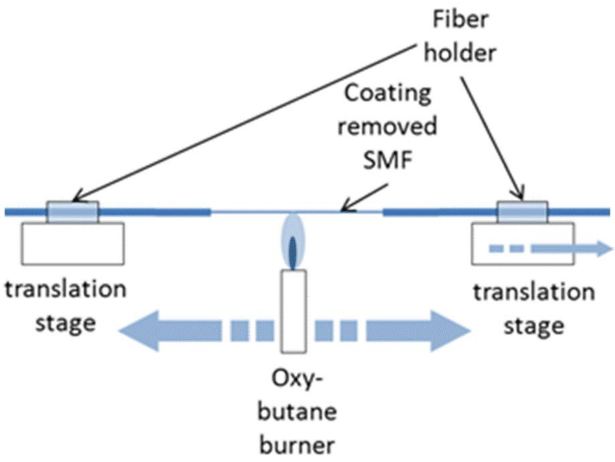

Fig. 1.1 Tapered fiber fabrication using flame brushing technique [3]

Later, a carbon dioxide laser beam replaced hydrogen gas torch as a heating source and was used to fabricate the MNF [4], which employs a sapphire tube (microfurnace) heated by a CO_2 laser. Because the tapers were short, having lengths of a few millimeters, they were convenient for bending and looping of the MNFs in free space. This approach can reduce or eliminate the 1380-nm-wavelength OH absorption in tapered fibers, as well as avoid contamination and random turbulence-induced nonuniformity of a flame-heated system.

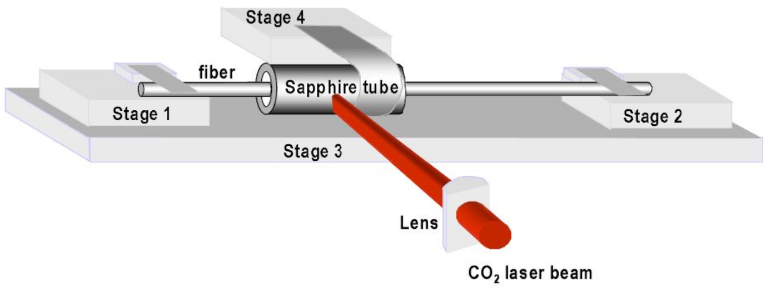

Fig. 1.2 Illustration of the setup for drawing MNF using a sapphire tube heated with a CO_2 laser [4].

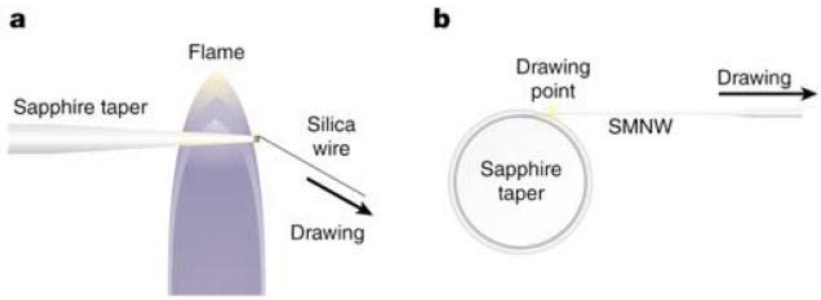

Fig. 1.3 The second step in the fabrication process of silica sub-micrometer and nanometer wires [5].

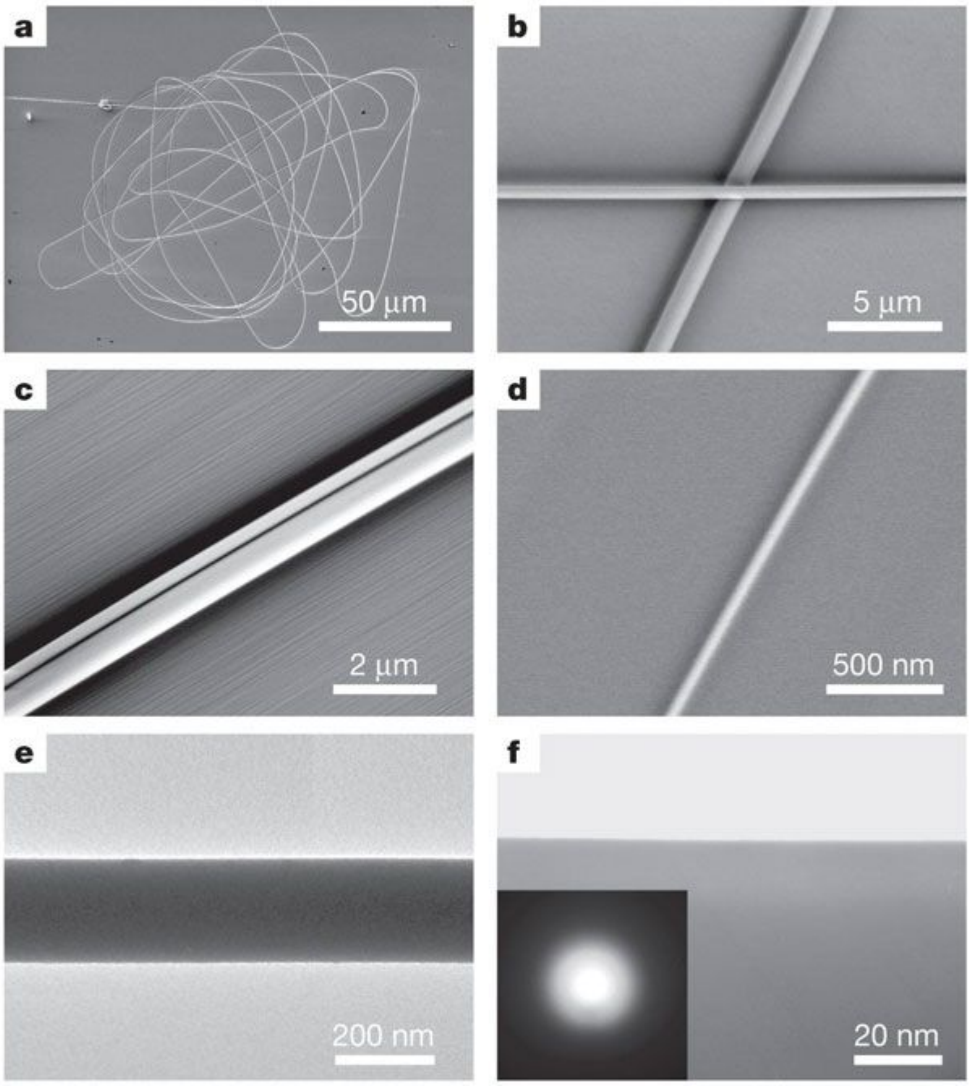

Fig. 1.4 SEM images of the MNFs drawn by two-step method [5].

In the two-step drawing process [5], as shown in Fig. 1.3, first, a silica fiber was drawn to a micrometer-diameter wire with a flame. Second, to obtain a steady temperature distribution in the drawing region while further reducing the wire diameter, a tapered sapphire fiber with a tip diameter of about 80 mm was used to absorb the thermal energy from the flame. One end of a micrometer-diameter silica wire was placed horizontally, then the sapphire tip was rotated around its axis of symmetry to wind the silica wire around the tip. The wire coil was moved about 0.5 mm out of the flame to prevent melting and the wire was then drawn perpendicular to the axis of the sapphire tip in the horizontal plane to form a MNF. Using this technique, silica MNFs with diameters down to 50 nm was obtained with lengths up to tens of millimeters, as shown in Fig. 1.4.

1.1.2 MNF-based devices and sensors

When the diameter of the MNF decreases, the whole tapered fiber can be considered as the fiber core and the Ge-doped core can be negligible, while the environment such as air is usually used as cladding. This structure introduces some unique optical and mechanical properties, such as strong confinement [7,8], a larger evanescent field [4, 9-14], great configurability [4,15], low loss and easy availability [16].

The potential applications of the MNFs can be widespread. Various MNF-based photonic devices have been reported [17-30]. Typical structures of optical MNF sensors introduced in this paper are illustrated in Fig. 1.5 [31].

Fig. 1.5 (a) depicts the simplest uncoated MNF sensor, in which the diameter of the MNF is usually close to or less than the wavelength of light. Due to the high fractional guiding mode of the MNF outside the fiber, transmission intensity of the MNF depends on the properties of the ambient medium surrounding the MNF, which has been applied for refractive index (RI), humidity, and chemical/biological sensing. In addition, the surface of MNF can be coated with reagents for wider sensing applications. Fig. 1.5 (b) illustrates a tapered fiber tip sensor, which is usually coated with a sensitive film to identify chemical or biological species. It has been used for RI sensing and some fluorescence based chemical/biological sensing. Fig. 1.5 (c) illustrates evanescent coupled nanowire-MNF sensor, which is in principle similar to Fig. 1.5 (a), but offers more flexibility for functionalizing the sensing elements, and has been applied to polymer or semiconductor nanowire optical sensors. While sensors in Fig. 1.5 (a)-(c) employ intensity-dependent scheme, those in Figs. 1.5 (d)-(f) depend on optical phase or path. Fig. 1.5 (d) shows a sensing structure relying on nanowire-MNF Mach-Zehnder interferometer (MZI). Fig. 1.5 (e) illustrates optical sensors based on MNF loop/knot/coil resonators that are assembled by micromanipulation. Fig. 1.5 (f) shows a liquid-core optical ring-resonator sensor using a MNF for input and output connections [31].

Besides exploiting the strong external evanescent field of the MNFs and taking advantage of the strong interaction of the evanescent field with environment or evanescent coupling between waveguides, some researches have been conducted on MNF in-line mode-coupling devices, such as Fiber Bragg Gratings (FBGs) [32] and long period gratings (LPGs) [33, 34], both of which can be used as the basic element in photonic systems or sensing applications.

However, the MNFs reported so far are taper-drawn directly from standard signal mode fibers (SMFs) or glass rods. They are typically not Hi-Bi and hence have little or no capability of maintaining the state of polarization during transmission, a crucial factor that determines the stability of phase sensitivity devices and sensors[35].

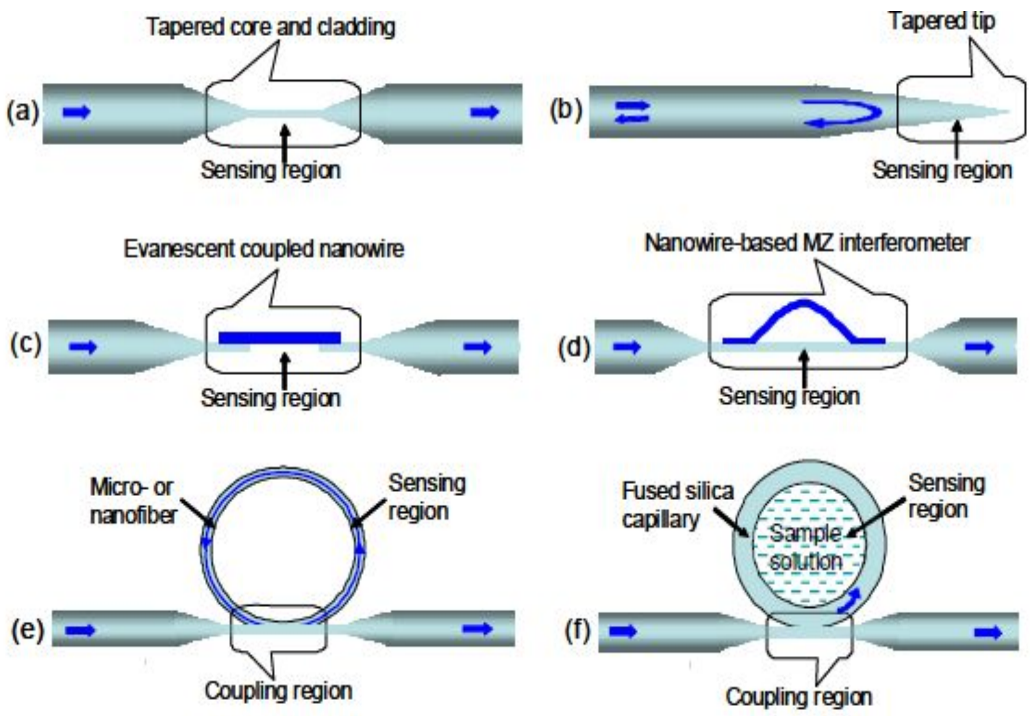

Fig. 1.5 Illustration of typical structures of optical MNF sensors: (a) straight MNF sensor, (b) tapered tip MNF sensor, (c) evanescent coupled nanowire MNF sensor, (d) nanowire-based MZI MNF sensor, (e) MNF loop/knot/coil resonator sensor, and (f) liquid-core optical ring-resonator sensor [31].

1.2 Motivation and contribution

In the structure where a perfect circular fiber cladding with perfect circular fiber core is present, the fundamental mode has two degenerate modes, which are orthogonally polarized and have the same propagation constant. Various imperfections in practical single-mode fibers result in an anisotropy of the fiber. These imperfections can be attributed to a noncircular core, asymmetrical lateral stress or external conditions such as bending, twist and tension. In general, this unpredictable birefringence introduced by these imperfections is not desirable. One method to control the output of the polarization is deliberately inducing predictable birefringence.

In this thesis, we refer a Hi-Bi MNFs, which have very high birefringence induced by elliptical geometry. As known, MNFs have been fabricated from conventional silica optical fibers. However, they are typically not highly birefringent (Hi-Bi) and hence have little or no capability of maintaining the state of polarization during transmission, a crucial factor that determines the stability of phase sensitivity devices and sensors. In this study, in-line Hi-Bi MNF is utilized. This air-cladding Hi-Bi elliptical-shaped MNF [35] has a high birefringence up to the order 10^{-2}, which is much bigger than conventional polarization maintaining fibers, and the birefringent MNFs can be designed with desired properties, and some optical devices and sensors based on the Hi-Bi MNFs were developed.

Based on the fabricated Hi-Bi MNFs which combine the unique properties of MNFs and polarization maintaining fibers, we explored some application based on the Hi-Bi MNFs, including interferometric comb filters and sensors, and mode coupling devices.

1.2.1 Comb Filters

The straightforward application of a Hi-Bi fiber is to form a comb filter by splicing it into a Sagnac loop, in which a path imbalance is introduced between the light that propagates along different polarization eigen-axis and an interferometric channeled spectrum is observed [36]. It has been intensively developed and commonly used for many applications such as in all-optical signal processing and multi-wavelength fiber lasers [37-39], because they have the advantages of low loss, small size, polarization independence, simple construction and better performance compared with conventional optical filters [40-42]. A Sagnac loop interferometer with one-stage Hi-Bi MNF is proposed in this work as a simple comb filter device, with a high birefringence, and hence shorter device length, can be used as the basic elements in micro/nano photonics, which focuses on micro photonic circuits composed of MNFs [43-45].

In this paper, the Sagnac loop interferometer with one section and two-stage Hi-Bi MNFs are proposed and the characteristics of the Sagnac loop interferometers are investigated both theoretically and experimentally. The Sagnac loop interferometer with one section of Hi-Bi MNF was used to measured the group birefringence of the Hi-Bi MNF fabricated, the obtained experimental data agrees well with the numerical simulation, while Sagnac loop interferometer using two-stage Hi-Bi MNFs that are connected together at different angle of rotation in relation with the birefringence axes instead of one section of Hi-Bi MNF allows more flexibility in controlling the transmission/reflection characteristics of the comb filters. The length of Hi-Bi MNFs is on the order of centimeters, one or even two orders of magnitude shorter than the conventional Hi-Bi fiber-based Sagnac loop interferometer devices, and a flat-top comb filter was obtained. The filter with the flat-top pass-band bandwidth is preferred for signal fidelity and tolerance of signal wavelength drift which can relax the requirements on wavelength control in DWDM system [46].

1.2.2 Robust MNF microcells for sensors

The MNFs have a large evanescent field outside the fiber, allowing strong evanescent-wave coupling between MNFs and their environment, and hence the straightforward applications based on this properties are evanescent-wave sensors [47, 48], which can be used for chemical and biological sensing in medical, industrial and environmental applications.

However, the challenge of these applications is that the MNF is fragile and easily contaminated. There are many activities on the method and the effect of embedding or preservation of MNF devices in order to improve robustness, stability and to provide reliable protection against degradation [49-51]. However, these methods are complicated and it is difficult to operate.

In this paper, we report simple, low cost, and effective method for fabricating encapsulated MNF photonic microcells (PMCs).The MNFs are made by bi-tapering a conventional single mode fiber (SMF) and suspended along the center area of a capillary tube. The MNFs are kept straight within the capillary while their SMF pigtails are glued to the two ends of the capillary. The encapsulation does not change the optical property of the MNF but the capillary tube protests the MNF from external disturbance and contamination. Side holes are made on the capillary wall and act as ingress/egress channels for sample liquids or gases. The PMCs of such made are robust and stable, and can be easily integrated into standard fiber-optic circuits with low loss, making the MNF-based devices more practical for real-world applications.

Due to two different polarization modes of Hi-Bi fiber exhibiting different responses to temperature, strain, and refractive index [52,53], Sagnac loop interferometer based Hi-Bi fiber has been shown to be an attractive device for optical fiber sensing [54] for possessing many advantages including simple design, ease of manufacture, high sensitivity and low cost. Besides the gyroscope application[55], the Sagnac loop interferometer has been used as temperature sensors[56, 57], strain sensors [58-61] and and bio-chemical sensors [62, 63]. In this work, the photonic microcells with Hi-Bi MNFs as polarimetric interference elements were spliced into a Sagnac loop interferometer system for high sensitive gas pressure, temperature and refractive index sensing.

1.2.3 Long period gratings and polarization rocking filters

Long period gratings (LPGs) are probably one of the most important in-line fiber devices that have widespread applications in the telecommunication and sensing fields. The theory, fabrication, and applications of LPGs may be found in a number of excellent textbooks/review papers[64-66]. The applications of LPGs include wavelength filters, mode-converters, spectrum flatteners, gain equalizers, and various types of sensors.

LPGs have been fabricated in both the standard telecommunication fibers, microstructured optical fibers, and MNFs with various fabrication techniques such as the traditional UV-writing technique, femtosecond laser (UV and IR) writing techniques, CO_2 laser irradiation, arc-discharge, chemical etching, and periodic mechanical stress techniques[65-75], however, there is no work on LPGs fabrication in the Hi-Bi MNFs. In this dissertation, we inscribed long period grating using two methods, IR femtosecond laser writing techniques, and CO_2 laser irradiation. These gratings can be used as wavelength selective polarization filters, sensors and so on.

Polarization-rocking filters (PRFs) are a special type of LPGs that couple light resonantly between the two principal states of polarization in Hi-Bi fibers. PRFs have been made in Ge-doped D-shaped and elliptical-core polarization-maintaining fibers by photoinducing, through an external UV-writing technique, periodic birefringent gratings along the length of the fibers [76, 77]; and in Hi-Bi photonic crystal fibers (PCFs) by periodic twist of the birefringent axis of the fibers through a CO_2 laser-assisted [78] and an arc fusion splicer-assisted technique [79]. The responses of PRFs to strain, temperature, and hydrostatic pressure have been studied [77, 79]. There are also reports on the use of PRFs as polarization-mode couplers to form Mach-Zehnder type fiber interferometers(i.e., in-line polarimeters) for temperature sensors [81], and on simultaneous strain and temperature sensing with a PRF in combination with a fiber Bragg grating(FBG) [81]. A study on the dispersive properties of a PRF in a Hi-Bi PCF was also carried out and shows that the formation of a PRF gives more flexibility in dispersion engineering, which cannot be achieved easily by designing the fiber alone [82]. However, all the PRFs and related devices reported so far are made in normal size optical fibers and there is no report on PRFs made on MNFs to our knowledge.

For elliptical MNFs, the birefringence is estimated to be between 10^{-3} and 10^{-2}, which corresponds to polarization beat lengths of a few hundreds of micrometers. Considering the facts that high quality PRFs have been made in normal-size Hi-Bi PCFs with a CO_2 laser-assisted or arc fusion splicer-assisted point-by-point technique to periodically twist the fibers [78, 79], and the twist angle can be as large as 5° over a twist length of ~30 μm [79], we fabricate PRFs in Hi-Bi MNFs with CO_2 laser irradiation with much shorter device length, and explore its applications.

1.3 Thesis outline

The thesis structure is arranged as follows:

Chapter 1 We review the background and applications of Hi-Bi fibers and MNFs from three different main lines: the development of Hi-Bi fibers, the invention and applications of MNFs, and in-line devices in MNFs. Then the motivation and contribution of this thesis is discussed followed by the thesis structure.

Chapter 2 In this chapter, we will introduce the principle of Hi-Bi MNF in detail. Empirical formulas that relate the higher order mode cutoff and the maximum birefringence with ellipticity, and that determine peak birefringence wavelength for a given fiber dimension are obtained. These results will be important for the design of highly birefringent MNFs with desired properties.

Chapter 3 We have analyzed Sagnac loop interferometers based on Hi-Bi fibers theoretically and experimentally. The Sagnac loop interferometers with one section of Hi-Bi MNFs as the simplest comb filters were used to measure the group birefringence of Hi-Bi MNFs fabricated in chapter 2, and the Sagnac loop interferometers containing two cascaded Hi-Bi MNFs were developed for flat-top comb filters.

Chapter 4 In this chapter, We report the fabrication of in-line photonic microcells by encapsulating tapered microfibers (MFs) inside glass tubes. The encapsulation isolates MFs from external environment and makes them more suitable for real-world applications. Based on the encapsulated Hi-Bi MNFs photonic microcells, we demonstrated gas pressure, temperature and refractive index (RI) sensors.

Chapter 5 Coupling between guided modes in MNFs are realized by fabricating LPGs along the MNFs. The Hi-Bi MNF LPGs are fabricated by periodically inducing micro-tapers along the MNF by use of focused pulsed CO_2-laser, and periodically modifying the surface along one side of the fiber with a femtosecond laser, demonstrating a polarization selected resonant dip, and as a refractive index sensor with high sensitivity.

Chapter 6 We proposed a special grating based on Hi-Bi MNFs, polarization rocking filters, which were fabricated in experiments by inducing permanent twist with scanning a CO_2 laser beam transversely across the MNF while it is being twisted alternatively, and the potential sensing applications were explored.

Chapter 7 The conclusion of the whole work will be drawn and future work will be suggested in this chapter.

1.4 Summary

In this chapter, we mainly introduced the background knowledge of this dissertation, mainly introduce the potential applications of Hi-Bi MNF and the contributions of this work. The main motivation of this thesis is demonstrated and the outline for each specific chapter is listed.

References of Chapter 1

1. M. Sumetsky, “Optical micro- and nanofibers for sensing applications,” Micro (MEMS) and Nanotechnologies for defense and security, edited by T. George, and Z. Cheng, Proc. of SPIE Vol. 6556, 65560J-1-65560J-11 (2008).

2. Brambilla, G., V. Finazzi, and D. Richardson, “Ultra-low-loss optical fiber nanotapers,” Opt. Express., Vol. 12, pp. 2258-2263 (2004).
3. K. S. Lim, S. W. Harun, H. Arof and H. Ahmad “Fabrication and Applications of MNF,” Selected Topics on Optical Fiber Technology, Dr Moh. Yasin (Ed.), ISBN: 978-953-51-0091-1, InTech, DOI: 10.5772/31123 (2012).
4. M. Sumetsky, Y. Dulashko, and A. Hale, "Fabrication and study of bent and coiled free silica nanowires: Selfcoupling microloop optical interferometer," Opt. Express, Vol. 12, pp. 3521-3531 (2004).
5. L. M. Tong, R. R. Gattass, J. B. Ashcom, S. L. He, J. Y. Lou, M. Y. Shen, I. Maxwell, and E. Mazur, “Subwavelength-diameter silica wires for low-loss optical wave guiding,” Nature,Vol. 426, pp. 816-819 (2003).
6. L. Tong, J. Lou, Z. Ye, G. T. Svacha, and E. Mazur, “Self-modulated taper drawing of silica nanowires,” Nanotechnology, Vol.16, 1445-1448 (2005).
7. S. G. Leon-Saval, T. A. Birks, W. J. Wadsworth and P. St.J. Russell, “Supercontinuum generation in submicron fibre waveguides,” Opt. Express, Vol. 12, pp. 2864-2869 (2004).
8. M. A. Foster, J. M. Dudley, B. Kibler, Q. Cao, D. Lee, R. Trebino and A. L. Gaeta, "Nonlinear pulse propagation and supercontinuum generation in photonic nanowires: Experiment and simulation", Appl. Phys. B: Lasers and Optics, vol. 81, pp. 363–367 (2005).
9. V. I. Balykin, K. Hakuta, Fam Le Kien, J. Q. Liang, and M. Morinaga, “Atom trapping and guiding with a subwavelength-diameter optical fiber,” Physical Review A, Vol. 70, ar. 011401 (2004).
10. G. Brambilla, G. S. Murugan, J. S. Wilkinson, and D. J. Richardson, “Optical manipulation of microspheres along a subwavelength optical wire,” Opt. Lett., Vol. 32, pp. 3041－3043 (2007).
11. J. Villatoro, and D. Monzón-Hernández, “Fast detection of hydrogen with nano

fiber tapers coated with ultra thin palladium layers," Opt. Express, Vol. 13, pp. 5087–5092 (2005).

12. F. Xu, P. Horak, and G. Brambilla, "Optical MNF coil resonator refractometric sensor," Opt. Express, Vol. 15, pp. 7888-7893 (2007).
13. M. Sumetsky, "Optical fiber microcoil resonator," Opt. Express, Vol. 12, pp. 2303-2316 (2004).
14. F. Xu, and G. Brambilla, "Embedding optical MNF coil resonators in Teflon," Opt. Lett., Vol.32, 2164-2166 (2007).
15. M. Sumetsky, Y. Dulashko, J. M. Fini and A. Hale "Optical MNF loop resonator" Appl. Phys. Lett., Vol. 86, pp. 161108-1-161108-3 (2005).
16. G. Brambilla, F. Xu, P. Horak, Y. Jung, F. Koizumi, N. P. Sessions, E. Koukharenko, X. Feng, G. S. Murugan, J. S. Wilkinson, and D. J. Richardson, "Optical fiber nanowires and microwires: fabrication and applications," Adv. Opt. Photon., Vol. 1, pp. 107-161 (2009).
17. L. M. Tong, R. R. Gattass, J. B. Ashcom, S. L. He, J. Y. Lou, M. Y. Shen, I. Maxwell, and E. Mazur, "Subwavelength-diameter silica wires for low-lossoptical wave guiding," Nature, Vol. 426, pp.816-819 (2003).
18. A. ryanfar, K.-S. Lim, W.-Y.Chong, S. W. Harun, H. Ahmad, "Add-Drop Filter Based on MNF Mach Zehnder/Sagnac Interferometer," IEEE J. Quantum Electron., Vol.48, pp.1411-1414 (2012).
19. S. S. Wang, Z. F. Hu, Y. H. Li, and L. M. Tong, "All-fiber Fabry-Perot resonators based on MNF Sagnac loop mirrors," Opt. Lett., Vol. 34, pp. 253-255 (2009).
20. A. A. Jasim, S. W. Harun, H. Arof, and H. Ahmad, "Inline MNF Mach-Zehnder interferometer for high temperature sensing," IEEE Sensors J., Vol. 13, pp. 626–628 (2013).
21. W. Fan, J. L. Gan, Z. S. Zhang, X. M. Wei, S. H. Xu, and Z. M. Yang, "Narrow

linewidth single frequency MNF laser," Opt. Lett., Vol. 37, pp. 4323–4325 (2012).

22. P. Polynkin, A. Polynkin, N. Peyghambarian, and M. Mansuripur, "Evanescent field-based optical fiber sensing device for measuring the refractive index of liquids in microfluidic channels," Opt. Lett., Vol.30, pp. 1273-1275 (2005).
23. J. Villatoro, V.P. Minkovich, D. Monzo´ n-Herna´ ndez, "Temperature -independent strain sensor made from tapered holey optical fiber," Opt. Lett., Vol. 31, pp. 305-307 (2006).
24. S. G. Leon-Saval, T. A. Birks, W. J. Wadsworth and P. St. J. Russell, "Supercontinuum generation in submicron fiber waveguides," Opt. Express, Vol. 12, pp. 2864-2869 (2004).
25. V. I. Balykin, K. Hakuta, Fam Le Kien, J. Q. Liang, and M. Morinaga, "Atom trapping and guiding with a subwavelength-diameter optical fiber," Physical Review A, Vol. 70, ar. 011401 (2004)
26. E. C. Mägi, H. C. Nguyen, and B. J. Eggleton, "Air-hole collapse and mode transitions in microstructured fiber photonic wires," Opt. Express, Vol. 13, 453-459 (2005).
27. G. Brambilla, V. Finazzi and D.J. Richardson, "Ultra-low-loss optical fiber nanotapers," Opt. Express, Vol. 12, pp. 2258-2263 (2004).
28. M. Sumetsky, Y. Dulashko, and A. Hale, "Fabrication and study of bent and coiled free silica nanowires: Self-coupling microloop optical interferometer," Opt. Express, Vol. 12, pp. 3521–3531 (2004).
29. P. Pal and W. H. Knox, "Low loss fusion splicing of micron scale silica fibers," Opt. Express, Vol.16, pp. 11568–11573 (2008).
30. P. Pal, and W. H. Knox, "Fabrication and Characterization of Fused MNF Resonators," IEEE Photon. Technol. Lett., Vol. 21, pp. 766–768 (2009).
31. L. Zhang, J.Y. Lou, L.M. Tong, "MNF optical sensors," Photonic Sens. ,Vol.1,

pp. 31–42 (2011).

32. X. Fang, C. Liao, and D. Wang, "Femtosecond laser fabricated fiber Bragg grating in MNF for refractive index sensing," Opt. Lett., Vol. 35, pp. 1007-1009 (2010).
33. H. F. Xuan, W. Jin, and S. J. Liu, “Long-period gratings in wavelength-scale MNFs,” Opt. Lett., Vol. 35, pp. 85–87 (2010).
34. H. F. Xuan, W. Jin, and M. Zhang, “CO_2 laser induced long period gratings in optical MNFs,” Opt. Express , Vol. 17, pp. 21882–21890 (2009).
35. H. Xuan, J. Ju, and W. Jin, “Highly birefringent optical MNFs” Opt. Express, Vol. 18, pp. 3828-3839 (2010).
36. Chun-Liu Zhao, X. Yang, C. Lu, W. Jin, M.S. Demokan, “Temperature-insensitive interferometer using a highly birefringent photonic crystal fiber loop mirror,” IEEE Photon. Technol. Lett., Vol. 16, pp. 2535-2537 (2004).
37. Wu, J.-W., X.-D. Tian, and H.-B. Bao, “A designed model about amplification and compression of picosecond pulse using cascaded soa and NOLM device," *Progress In Electromagnetics Research* PIER, Vol. 76, pp.127-139 (2007).
38. C.-H. Chang, H. Lin, Y.-S. Huang, and S.-H. Tong, “Multi-wavelength-switchable and uniform erbium-doped fiber laser using unbalanced in-line Sagnac interferometer,” Opt. Express., Vol. 15, pp. 12450-12456 (2007).
39. Hu, S., L. Zhan, Y. J. Song, W. Li, S. Y. Luo, and Y. X. Xia, “Switchable multiwavelength erbium-doped fiber ring laser with a multisection high-birefringence fiber loop mirror," *IEEE Photon.Technol. Lett*., Vol. 17, 1387-1389 (2005).
40. Jinno, M. and T. Matsumoto, “Nonlinear Sagnac interferometer switch and its applications," *IEEE J. Quantum Electron.*, Vol. 28, pp. 875-882 (1992).

41. M. A. Mirza and G. Stewart, “Theory and design of a simple tunable Sagnac loop filter for multiwavelength fiber lasers,” Appl. Opt., Vol. **47**, pp. 5242-5252 (2008).

42. E. A. Kuzin, N. Korneev, J.W. Haus, and B. Ibarra-Escamilla, “Polarization independent nonlinear fiber sagnac interferometer,” Opt. Commun., Vol. 183, pp. 389-393 (2000).

43. M. Sumetsky, “Basic elements for MNF photonics: MNFs and MNF coil resonators,” J. Lightwave Technol., Vol. **26**, pp. 21–27 (2008).

44. L. M. Tong, R. R. Gattass, J. B. Ashcom, S. L. He, J. Y. Lou, M. Y. Shen, I. Maxwell, and E. Mazur, “Subwavelength-diameter silica wires for low-loss optical wave guiding,” Nature 426 (6968), pp. 816–819 (2003).

45. L. M. Tong, J. Y. Lou, R. R. Gattass, S. L. He, X. W. Chen, L. Liu, and E. Mazur, “Assembly of silica nanowires on silica aerogels for microphotonic devices,” Nano Lett., Vol. **5**, pp. 259–262 (2005).

46. Y. W. Lee, H. T. Kim, J. Jung, and B. H. Lee,“Wavelength-switchable flat-top fiber comb filter based on a Solc type birefringence combination,” Opt. Express 13(3), 1039–1048 (2005).

47. L. M. Tong, J. Y. Lou, and E. Mazur, “Single-mode guiding properties of subwavelength-diameter silica and silicon wire waveguides,” Opt. Express, Vol. 12, pp.1025–1035 (2004).

48. J. Villatoro, and D. Monzón-Hernández, “Fast detection of hydrogen with nano fiber tapers coated with ultra thin palladium layers,” Opt. Express, Vol. 13, pp. 5087–5092 (2005).

49. L. Tong, J. Lou, R. R. Gattass, S. He, X. Chen, L. Liu, E. Mazur, “Assembly of silica nanowires on silica aerogels for microphotonic devices,” Nano Lett., Vol. 5, pp. 259–262 (2005).

50. F. Xu, and G. Brambilla, “Preservation of micro-optical fibers by embedding,”

Jpn. J. Appl., Vol.47, pp. 6675-6677, (2008).

51. G. Vienne, Y. H. Li, L. M. Tong, “Effect of host polymer on MNF resonator”, IEEE Photon. Technol. Lett., Vol. 19, pp. 1386–1388, (2007).
52. O. Frazao, B.V. Marques, P. Jorge, J.M. Baptista, and 1.L. Santos, “High birefringence D-type fiber loop mirror used as refractometer,” Sensor and Actuators B: Chemical, vol. 135, pp. 108-111 (2008).
53. C.L. Zhao, L.R. Zhao, W. Jin, J. Ju, L. Cheng, and X.G. Huang, “Simultaneous strain and temperature measurement using a highly birefringence fiber loop mirror and a long-period grating written in a photonic crystal fiber,” Optics Communication, Vol. 282, pp. 4077-4080 (2009).
54. V. Vali and R. W. Shorthill, “Fiber ring interferometer,” Appl. Opt., Vol. 15, pp. 1099–1100 (1976).
55. B. Culshaw, “The optical fiber Sagnac interferometer: An overview of its principles and applications,” Meas. Sci. Technol., vol. 17, pp. R1–R16, (2006).
56. E. De la Rosa, L. A. Zenteno, A. N. Starodumov, and D. Monzon, “All-fiber absolute temperature sensor using an unbalanced high-birefringence Sagnac loop,” Opt. Lett., vol. 22, pp. 481–483 (1997).
57. Y. Yu, X. Li, X. Hong, Y. 4.Deng, K. Song, Y. Geng, H. Wei, and W. Tong, “Some features of the photonic crystal fiber temperature sensor with liquid ethanol filling,” Opt. Exp., vol. 18, pp. 15383–15388, (2010).
58. M. Campbell, G. Zheng, A. S. Holmes-Smith, and P. A. A. Wallace, “Frequency-modulated continuous wave birefringent fiber-optic strain sensor based on a Sagnac ring configuration,” Meas. Sci. Technol., vol.10, pp. 218–224 (1999)
59. X. Y. Dong, H. Y. Tam, and P. Shum, “Temperature-insensitive strain sensor with polarization-maintaining photonic crystal fiber based Sagnac interferometer,” Appl. Phys. Lett., vol. 90, pp. 151113-1–151113-3, (2007).

60. J. Villatoro, V.P. Minkovich, D. Monzo´ n-Herna´ ndez, “Temperature-independent strain sensor made from tapered holey optical fiber,” Opt. Lett., Vol. 31, Issue 3, pp. 305-307 (2006).
61. C. Shen, C. Zhong, J. Chu, X. Zou, Y. Jin, J. Wang, X. Dong, Y. Li, L. Wang, and C. Shen, “Temperature-insensitive strain sensor using a fiber loop mirror based on low-birefringence polarization-maintaining fibers ”, Opt. Commun., Vol. 287, pp. 31-34, (2013).
62. Chun-Liu Zhao, X. Yang, C. Lu, W. Jin, M.S. Demokan, “Temperature-insensitive interferometer using a highly birefringent photonic crystal fiber loop mirror,” IEEE Photon. Technol. Lett., Vol. 16, pp. 2535-2537 (2004).
63. O. Frazão, B. V. Marques, P. Jorge, J. M. Baptista, and J. L. Santos, “High birefringence D-type fiber loop mirror used as refractometer,” Sens. Actuators B, Chem., vol. 135, pp. 108–111 (2008).
64. A. Othonos, and K.Kalli, Fiber Bragg Gratings: Fundamentals and Applications in Telecommunications and Sensing, Boston, MA, Artech House,1999.
65. Kersey A., Davis A., Patrick H., Leblanc M., Koo K., Askins C., Putnam A., Friebele E., “Fiber Grating Sensors”; Journal ofLightwave Technology, Vol.15, pp. 1442-1463 (1997).
66. D. N. Nikogosyan, “ Multi-photon high-excitation-energy approach to fibre grating inscription,” Meas. Sci. Technol., Vol.18, pp. R1-R29 (2007).
67. A. M. Vengsarkar, J. R. Pedrazzani, J. B. Judkins, and P. J. Lemaire, “Long-period fiber-grating-based gain equalizers, ” Opt. Lett., Vol. 21, pp. 336-338 (1996).
68. D. D. Davis, T. K. Gaylord, E. N. Glytsis, S. G. Kosinski, S. C. Mettler, and A. M. Vengsarkar, “Long period fibre grating fabrication with focused CO_2 laser pulses,” *Electron. Lett.*, vol. 34, no. 3, pp. 302–303 (1998).
69. I. K. Hwang, S. H. Yun, and B. Y. Kim, "Long-period fiber gratings based on

periodic microbends", Opt. Lett., vol. 24, pp.1263 -1265 (1999).

70. C. Y. Lin, G. W. Chern, and L. A. Wang, “Periodical corrugated structure for forming sampled fiber Bragg grating and long-period fiber grating with tunable coupling strength,” J. Lightwave Technol., Vol. 19, pp. 1212–1220 (2001).
71. Y. Kondo, K. Nouchi, T. Mitsuyu, M. Watanabe, P. G. Kazansky, and K. Hirao, “Fabrication of long-period fiber gratings by focused irradiation of infrared femtosecond laser pulses,” Opt. Lett., Vol. 24, pp. 646–648 (1999).
72. W. Ding and S. R. Andrews, “Modal coupling in surface-corrugated long-period-grating fiber tapers,” Opt. Lett., Vol. 33, pp. 717-719 (2008).
73. G. Kakarantzas, TE Dimmick, TA Birks, RL Roux and PSJ Russell, “Miniature all-fiber devices based on CO_2 laser microstructuring of tapered fibers,” Opt. Lett., Vol. 26, pp. 1137-1139 (2001).
74. H. Xuan, W. Jin, and M. Zhang, “CO_2 laser induced long period gratings in optical MNFs,” Opt. Express, Vol. 17, pp. 21882-21890 (2009).
75. H. Xuan, W. Jin, and S. Liu, “Long period gratings in wavelength-scale MNFs,” Opt. Lett., Vol. 35, pp. 85-87 (2010).
76. K. 0. Hill, F. Bilodeau, B. Male, and D. C. Johnson, “Birefringent Photosensitivity in Monomode Optical Fibre: Application to External Writing of Rocking Filters”, ELEC. TRONICS LETTERS, vol. 27, pp. 1548-1550 (1991).
77. R. Kaul, “Pressure sensitivity of rocking filters fabricated in an elliptical-core optical fiber,” Opt. Lett., Vol. 20, pp. 1000-1001 (1995).
78. G. Kakarantzas, A. Ortigosa-Blanch, T. A. Birks, P. St. J. Russell, L. Farr, F. Couny, and B. J. Mangan, “Structural rocking filters in highly birefringent photonic crystal fiber,” Opt. Lett., Vol. 28, pp. 158–160 (2003).
79. G. Statkiewicz-Barabach, A. Anuszkiewicz, W. Urbanczyk, and J. Wojcik, “Sensing characteristics of rocking filter fabricated in microstructured birefringent fiber using fusion arc splicer,” Opt. Express, Vol. 16, pp. 17249–

17257 (2008).

80. S. E. Kanellopoulos, V. A. Handerek, and A. J. Rogers, "Compact Mach-Zehnder fiber interferometer incorporating photoinduced gratings in elliptical-core fibers," Opt. Lett., Vol. 18, pp. 1013-1015 (1993).
81. S. E. Kanellopoulos, V. A. Handerek, and A. J. Rogers, “Simultaneous strain and temperature sensing employing a photogenerated polarisation coupler and low-order modes in an elliptically cored optical fibre,” Electron. Lett., Vol. 30, pp. 1786–1787 (1994).
82. Zang, L. Y.; Kang, M.S.; Pearce, G. J.; Scharrer, M.; Rammler, S.; Russell, P.S.J., "Dispersive properties of rocking filters in highly birefringent photonic crystal fiber," IEEE/LEOS Winter Topical Meeting Series, vol., no., pp.192-193 (2008).

Chapter 2

Hi-Bi MNFs

2.1 Introduction

Hi-Bi air-cladding silica MNFs with wavelength and sub-wavelength scale transverse dimensions are studied theoretically and experimentally. Hi-Bi MNFs are taper-drawn from the standard SMF-28 single mode fibers that are “pre-processed” by “cutting-away” parts of the silica cladding on opposite sides of the fiber with a femtosecond infrared laser. Such Hi-Bi MNFs have approximately elliptical cross-sections and are approximated by a three-layer model comprising a small central Ge-doped region surrounded by an elliptical silica region and air-cladding. Theoretical modeling shows that phase birefringence of the order 10^{-2} can be achieved with such air-cladding Hi-Bi MNFs. The Hi-Bi MNFs could be useful for micron/nano scale polarization maintaining transmission and phase-sensitive interferometric sensors.

2.2 Basic theory of MNFs

The basic theory for MNFs have already been well developed [1]. The MNF is assumed to have a circular cross-section, and a step index profile as shown in Fig. 2.1,

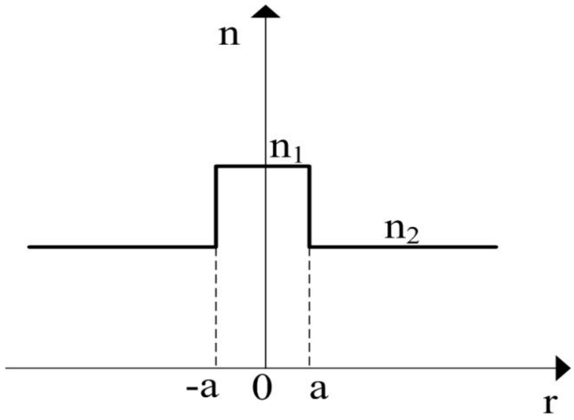

Fig. 2.1 The refractive index profile of MNFs.

$$n(r)=\begin{cases} n_1, & 0<r\le a \\ n_2, & a<r<\infty \end{cases} \tag{2.1}$$

where a is the radius of the MNF, n_1 is the refractive index of the MNF, and n_2 is the refractive index of the air. Here, the cladding is assumed to be the infinite air clad. Under the assumption that the MNF is non-dissipative and source free, the electric (or magnetic) field of the MNF satisfies the Helmholtz equations,

$$\begin{aligned} (\nabla^2+n^2k^2-\beta^2)\vec{e}=0 \\ (\nabla^2+n^2k^2-\beta^2)\vec{h}=0 \end{aligned} \tag{2.2}$$

where k=2π/λ, and β is the propagation constant. The eigenvalue Eq. (2.2) is expressed as follows,

$$\left\{\frac{J_v'(U)}{UJ_v(U)}+\frac{K_v'(W)}{WK_v(W)}\right\}\left\{\frac{J_v'(U)}{UJ_v(U)}+\frac{n_2^2}{n_1^2}\frac{K_v'(W)}{WK_v(W)}\right\}=\left(\frac{v\beta}{kn_1}\right)^2\left(\frac{V}{UW}\right)^4 \tag{2.3}$$

where J_v is the Bessel function of the first kind, K_v is the modified Bessel function of the second kind, and $U=a(k_0^2n_1^2-\beta^2)^{1/2}$, $W=a(\beta^2-k_0^2n_2^2)^{1/2}$.

Through numerical calculation, the propagation constants β at different diameters D of MNF are obtained, as illustrated in Fig. 2.2.

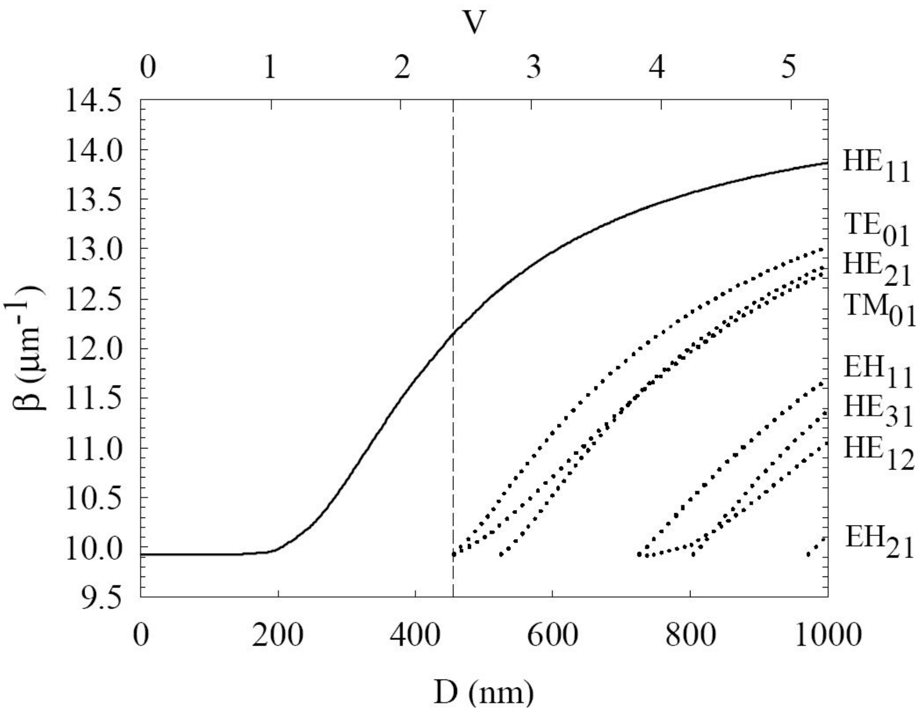

Fig. 2.2 The propagation constants of the MNF of different diameters at wavelength of 633 nm [1]. Solid line: the fundamental mode. Dot lines: the high order modes. Dash line: cut-off frequency.

The single mode condition for MNF is similar with the conventional SMF, and is determined by the normalized frequency,

$$V_c = \frac{2\pi}{\lambda} a \sqrt{n_1^2 - n_2^2} \tag{2.4}$$

where a is the radius of the MNF, λ is the guide light wavelength, and n_1, n_2 are the refractive index of the MNF and air cladding, respectively. If the V_c <2.405, the MNF only supports the fundamental mode. As shown in Fig. 2.2, the MNFs with a diameter of less than 475nm are single mode at wavelength 633nm. In the case of silica MNFs, the single mode condition can be approximately expressed as $D/\lambda<0.73$, if the refractive index of the silica is considered as 1.45.

Since the MNFs have been widely used as the evanescent sensors, the fraction of the modal power inside and outside the MNF is an important issue. From the eigenvalue Eq. (2.2), we can derive the exact value.

If electromagnetic fields are expressed as,

$$\begin{cases} \vec{E}(r,\phi,z) = (E_r\vec{r} + E_\phi\vec{\phi} + E_z\vec{z})\exp(i\beta z) \\ \vec{H}(r,\phi,z) = (H_r\vec{r} + H_\phi\vec{\phi} + H_z\vec{z})\exp(i\beta z) \end{cases} \tag{2.5}$$

When 0<r<a, the expressions of the electric fields inside the core are,

$$\begin{aligned} e_r &= -\frac{a_1J_0(UR)+a_2J_2(UR)}{J_1(U)}\cdot f_1(\phi) \\ e_\phi &= -\frac{a_1J_0(UR)-a_2J_2(UR)}{J_1(U)}\cdot g_1(\phi) \\ e_z &= -\frac{-iU}{\alpha\beta}\frac{J_1(UR)}{J_1(U)}\cdot f_1(\phi) \end{aligned} \tag{2.6}$$

When a<r<∞, the expressions are,

$$\begin{aligned} e_r &= -\frac{U}{W}\frac{a_1K_0(WR)-a_2K_2(WR)}{K_1(W)}\cdot f_1(\phi), \\ e_\phi &= -\frac{U}{W}\frac{a_1K_0(WR)+a_2K_2(WR)}{K_1(W)}\cdot g_1(\phi), \\ e_z &= \frac{-iU}{\alpha\beta}\frac{K_1(WR)}{K_1(W)}\cdot f_1(\phi) \end{aligned} \tag{2.7}$$

The expressions of the magnetic field can be found in the [2]. Then the z-component of Poynting vectors S_z which stands for the z-direction power flow in the fiber, can be derived through the following formula,

$$S_z = \frac{1}{2}\mathrm{Re}\left\{E\times H^*\cdot\vec{z}\right\} \tag{2.8}$$

The S_z in the core (0<r<a),

$$S_{Zco} = \frac{1}{2}\left(\frac{\varepsilon_0}{\mu_0}\right)^{\frac{1}{2}}\frac{kn_1^2}{\beta J_1^2(U)}\left[a_1a_3J_0^2(UR)+a_2a_4J_2^2(UR)+\frac{1-F_1F_2}{2}J_0(UR)J_2(UR)\cos(2\phi)\right] \tag{2.9}$$

in the air (a<r<∞),

$$S_{Zair} = \frac{1}{2}\left(\frac{\varepsilon_0}{\mu_0}\right)^{\frac{1}{2}}\frac{kn_1^2}{\beta K_1^2(W)}\frac{U_2}{W_2}\left[a_1a_5K_0^2(WR)+a_2a_6K_2^2(WR)+\frac{1-2\Delta-F_1F_2}{2}K_0(WR)K_2(WR)\cos(2\phi)\right] \tag{2.10}$$

and $f_1(\phi)=\sin(\phi), g_1(\phi)=\cos(\phi)$,

$$a_1=\frac{F_2-1}{2}, a_2=\frac{F_2+1}{2}, a_3=\frac{F_1-1}{2}, a_4=\frac{F_1+1}{2}, a_5=\frac{F_1-1+2\Delta}{2},$$

$$a_6=\frac{F_1+1-2\Delta}{2}, F_1=\left(\frac{UW}{V}\right)^2\left[b_1+(1-2\Delta)b_2\right], F_2=\left(\frac{UW}{V}\right)^2\frac{1}{b_1+b_2},$$

$$b_1=\frac{1}{2U}\left\{\frac{J_0(U)}{J_1(U)}-\frac{J_2(U)}{J_1(U)}\right\}, b_2=-\frac{1}{2W}\left\{\frac{K_0(W)}{K_1(W)}-\frac{K_2(W)}{K_1(W)}\right\}.$$

From above expressions, the fraction of the power in the MNF can be expressed as,

$$\eta=\frac{\int_{r<a} S_{Zco}dA}{\int_{r<a} S_{Zco}dA+\int_{a\le r<\infty} S_{Zair}dA} \tag{2.11}$$

where, $dA=\pi\cdot rdr$, and a is the MNF radius. In Ref [1], both the power distribution and the η were calculated.

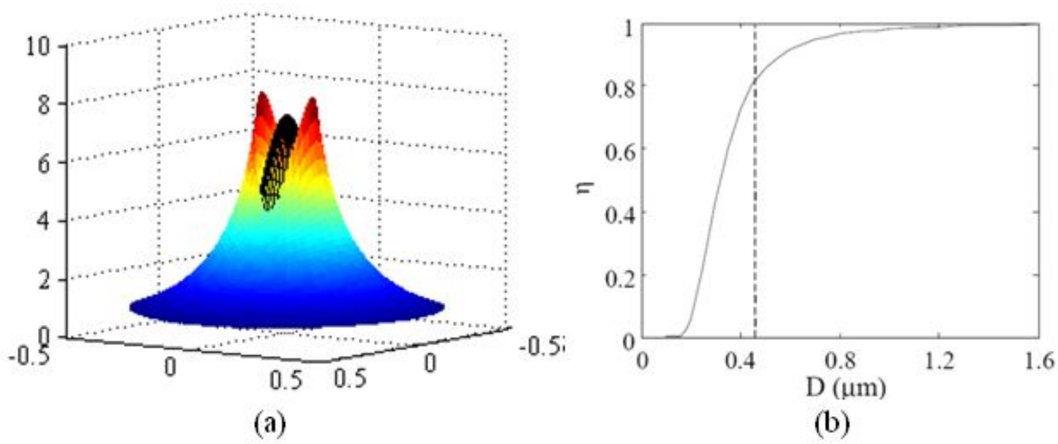

Fig. 2.3 (a) The power distribution in the MNF with a diameter of 200nm at 600nm. (b) The fraction of power in the MNF at different diameters at 600nm [1].

As shown in Fig. 2.3, the fraction of power outside the MNF η increases with the decrease of the MNF diameter. As a result, MNFs with smaller diameters may enhance the sensitivity of MNF based evanescent sensors.

Theoretically, the existence of the fundamental mode is independent of the MNF thickness. However, studies show that the loss of the MNF will limit the radius of MNFs. If the radius decreases to a considerably smaller value, the loss mainly caused by the input and output loss at the adiabatically tapered region increases greatly. For a MNF taper with a waist diameter greatly smaller than the wavelength of the guide light, the radiation loss is estimated to be [3],

$$P \sim \exp\left(-\frac{0.51L}{a_0^{\frac{1}{2}}(a_\infty - a_0)^{\frac{1}{2}}} \exp(-\frac{0.143\lambda^2}{a_0^2}) \right) \tag{2.12}$$

where, P is the radiation loss, L is the characteristic length of the taper MNF, a_∞ and a_0 are the taper radii at the MNF ends and at the MNF center, respectively. From the formula (2.12), the loss is approximately inversely double-exponentially dependent on the radius of the MNF waist radius. As a result, an appropriate diameter is important for designing an evanescent sensor with both high sensitivity and low loss.

2.3 Hi-Bi MNFs

The most common types of polarization maintaining (PM) fibers are shown in Fig. 1.6, named PANDA fiber [4] and bow-tie fiber [5], respectively, according to their appearance, the birefringence of these fibers is induced by the stress rod. Alternatively, Hi-Bi operation can also be achieved by asymmetric waveguide geometry, and the elliptical core fibers are a typical representative of this type [6, 7]. Owing to the flexibility of structure and the feasibility of fabrication, PCF can generate a Hi-Bi with an asymmetric design [8, 9] and an elliptical core [10], as shown in Fig. 2.4. In this paper, the high birefringence is achieved by the asymmetric waveguide geometry of an elliptical shape cross-section [11].

2.3.1 Elliptical optical MNF

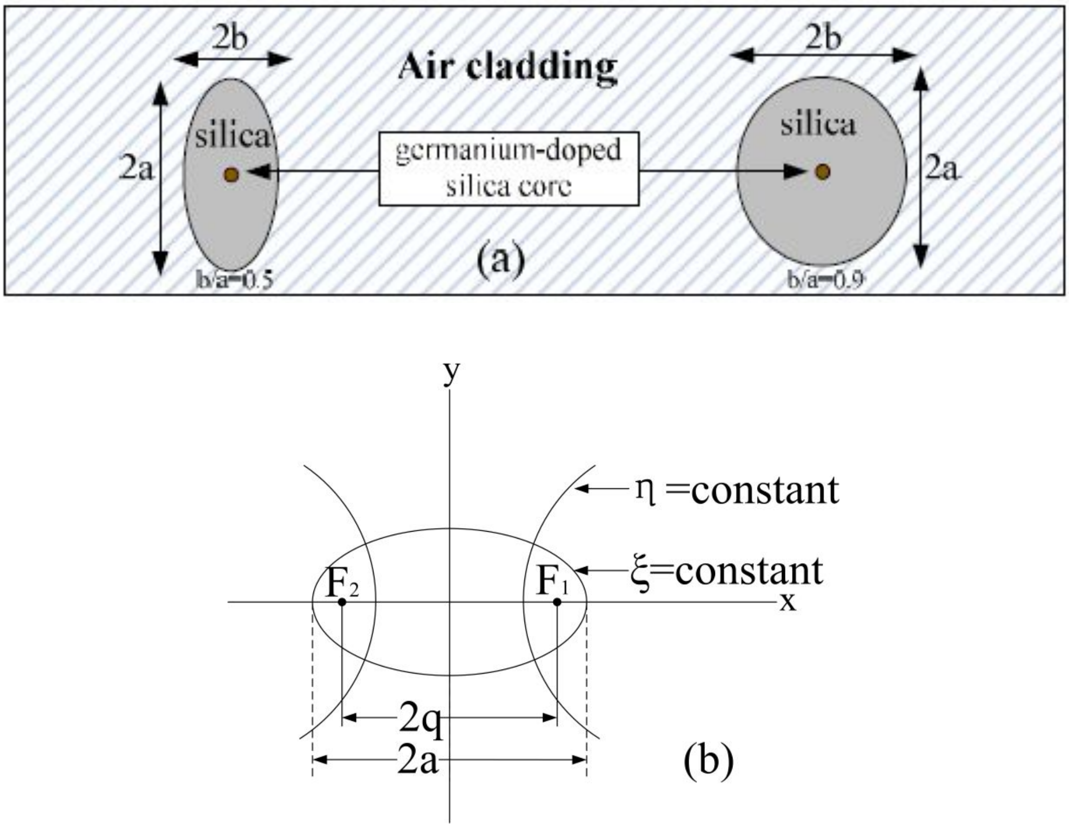

Fig.2.4 (a) The three layer model of air-cladding elliptical MNF [11] (b) Elliptical coordinate system

Fig. 2.4 (a) [11] shows a theoretical model used to study the properties of such air-cladding Hi-Bi MNFs. The model comprises three layers or regions: an infinite air-cladding, an elliptical core made predominantly of silica with a tiny circular Ge-doped center region. The key waveguide parameters of the fiber are semi-major axis “a” and semi-minor axis “b”. The diameter of the Ge-doped region is very small and can be estimated by $D \approx (8.3/125)*2a$.

The mode property of a MNF can be studied readily by solving the Maxwell equations for a uniform, elliptical symmetric multilayer dielectric waveguide. Either a two-layer (i.e, a elliptical silica rod with an infinite air clad) or a three-layer (a

Ge-doped central region, a silica elliptical region and an infinite air clad) step-index model may be used. For the MNFs interested in this paper, the Ge-doped region has a diameter of ~0.4 μm or less and a refractive index ~0.36% higher than that of fused silica. In the following, the three-layer elliptical model is adopted to investigate the modal characteristics of the Hi-Bi MNFs with the finite element method.

Fig. 2.4 (b) shows the elliptical coordinate, the radial ξ coordinate describes a set of confocal ellipses and the η animuth coordinate a set of hyperbolae orthogonal to the ellipses. The axial coordinate, in the direction of propagation, is z. The elliptical coordinates ξ, η, and z relate to the Cartesian coordinates x, y, and z as

$$x = q\cosh\xi\cos\eta \tag{2.13a}$$

$$y = q\cosh\xi\cos\eta \tag{2.13b}$$

$$z = z \tag{2.13c}$$

Defining the core boundary by $\xi = \xi_0$, the semi-major and semi-minor axes of the core ellipse are $a = q\cosh\xi_0$; $b = q\sinh\xi_0$.

The eccentricity e is

$$e = \left(1 - \left(\frac{b}{a}\right)^2\right)^{\frac{1}{2}} = \frac{1}{\cosh\xi_0} \tag{2.14}$$

The wave equations in elliptical coordinates are

$$\frac{\partial^2 E_z}{\partial\xi^2} + \frac{\partial^2 E_z}{\partial\eta^2} + \left[q^2\left(\varepsilon k_0^2 - \beta^2\right)\left(\sinh^2\xi + \sin^2\eta\right)\right]E_z = 0 \tag{2.15a}$$

$$\frac{\partial^2 H_z}{\partial\xi^2} + \frac{\partial^2 H_z}{\partial\eta^2} + \left[q^2\left(\varepsilon k_0^2 - \beta^2\right)\left(\sinh^2\xi + \sin^2\eta\right)\right]H_z = 0 \tag{2.15b}$$

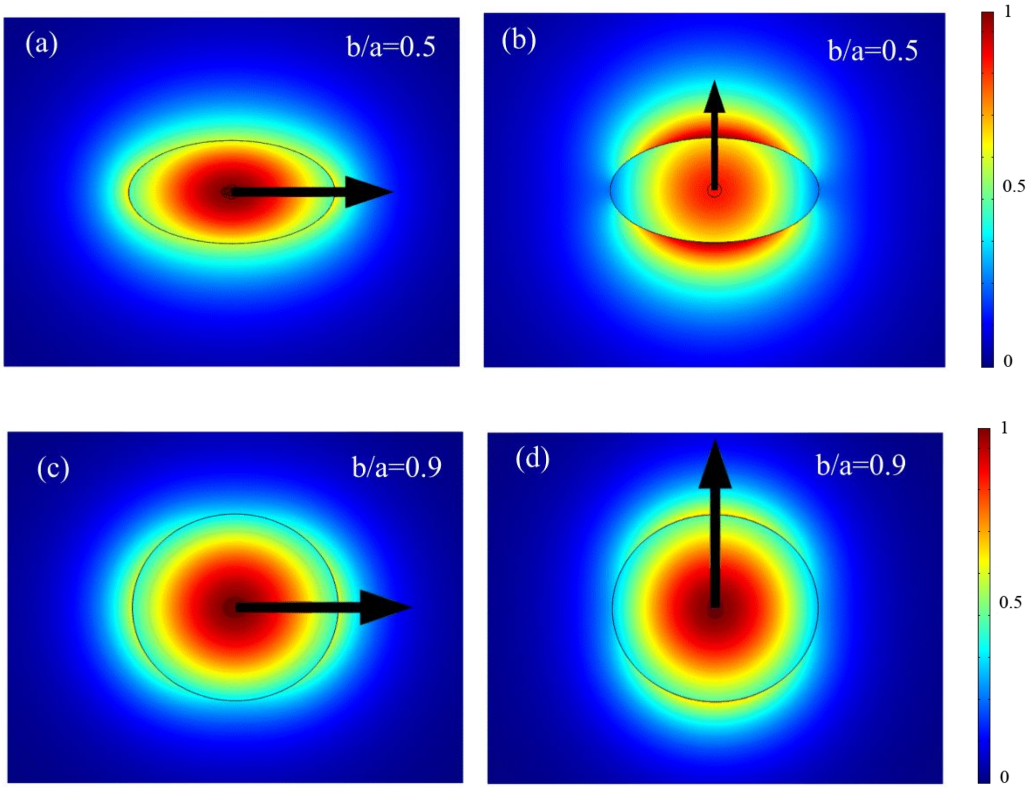

Fig. 2.5 Calculated intensity profiles and electric field directions (black arrows) of the two polarization eigenmodes of the MNFs at 1550 nm.

Although an elliptical dielectric waveguide may processes an analytic solution, the eigenvalue equations for various modes are no longer defined special function equations as in the circular dielectric boundary, but a sets of infinite homogenous algebraic equations [12, 13]. In addition, no single order analytic special function representing a single modal field can be found for those boundary conditions, even for a weakly guiding elliptical fibers [12, 14]. In this paper, the waveguide property of the air-cladding elliptical MNFs is numerically investigated by use of a full vector finite-element method (FEM). The Hi-Bi MNFs are numerically modeled with the following parameters: b/a=0.5 and $2a$~1.4μm, b/a=0.9 and $2a$~1.4μm. The fast/slow fiber mode has an electric field oriented along the minor/major axis of the core as shown in Fig. 2.5. The fraction of the total power carried in the core is often called the modal confinement and is represented by equation (2.16), and can be described as

$$\frac{P_{core}}{P_{total}} = \frac{\dfrac{\overline{\beta}}{\overline{\upsilon_g}} - n_2^2}{n_1^2 - n_2^2} \tag{2.16}$$

where $\overline{\beta}$ is the normalized constant, equals to effective refractive index, and $\overline{\upsilon_g}$ is normalized group velocity, equal to group refractive index. The ${}_o$HE$_{11}$ mode with the better "binding geometry" has the greater fraction of the power in the core.

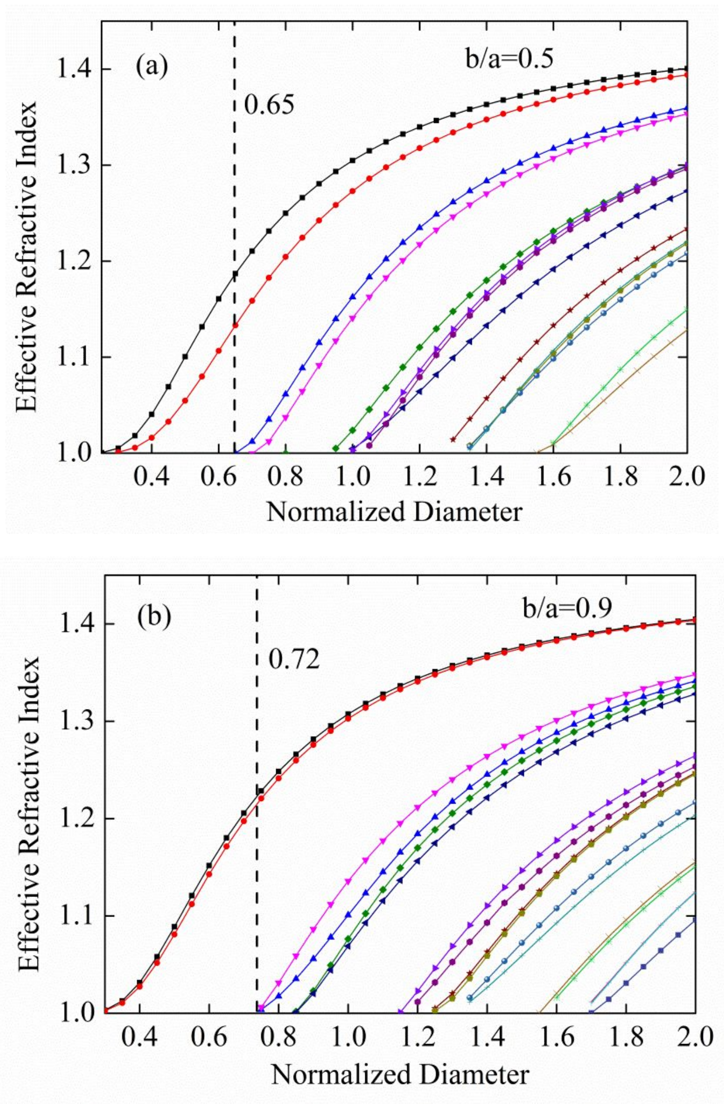

Fig.2.6 Effective indexes of lower-order modes as functions of normalized fiber diameter ($\sqrt{2a*2b}/\lambda$) for *b/a*=0.5 (a) and *b/a*=0.9 (b) [11].

Fig. 2.6 (a) and (b) [11] show respectively the effective refractive indices of the lower order modes as functions of normalized fiber diameter $\sqrt{2a*2b}/\lambda$ for MNFs with *b/a*=0.5 and *b/a*=0.9, respectively. When the normalized diameter is reduced to a certain value as denoted as the vertical dotted line in Figs. 2.6 (a) and 2.6 (b), the MNF can just support single mode which has two non-degenerated HE11 (oHE$_{11}$ and eHE$_{11}$) modes. The cut-off condition in elliptical MNFs depends on the ellipticity of the fiber; for example, ~ 0.65 for *b/a*=0.5 (Fig. 2.6 (a)) and ~0.72 for *b/a*=0.9 (Fig. 2.5 (b)).

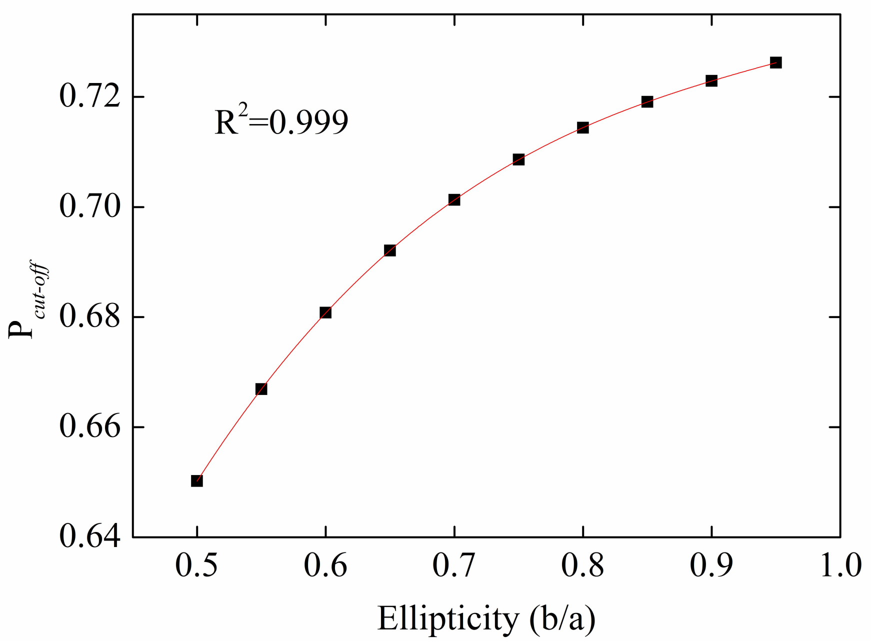

Fig. 2.7 Cut off condition as a function of ellipticity (b/a)

Through a series of numerical calculations, for 0.5<*b/a*<1, the higher order modes cut-off condition of the air-cladding elliptical MNFs can be fitted to the following polynomial, as shown in Fig. 2.7

$$\frac{\sqrt{2a*2b}}{\lambda}=P_{cut-off}\left(\frac{b}{a}\right)=0.4519*\left(\frac{b}{a}\right)^3-1.3181*\left(\frac{b}{a}\right)^2+1.3448*\left(\frac{b}{a}\right)+0.2508 \tag{2.17}$$

2.3.2 Birefringence

One of the most important characteristics of elliptically cored fiber is its ability to preserve the polarization of a guided wave by the decoupling of the propagation constants of the fast mode and slow mode of HE_{11} mode, known as the birefringence, and defined as the difference between the normalized propagation constant, $\Delta\beta = \overline{\beta_s} - \overline{\beta_f}$.

Ramaswamy et al. [15] adapted Marcatili's calculations for rectangular waveguide [16] to give the birefringence:

$$\frac{a\Delta\beta}{e^2\left(1-\left(\frac{n_2}{n_1}\right)^2\right)^{\frac{3}{2}}} \approx \frac{3\pi V^2}{(V+2)^4} \tag{2.18}$$

where

$$V = \frac{2\pi a}{\lambda_0}\left(n_1^2 - n_2^2\right)^{\frac{1}{2}} \tag{2.19}$$

Schlosser [17], using a more sophisticated analysis, has

$$\frac{a\Delta\beta}{e^2\left(1-\left(\frac{n_2}{n_1}\right)^2\right)^{\frac{3}{2}}} \approx \frac{u^4 w^3}{8V^5 J_1^2(u)}\left[\frac{K_0(w)}{K_1(w)} + \frac{1}{w}\right] \tag{2.20}$$

where

$$u = b(k_0^2 n_1^2 - \beta^2)^{1/2}, \;\; w = b(\beta^2 - k_0^2 n_2^2)^{1/2} \tag{2.21}$$

Marcuse [18] has the approximation

$$\frac{a\Delta\beta}{e^2\left(1-\left(\frac{n_2}{n_1}\right)^2\right)^{\frac{3}{2}}} \approx \frac{u^2 w^2}{8V^3} \tag{2.22}$$

Snyder and Young [19] use another approximation to give

$$\frac{a\Delta\beta}{e^2\left(1-\left(\frac{n_2}{n_1}\right)^2\right)^{\frac{3}{2}}} \approx \frac{u^2w^2}{8V^3}\left[1+\frac{uK_0^2(w)J_2(u)}{K_1^2(w)J_1(u)}\right] \tag{2.23}$$

All these approximations use the normalized birefringence term

$$X = \frac{a\Delta\beta}{e^2\left(1-\left(\frac{n_2}{n_1}\right)^2\right)^{\frac{3}{2}}} \tag{2.24}$$

which can be arranged in the form

$$\frac{\Delta\beta}{(\Delta n)^2} = \frac{4\frac{b}{a}\left[1-\left(\frac{b}{a}\right)^2\right]X}{n_1V_b} \tag{2.25}$$

Where

$$V_b = \sqrt{u^2+w^2} \tag{2.26}$$

The birefringence $\Delta\beta$ is then seen to be proportional to $(\Delta n)^2$. For a traditional elliptical core fiber comprising a Ge-doped core and silica cladding, the core-cladding index difference Δn is typically less than 0.04. If the silica cladding were replaced by air, which has an index difference of ~0.45 from the doped silica core, the birefringence of the fiber with the same core-size and shape would have a much larger birefringence.

In ref [11], the birefringent properties of Hi-Bi MNFs are given by the difference of refractive index of the two polarized mode, $B = n_s - n_f$. From Fig. 2.6 (a) and 2.6 (b), it is found that the birefringence raises with increasing ellipticity. More detailed information about birefringence in these elliptical MNFs is shown in Fig. 2.8. The birefringence as a function of normalized fiber diameter $\sqrt{2a*2b}/\lambda$ with different ellipticity (*b/a* from 0.9 to 0.5) is shown in Fig. 2.8 (a) (the X and the left-Y axes), while the maximum birefringence $B_{\max}$ as a function of *b/a* is shown in the Fig. 2.8 (b). The birefringence of these air-clad elliptical MNFs is very high even with a small ellipticity and is increasing dramatically with an increase of ellipticity. The maximum birefringence *max B* is ~ 0.054 for a MNF with *b/a*=0.5 and ~0.01 for a MNF with *b/a*=0.9. From the results in Fig. 2.8 (a), the condition for maximum birefringence may be approximated by:

$$\frac{\sqrt{2a*2b}}{\lambda} \sim 0.6 \tag{2.27}$$

Eq. (2.25) shows that to achieve the highest birefringence the dimension of MNF (semi-major axis “*a*” and semi-major axis “*b*”) should be down to the sub-wavelength scale. Furthermore, from Fig. 2.7 (b), the relationship between *max B* and *b/a* may be fitted to the following polynomial:

$$B_{\max} = 0.043946 * \left(\frac{b}{a}\right)^2 - 0.17444 * \left(\frac{b}{a}\right) + 0.13053 \tag{2.28}$$

The higher order modes cut-off or single mode condition is also indicated in Fig. 2.7(a) by the“☆” line corresponding to X and right-Y axes. The left side of this line is the single mode operation region in which only the two orthogonal polarizations of the fundamental mode are guided by the fiber. It is obvious that the maximum birefringence for a Hi-Bi MNF with a *b/a* of from 0.5 to 1 always occur in the single mode region. This property is important for Hi-Bi MNF design, since the maximum possible birefringence and single mode operation can be achieved at the same time.

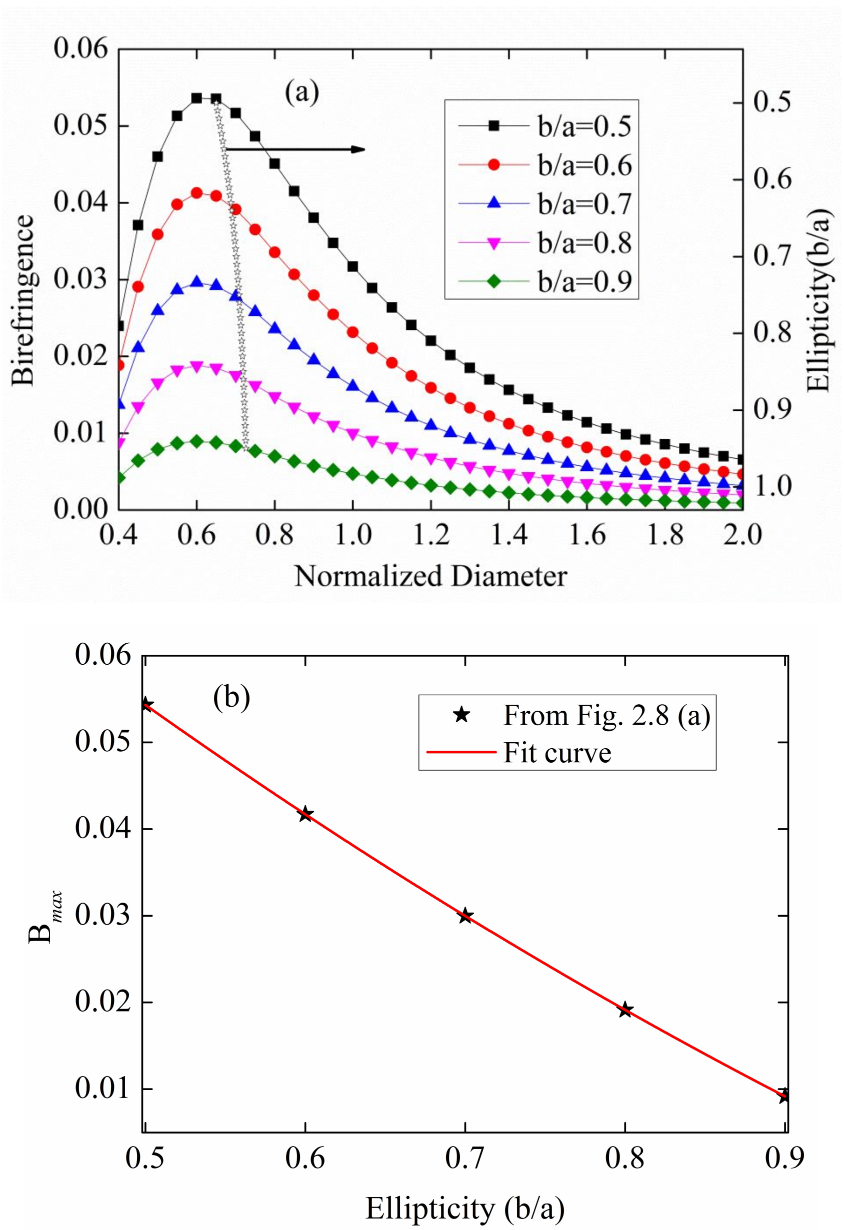

Fig.2.8 (a) Birefringence as a function of normalized fiber diameter $\sqrt{2a*2b}/\lambda$ for elliptical MNFs with various b/a from 0.9 to 0.5 (left y-axis). The "+" line (right y-axis) is the higher modes cut-off line; the left side of this line is the single mode region. (b) Maximum birefringence in elliptical MNFs as a function of *b/a*. [11] The data represented by red points are obtained from Fig. 2.7 (a), and the data of the blue line are calculated according to the Eq. (2.26)

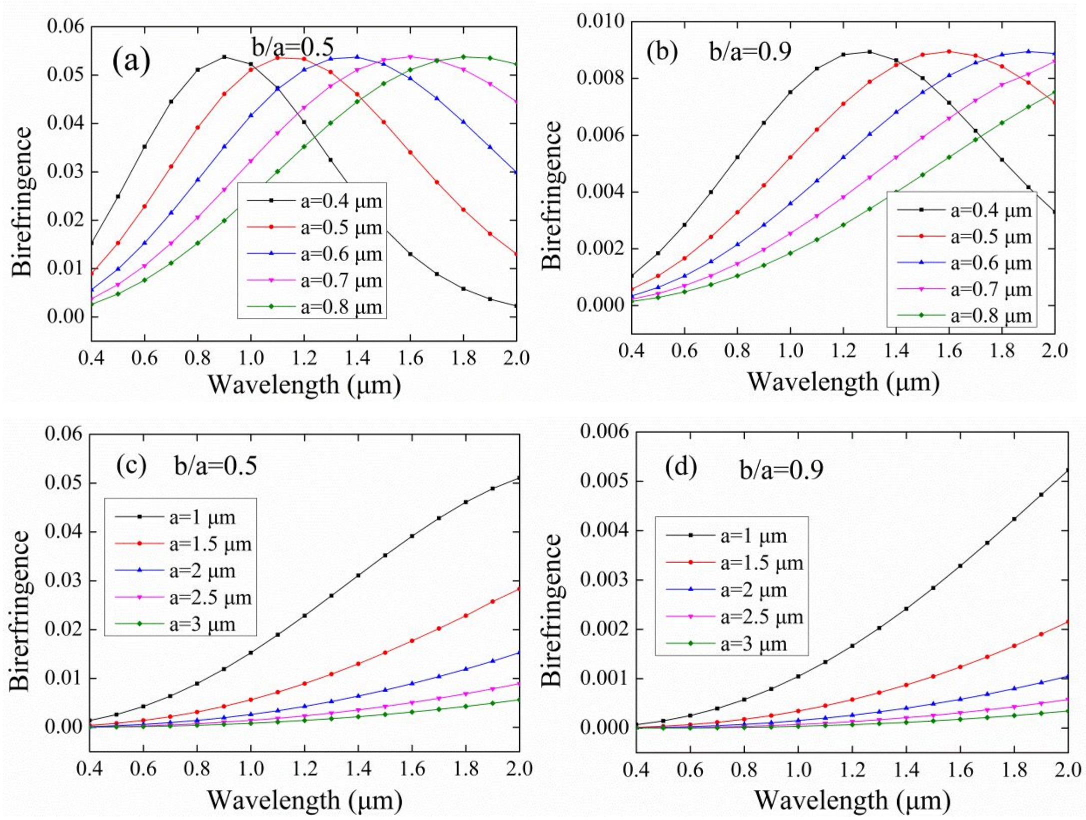

Fig. 2.9 Birefringence as a function of optical wavelength for various fiber dimensions and ellipticities. (a) b/a=0.5, a from 0.4 to 0.8 μm; (b) b/a=0.9, a from 0.4 to 0.8 μm; (c) b/a=0.5, a from 1 to 3 μm; and (d) b/a=0.9, a from 1 to 3 μm.

Fig. 2.9 shows the variations of birefringence as functions of optical wavelength for MNFs with various diameters from 0.2μm to 5μm. Fig. 2.9 (a) and 2.9 (c) are for b/a=0.5, while Fig. 2.9 (b) and 2.9 (d) are for b/a=0.9. As illustrated in Fig. 2.9 (a) and 2.9 (b), the peak of the birefringence-λ curve shifts to longer wavelength and becomes broader when the semi-major axis a is increased from 0.4 to 0.8μm, while the maximum birefringence B_{max} remains at a constant level for a fixed b/a ratio. This means that the maximum birefringence B_{max} is independent of the value of a, but strongly depend on the ellipticity or b/a ratio as shown in Fig. 2.8 and 2.9. The results shown in Fig. 2.9 (a) and 2.9 (b) also confirm that the wavelength corresponding to maximum birefringence B_{max} can indeed be estimated by Eq. (2.25).

For example, for a MNF with b/a=0.5 and a=0.6 μm, the peak birefringence wavelength may be estimated to be $\lambda = \sqrt{2a * 2b * 0.5} / 0.6 = 1.41$ μm, and this prediction clearly agrees with the peak wavelength obtained from the Fig. 2.9 (a). When the fiber dimension is beyond a~1μm, the birefringence in wavelength range of below 2 μm decreases dramatically as shown in Fig. 2.9 (c) and 2.9 (d). This is because the peak birefringence wavelength has shifted to a much longer wavelength as predicted by Eq. (2.5). In addition, the MNF will become multi-modes for a larger fiber size beyond the critical value as predicted by Eq. (2.16).

2.4 Fabrication

In our lab, air-clad Hi-Bi MNFs with wavelength and sub-wavelength scales diameters are fabricated from a standard telecommunication fiber (SMF-28) through a two-step process: firstly, the SMF-28 fiber is "pre-processed" by "cutting away" parts of the silica on opposite sides of the cladding with a femtosecond infrared (IR) laser; and then the "processed" SMFs are taper-drawn to wavelength and sub-wavelength scale with a commercial coupler fabrication rig. We show theoretically that phase and group birefringence of the order of 10^{-2} can be achieved with such air-clad Hi-Bi MNFs. At the same time, another technique to fabricate Hi-Bi MNF was proposed by using a rectangular silica fiber [20, 21], which is drawn from a rectangular preform, also tapered down to wavelength and sub-wavelength scales to generate birefringence with rectangular cross-section after being spliced with SMFs. These two structure induced the highly birefringence by the asymmetric geometry, and the technique in our lab shows more flexible to design the Hi-Bi MNFs.

2.4.1 Femtosecond laser micromachining technique

Laser machining is a process that uses a focused optical light beam to selectively remove materials from a substrate to create a desired feature on or internal to the substrate. Compared with conventional mechanical machining techniques, laser assisted machining exhibits advantages of non-contact, good machining quality, high flexibility and easiness of automation. However, conventional laser machining, cw or pulsed, can't create micron-sized structures because linear optical absorption of the materials often leads to heat deposition, and micro-cracks and small collateral damage to the surrounding is unavoidable.

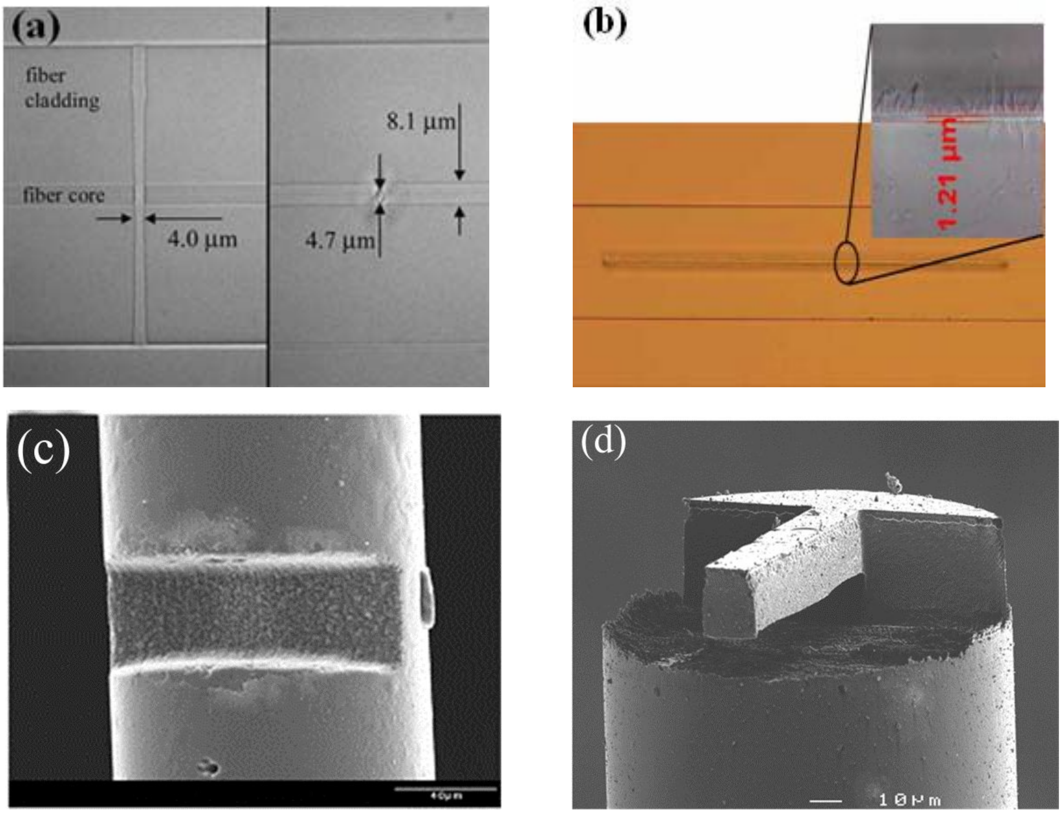

Fig 2.10 Fs laser inscribed (a) micro-channel (b) micro-slot [22, 23]. (c) Fs laser inscribed FPI in SMF[24-27]. (d) Fs laser 3D micro-machined cantilever on fiber tip [28].

The generation of femtosecond (fs) laser is the greatest breakthrough in the field of laser technique, and femtosecond laser micromachining is a rapidly advancing area of ultrashort laser applications. It utilizes the ultrashort laser pulse properties to achieve an unprecedented degree of control in sculpting the desired microstructures internal to the materials without collateral damage to the surroundings, which has been widely used in fiber post-processing, including hole drilling [22], line cleaving [23], engraving [24-27] and 3D micro-machining processing [28], attributed to its advantages of fast temporal resolution, high pulse repetition rate and high peak intensity. With the maturation of the commercialized fs laser system, the fs laser micro-machining has also been employed intensively in material operation. Compared with CW or long pulse duration lasers, the fs laser has initiated many new machining fields, such as high precision, small destruction, spatial 3 dimensional (3D) internal Processing. In general, the fs laser machining has the following novel properties [29]:

(1) Small machining dimension. The transverse dimension of laser focus spot and thus the machining result is always larger than the laser wavelength due to the diffraction limit which the fs laser also obeys. However, due to the ultrahigh pulse peak power of fs laser, the normally involved nonlinear absorption of photon energy will result in the material damage being strongly dependent on the laser energy and its spatial intensity distribution. The fs laser normally has a spatial Gaussian distribution, which has its strongest intensity at the focus spot center and quickly decreases along the focus spot radius. Therefore, through precisely adjusting the pulse energy when only the laser power intensity at the focus spot center could achieve the material damage threshold, one can obtain a sub-micro machining dimension, which is much smaller than the entire focus spot size. For example, periodical structures with nm scale can be fabricated on SU-8 material through a two-photon absorption process [30].

(2) Less thermal effect during the laser operation process. The ultrahigh pulse

peak power and ultrashort pulse duration enable fs laser to interact with materials with little energy diffusion. This can help to eliminate the usually involved defects in laser machining such as material melting, thermal diffusion and shockwave. Moreover, the emitted ions have the same charge polarity as the electron plasma generated, which prevents re-contamination of the machining surface. Therefore, the fs laser machined surface has a much smoother morphology compared with that machined by long pulse duration lasers [31].

(3) Capability of internal 3D machining of transparent materials. Since transparent materials do not linearly absorb the fs laser energy, the laser energy could transmit to the internal focus point with little loss. Therefore, by carefully adjusting the laser energy, internal machining of transparent materials could be achieved while leaving the surface unaffected [32].

(4) Diversity of machining materials and low energy assumption. Due to the different absorption process of fs laser energy, the materials under operation have deterministic threshold energy. The ablation of material strongly depends on the laser pulse energy. Laser energy absorption and ablation threshold energy only depend on the atom properties of the material, which has nothing to do with the free carrier concentration in the material. Therefore, an fs laser with ultrashort pulse duration and enough pulse energy can machine any kinds of materials, such as silica, ceramics, semiconductors, polymers, biological tissues [30-33].

2.4.2 Fabrication of Hi-Bi MNF

Air-cladding Hi-Bi MNFs are fabricated from a commercial SMF-28 (outer diameter D~125μm, core diameter d~8.2μm, $\Delta n \sim 0.36\%$) by following a two-step process [11]: firstly, the SMF-28 fiber is “processed” by “cutting away” parts of the silica on opposite sides of SMF cladding with a femtosecond IR laser, resulting in an approximately square-like cross-section as depicted in Figs. 2.11 (b) and 2.11 (c);

then, the “processed” SMF is taper-drawn to wavelength or sub-wavelength scale by using a commercial optical fiber coupler fabrication rig. The cross-sectional shape of the “processed” region was found to retain its square-like shape during the initial taper-drawn process and eventually turned to an approximately elliptical shape when the fiber diameter was drawn down to sub-wavelength dimensions.

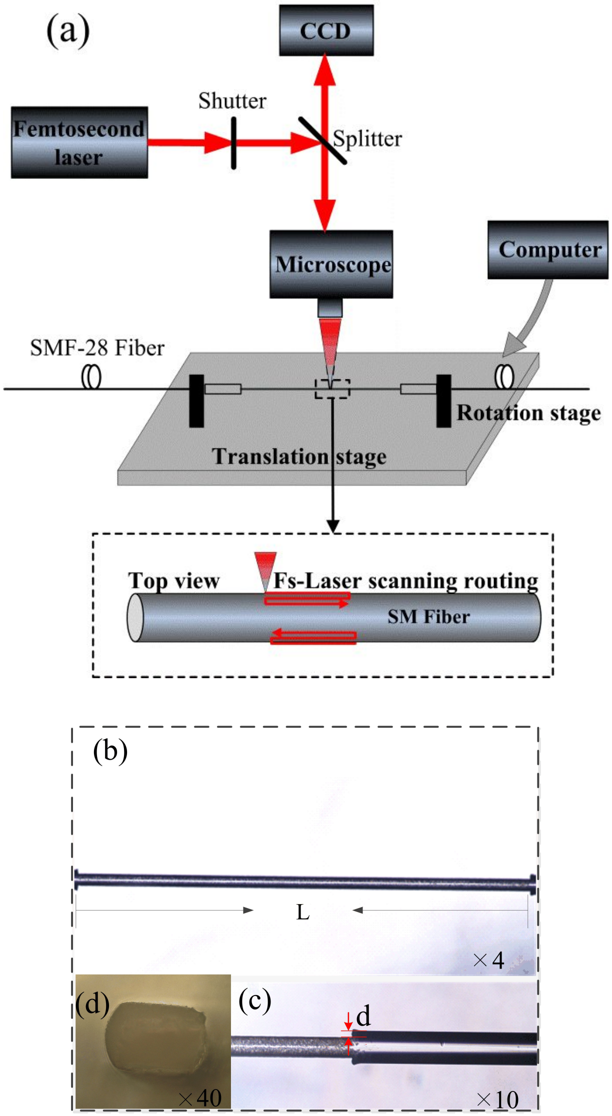

Fig. 2.11 (a) Schematic of the femtosecond IR laser system for SMF “pre-processing”. The femtosecond laser scanning routing is shown in the magnified inset. (b), (c) and (d) Microscope image of the idealized “pre-processed” SMF section from which a Hi-Bi MNF may be taper-drawn.

Fig. 2.11 (a) shows the schematic of the femtosecond IR laser setup for "pre-processing" of SMFs. Laser pulses with wavelength of 800nm, duration of 120 fs, and a repetition rate of 1 kHz are produced by a Ti: sapphire laser. The laser beam is focused onto the SMF by a microscope objective (×10), and the focal spot size is ~3μm. With the assistance of an optical microscope, the laser focal position is monitored and displayed on a LCD monitor, through which the location of the focal point can be accurately adjusted via a computer controlled translation stage.

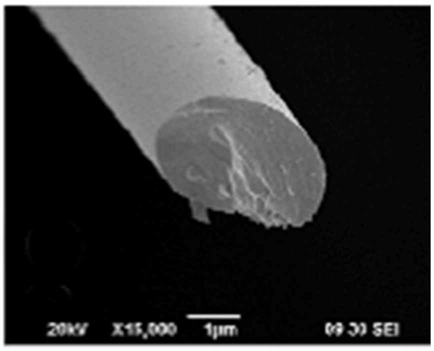

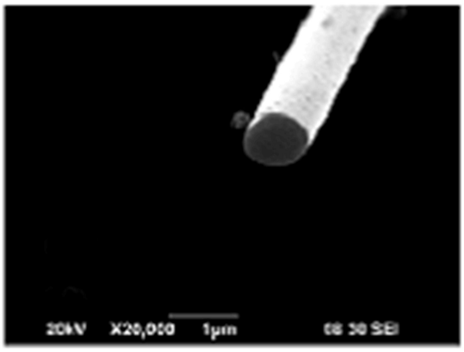

Fig. 2.12 (a) and (b): SEM images of elliptical Hi-Bi MNFs whose diameters are on the order of ~1μm, which are taper-drawn from the "processed" SMF [11].

The SMF is mounted on a computer-controlled three-axis translation stage with a tuning resolution of 100nm. The laser pulses with an irradiation intensity of ~20 J/cm^2 are focused onto the one side of the SMF cladding and moved along a pre-programmed track with a speed of 10 μm/s. The detailed routing of femtosecond laser scanning is shown in the magnified inset in Fig. 2.11 (a). Firstly, the focused laser beam scans longitudinally from left to right along the outer-most surface of the fiber for a length of L, then the laser beam moves transversely toward the center of the fiber by a step of ~3μm to perform another longitudinal scanning from right to left. This process is repeated for N times to produce, on one side of the fiber, a square-shaped groove with depth of d (~ N*3μm) and a length of L as shown in the Fig. 2.11 (b). By following the same routine, a similar groove is created on the opposite side of the fiber. The section of the SMF after "processing" should have a shape similar to that shown in the Figs. 2.11 (b) and (c), and the square-like cross-section is shown in Figs. 2.11 (d).The depth of "processed" part "d" can be as small as 15μm to produce MNFs with a sufficiently large birefringence [11].

The "processed" SMF samples are taper-drawn to wavelength or sub-wavelength scale by use of a commercial optical fiber coupler fabrication rig. The SMF is heated and soften by a hydrogen flame which covers about ~8mm length of fiber, much bigger than the length of pre-processed fiber section. The flame is scanning along the fiber back and forth with a scan length of l and a velocity of V_f, while the two translation stages move in the opposite direction with the same velocity V_s. The fiber could be pulled and tapered adiabatically into a MNF with diameter about hundreds nanometers or several micrometers. With proper fabrication parameters, non-circular MNFs with diameter from below one to several micrometers can be fabricated. Figs 2.12 (a) and (b) show the scanning electron microscope (SEM) images of elliptical Hi-Bi MNFs with wavelength and sub-wavelength dimensions. In our experiment, the MNF was fabricated by the flame-assisted taper drawing device. An MNF with a diameter down to ~1 μm with relative low loss has already been produced by this method and with a taper length of up to 5 cm [11].

2.5 Summary

Highly birefringent (Hi-Bi) air-clad silica MNFs with wavelength and sub-wavelength scale transverse dimensions are studied theoretically and experimentally. Hi-Bi MNFs are taper-drawn from the standard SMF-28 that are "pre-processed" by "cutting-away" parts of the silica cladding on opposite sides of the fiber with a femtosecond infrared laser. Such Hi-Bi MNFs have approximately elliptical cross-sections and are approximated by a three-layer model comprising a small central Ge-doped region surrounded by an elliptical silica region and air-cladding. Theoretical modeling shows that phase birefringence of the order 10^{-2}

can be achieved with such air-cladding Hi-Bi MNFs. Empirical formulas that relate the higher order mode cutoff and the maximum birefringence with ellipticity, and that determine the peak birefringence wavelength for a given fiber dimension are obtained. These results will be important for the design of Hi-Bi MNFs with desired properties.

References of Chapter 2

1. Tong, L., J. Lou, and E. Mazur, “Single-mode guiding properties of subwavelength-diameter silica and silicon wire waveguides,” Opt. Express., Vol. 12, pp. 1025-1035 (2004).
2. A. W. Snyder, and J. D.L, Optical waveguide theory (Chapman and Hall, New York, NY 1983).
3. S. umetsky, M., “How thin can a MNF be and still guide light?,” Opt. Lett., Vol. 31, pp. 870-872 (2006).
4. T. Hosaka, K. Okamoto, T. Miya, Y. Sasaki, and T. Edahiro, "Low-Loss Single Polarization Fibers with Asymmetrical Strain Birefringence," Electron. Lett. **17**, 530-531 (1981).
5. M. P. Varnham, D. N. Payne, R. D. Birch, and E. J. Tarbox, "Single-Polarization Operation of Highly Birefringent Bow-Tie Optical Fibers," Electron. Lett. **19**, 246-247 (1983).
6. S. C. Rashleigh, and M. J. Marrone, "Polarization Holding in Elliptical-Core Birefringent Fibers," Ieee J. Quantum Electron. **18**, 1515-1523 (1982).
7. R. B. Dyott, J. R. Cozens, and D. G. Morris, "Preservation of polarisation in optical-fibre waveguides with elliptical cores," Electron. Lett. **15**, 380-382 (1979).
8. A. Ortigosa-Blanche, J.C. Knight, W.J. Wadsworth, J.Arriaga, B.J.Mangan,T.A. Birks, and P.St.J. Russell, “Highly birefringent photonic crystal fibers,” Opt.

Lett. 25, 1325-1327 (2000).

9. D. Chen and L. Shen, "Ultrahigh birefringent photonic crystal fiber with ultralow confinement loss," IEEE Photon. Technol. Lett., Vol. 19, pp. 185-187 (2007).
10. T. P. Hansen, J. Broeng, S. E. B. Libori, E. Knudsen, A. Bjarklev, J. R. Jensen, and H. Simonsen, “Highly birefringent index-guiding photonic crystal fibers,” IEEE Photon. Technol. Lett., Vol. 13, pp. 588-590 (2001).
11. Haifeng Xuan, Jian Ju, and Wei Jin, "Highly birefringent optical MNFs," Opt. Express, Vol. 18, pp. 3828-3839 (2010).
12. R. B. Dyott, Elliptical fiber waveguides, Artech House, boston.london, (1995).
13. C. Yeh, "Elliptical dielectric waveguides," AIP, pp. 3235-3243 (1962).
14. J. K. Shaw, W. M. Henry, and W. R. Winfrey, "Weakly guiding analysis of elliptical core step index waveguides based on the characteristic numbers of Mathieu's equation," J. Lightwave Technol., Vol. 13, pp. 2359-2371 (1995).
15. V. Ramaswamy, W. G. French, and R. D. Standley, "Polarization characteristics of noncircular core single-mode fibers," Appl. Opt. 17, 3014-3017 (1978).
16. Marcatili, E.A.J. “Dielectric optical waveguides and directional coupler for integrated optics,” Bell System Technical Journal, Vol. 48, pp. 2071-2102 (1969).
17. Schlosser, W.O. “Delay distortion in weakly guiding optical fibers due to elliptical deformation at the boundary,” Bell System Technical Journal, Vol. 51, pp. 487-492 (1972).
18. Marcuse, D. Theory of Dielectric Optical Waveguides, Academic Press: New York, pp. 158 (1974).
19. Allan W. Snyder and William R. Young, "Modes of optical waveguides," J. Opt. Soc. Am., Vol. 68, pp. 297-309 (1978).
20. Y. Jung, G. Brambilla, K. Oh, and D. J. Richardson, “Highly birefringent silica

MNF,"Opt. Lett., Vol. 35, pp. 378–380 (2010).

21. J. Li, L. P. Sun, S. Gao, Z. Quan, Y. L. Chang, Y. Ran, L. Jin and B. O. Guan, "Ultrasensitive refractive index sensors based on rectangular silica MNFs," Opt. Lett., Vol. 36, pp. 3593-3595 (2011)
22. Y. Lai, K. Zhou, I. Bennion, "Microchannels in conventional single-mode fibers," Opt. Lett., Vol. 31, pp. 2559-2561 (2006).
23. K. Zhou, Y. Lai, X. Chen, et al, "A refractometer based on a micro-slot in a fiber Bragg grating formed by chemically assisted femtosecond laser processing," Opt. Express, Vol. 15, pp. 15848-15853 (2007).
24. Y. Rao, M. Deng, D. Duan, et al, "Micro Fabry-Perot interferometers in silica fibers machinded by femtosecond laser," Opt. Express, Vol. 15, pp. 14123-14128 (2007).
25. Z. L. Ran, Y. J. Rao, W. J. Liu, et al, "Laser-micromachined Fabry-Perot optical fiber tip sensor for high-resolution temperature-independent measurement of refractive index," Opt. Express,Vol. 16, pp. 2252-2263 (2008).
26. T. Wei, Y. Han, H. Tsai, et al, "Miniaturized fiber inline Fabry-Perot interferometer fabricated with a femtosecond laser," Opt. Lett., Vol. 33, pp. 536-538 (2008).
27. T. Wei, Y. Han, Y. Li, et al, "Temperature-insensitive miniaturized fiber inline Fabry-Perot interferometer for highly sensitive refractive index measurement," Opt. Express, Vol. 16, pp. 5764-5769 (2008).
28. A. A. Said, M. Dugan, S. de Man, et al, "Carving fiber-top cantilevers with femtosecond laser micromachining," J. Micromech. Microeng., Vol. 18, 035005 (2008).
29. M. Yang, "Optical fiber devices fabricated by femtosecond laser micro-machining for sensing applications", The Hong Kong Polytechnic University, 2011.

30. S. Jeon, V. Malyarchuk, J. A. Rogers, et al, “Fabricating three dimensional nanostructures using two photon lithography in a single exposure step,” Opt. Express, Vol. 14, pp. 2300-2308 (2006).
31. B. N. Chichkov, C. Momma, S. Nolte, et al, “Femtosecond, picosecond and nanosecond laser ablation of solids,” Appl. Phys. A, Vol. 63, pp. 109-115 (1996).
32. S. Maruo, K. Ikuta, H. Korogi, “Submicron manipulation tools driven by light in a liquid,” Appl. Phys. Lett.,Vol. 82, pp. 133-135 (2003).
33. M. D. Perry, B. C. Strart, P. S. Banks, et al, “Ultrafast-pulse laser machining of dielectric materials,” J. Appl. Phys., Vol. 85, pp. 6803-6810 (1999).

Chapter 3

Sagnac loop interferometers based on Hi-Bi MNFs for comb filters

3.1 Introduction

Sagnac loop interferometer based on the Hi-Bi fiber has been investigated extensively in both theory and experiment because of their wide applications in many fields such as fiber optic gyros, fiber lasers and fiber sensors [1-6]. This is attributed to their advantages such as low cost, low loss, simple construction and polarization independence [7, 8]. As filters, they are key components in the processing of microwave and optical signals, as well as the wavelength division multiplexing communications with high stability and very good tunable characteristics. In this chapter, the basic theory of the fiber Sagnac loop interferometer based on the Jones matrix method is given in details, the transmission and reflection spectra characteristics of the Sagnac loop interferometer system is studied with theory and numerical simulations, and the Sagnac loop interferometer systems are used to measure the group birefringence of the fabricated Hi-Bi MNFs to verify the Hi-Bi MNF models and from compact comb filters.

3.2 Operation principle

The Sagnac loop interferometer [9] was designed based on the Sagnac effect which was firstly proposed by G. Sagnac in 1913. The basic configuration of Sagnac loop interferometer with one sections of Hi-Bi fiber is schematically shown in Fig. 3.1. It is a Sagnac loop interferometer comprising of a polarization controller, one section of Hi-Bi Fibers, and a SMF 3-dB directional coupler. The incident light is launched into the 3 dB coupler at the input port and split into c1ockwise- and counterclockwise-beams by the 3 dB coupler. The two beams pass through polarization controller and the Hi-Bi fibers from opposite directions and the transmitted and the reflected outputs are denoted as “T” and “R”. The fiber birefringence and the position of the cross-splicing point with respect to the middle of the loop determine the channel separation of this interferometer [10].

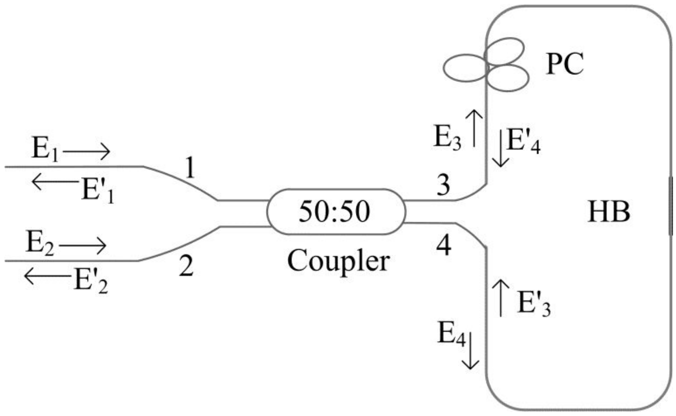

Fig. 3.1 Single section high birefringence fiber Sagnac loop interferometer

Let a linearly polarized light beam with azimuth angle of θ respect to the x axis is launched into port 1 of the coupler ($E_1 \neq 0$ $E_2=0$), which is split into two waves (E_3, E_4) described by

$$\begin{pmatrix} E_3 \\ E_4 \end{pmatrix} = \begin{pmatrix} \sqrt{1-k} & j\sqrt{k} \\ j\sqrt{k} & \sqrt{1-k} \end{pmatrix} \begin{pmatrix} E_1 \\ E_2 \end{pmatrix} \tag{3.1}$$

where κ is the coupled ratio. Being a transverse wave, the electric field vector must lie in the xy plane, and neglect the polarization converter effect of coupler, E_3 and E_4 can be decomposed into x and y components, given by

$$\begin{pmatrix} E_{3x} \\ E_{3y} \end{pmatrix} = \sqrt{1-k} \begin{pmatrix} E_{1x} \\ E_{1y} \end{pmatrix} = \sqrt{1-k} \begin{pmatrix} E_1 \cos\theta \\ E_1 \sin\theta \end{pmatrix} \tag{3.2}$$

$$\begin{pmatrix} E_{4x} \\ E_{4y} \end{pmatrix} = j\sqrt{k}\begin{pmatrix} E_{1x} \\ E_{1y} \end{pmatrix} = j\sqrt{k}\begin{pmatrix} E_1 \cos\theta \\ E_1 \sin\theta \end{pmatrix} \tag{3.3}$$

After traveling through the polarization controller,the polarization of the beam can be characterized as rotated by an angle of θ_1 and the electric field E31 in the clockwise direction can be represented as

$$\begin{pmatrix} E_{31x} \\ E_{31y} \end{pmatrix} = R(\theta_1)\begin{pmatrix} E_{3x} \\ E_{3y} \end{pmatrix} = \begin{pmatrix} \cos\theta_1 & \sin\theta_1 \\ -\sin\theta_1 & \cos\theta_1 \end{pmatrix}\begin{pmatrix} E_{3x} \\ E_{3y} \end{pmatrix} \tag{3.4}$$

After traveling through the Hi-Bi fiber, the beam is phase retarded and the electric field is expressed as

$$\begin{pmatrix} E_{32x} \\ E_{32y} \end{pmatrix} = \begin{pmatrix} e^{-j\Delta\phi/2} & 0 \\ 0 & e^{j\phi/2} \end{pmatrix}\begin{pmatrix} \cos\theta_1 & \sin\theta_1 \\ -\sin\theta_1 & \cos\theta_1 \end{pmatrix}\begin{pmatrix} E_{3x} \\ E_{3y} \end{pmatrix} \tag{3.5}$$

where $\Delta\varphi = 2\pi BL/\lambda$. Let θ_2 is the angle between the Hi-Bi fiber and the single mode fiber, the light wave travels through the Hi-Bi fiber to the single mode fiber, the axis is rotated by the angle θ_2, the electrical field of E3 arriving at the port 4 eventually evolve into

$$\begin{pmatrix} E_{3x}^{'} \\ E_{3y}^{'} \end{pmatrix} = \begin{pmatrix} \cos\theta_2 & \sin\theta_2 \\ -\sin\theta_2 & \cos\theta_2 \end{pmatrix}\begin{pmatrix} e^{-j\Delta\phi/2} & 0 \\ 0 & e^{j\Delta\phi/2} \end{pmatrix}\begin{pmatrix} \cos\theta_1 & \sin\theta_1 \\ -\sin\theta_1 & \cos\theta_1 \end{pmatrix}\begin{pmatrix} E_{3x} \\ E_{3y} \end{pmatrix} \tag{3.6}$$

It can be described as

$$E_3^{'} = R(\theta_2)JR(\theta_1)E_3 = M_{cw}E_3 \tag{3.7}$$

where

$$M_{cw} = \begin{pmatrix} \cos\theta_2 & \sin\theta_2 \\ -\sin\theta_2 & \cos\theta_2 \end{pmatrix}\begin{pmatrix} e^{-j\Delta\phi/2} & 0 \\ 0 & e^{j\Delta\phi/2} \end{pmatrix}\begin{pmatrix} \cos\theta_1 & \sin\theta_1 \\ -\sin\theta_1 & \cos\theta_1 \end{pmatrix} \tag{3.8}$$

Assume that the input beam from the other arm of the coupler has the identical components magnitude. Analogously, the same result for the anti-clockwise propagating beam can be obtained by using the same algebraic manipulation

$$E_4^{'} = R(-\theta_1)JR(-\theta_2)E_4 = M_{acw}E_4 \tag{3.9}$$

where

$$M_{cw} = \begin{pmatrix} \cos\theta_1 & -\sin\theta_1 \\ \sin\theta_1 & \cos\theta_1 \end{pmatrix} \begin{pmatrix} e^{-j\Delta\phi/2} & 0 \\ 0 & e^{j\Delta\phi/2} \end{pmatrix} \begin{pmatrix} \cos\theta_2 & -\sin\theta_2 \\ \sin\theta_2 & \cos\theta_2 \end{pmatrix} \tag{3.10}$$

After reentering the coupler, the electrical field at the out port are shown as

$$\begin{pmatrix} E_{1x}^{'} \\ E_{2x}^{'} \end{pmatrix} = \begin{pmatrix} \sqrt{1-k} & j\sqrt{k} \\ j\sqrt{k} & \sqrt{1-k} \end{pmatrix} \begin{pmatrix} E_{4x}^{'} \\ E_{3x}^{'} \end{pmatrix} \tag{3.11}$$

$$\begin{pmatrix} E_{1y}^{'} \\ E_{2y}^{'} \end{pmatrix} = \begin{pmatrix} \sqrt{1-k} & j\sqrt{k} \\ j\sqrt{k} & \sqrt{1-k} \end{pmatrix} \begin{pmatrix} E_{4y}^{'} \\ E_{3y}^{'} \end{pmatrix} \tag{3.12}$$

The reflected output power at the port 1 and the transmitted output power at the port 2 can be described separately

$$P_1 = \left|E_{1x}^{'}\right|^2 + \left|E_{1y}^{'}\right|^2, \qquad P_2 = \left|E_{2x}^{'}\right|^2 + \left|E_{2y}^{'}\right|^2 \tag{3.13}$$

The light power of the incident beam is

$$P_0 = \left|E_{1x}\right|^2 + \left|E_{1y}\right|^2 \tag{3.14}$$

The reflectivity and transmission of Sagnac loop interferometer are presented separately by

$$R = P_1 / P_0 \qquad\qquad T = P_2 / P_0 \tag{3.15}$$

We can obtained the reflected output and the transmitted output of Sagnac loop interferometer with Hi-Bi fiber

$$R = 4k(1-k)[1-\sin^2(\theta_1+\theta_2)\cos^2(\Delta\phi/2)] \tag{3.16a}$$

$$T = (1-2k)^2 + 4k(1-k)\sin^2(\theta_1+\theta_2)\cos^2(\Delta\phi/2) \tag{3.16b}$$

Eq. 3.16 shows that the reflectivity and transmission as functions of wavelength depend on the rotation angle of polarization controller and the birefringence and length of the Hi-Bi fiber, independent of the polarization of the incident light. Sagnac loop interferometer can be assumed as a device with input polarization independence.

3.3 Group birefringence measurement of Hi-Bi MNFs

The two Hi-Bi MNFs samples fabricated in section 2 were connected in to the Sagnac loop interferometer system the get the transmission spectrums shown in Fig. 3.3, the envelop shape of the interference pattern was observed to result from the 3 dB coupler, the coupled ration of which is a function of wavelength. From the measured transmission spectrums, the group birefringence can be obtained by using the following equation[11-14]

$$\Delta\lambda_0 = \frac{\lambda_0^2}{B_g L} \tag{3.29}$$

where

$$B_g = B - \lambda \frac{dB}{d\lambda} \tag{3.30}$$

B_g is called group birefringence, which includes the wavelength dispersion λ_0 is a certain wavelength, both with effective length of ~ 8 mm.

Based on the phase birefringence B of the fiber samples H_1 and H_2 are numerically modeled by using the following parameters: (1) H_1, b/a=0.72 and $2a$~3.4μm; (2) H_2, b/a=0.9 and $2a$~0.9 μm. Based on the numerical model, the group birefringence B_g can be calculated with Eq. (3.30). The calculated and the measured group birefringences agree well with each other for both samples.

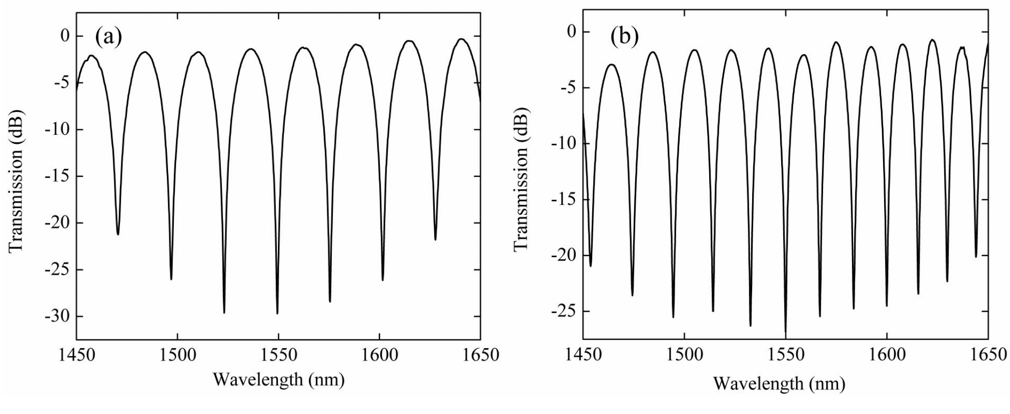

Fig. 3.2 Measured transmission spectrums for two Hi-Bi MNF sample H_1 and H_2

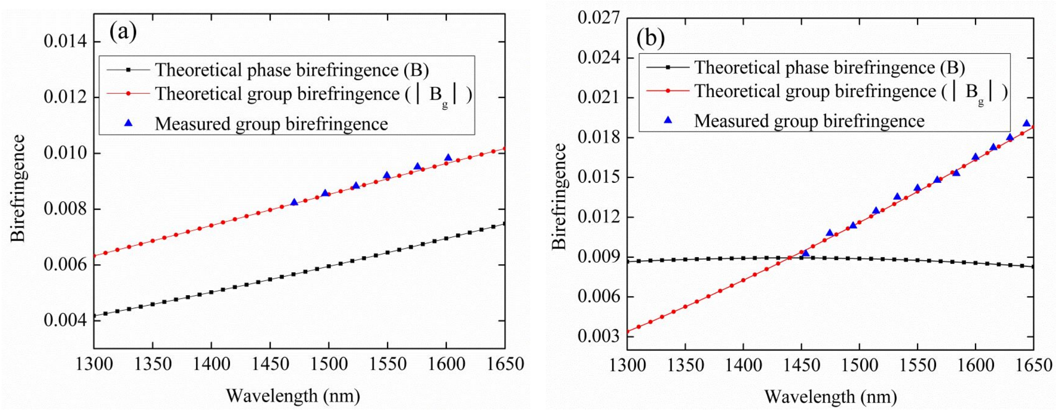

Fig. 3.3 Group birefringence B_g and phase birefringence B as functions of wavelength for Hi-Bi MNF sample (a) H_1 and (b) H_2.

3.4 Comb filters based on Sagnac loop interferometers with two-stage Hi-Bi MNFs

Optical comb filters as multi-channel filters have been studied intensively for application in wavelength division multiplexing (WDM) communication systems [15], and filters with flat-top are particularly attractive for DWDM systems due to signal fidelity and tolerance of signal wavelength drift. Especially, all-fiber comb filters based on a Sagnac loop interferometer are popularly used for all-optical signal processing and multi-wavelength fiber lasers [16-18] due to lower insertion loss and better performance. A number of techniques for realizing comb filters have been reported, including polarization-diversity loop configuration [19], Mach-Zehnder (M-Z) [20] and Fabry-Perot [21] interferometers, photorefactive gratings [22], and a Sagnac loop interferometer formed by cascading different pieces of fibers placed inside a fiber loop mirror (Sagnac loop interferometer) [23]. The use of two cascaded Hi-Bi MNFs instead of a single MNF allows more flexibility in controlling the transmission/reflection characteristics of the Sagnac loop interferometer. The length of Hi-Bi MNFs is on the order of centimeters, one or even more two orders of magnitude shorter than the conventional Hi-Bi fiber-based Sagnac loop interferometer devices

We investigate the use of two-stage Hi-Bi MNF-based Sagnac loop interferometers for tunable comb filters theoretically and experimentally. Two different configurations were studied. One incorporates a single piece of twisted Hi-Bi MNF in a Sagnac loop, while the other includes two pieces of Hi-Bi MNFs cascaded along a fiber with a rotation of their birefringence axes. This work on MNFs may result in novel applications such as wavelength-scale light transmission and interconnection which are useful for photonic integration, computing, and nano-scale sensing.

3.4.1 Numerical modeling

A Sagnac loop interferometer of two-stage hi-bi MNFs is schematically shown in Fig.1, which includes two Hi-Bi fibers, namely HB1 and HB2, each length of L1 and L2. This system relies on two hi-bi fibers that are connected together at different angle of rotation in relation with the birefringence axes. A mathematical model of the interferometer is constructed on hi-bi fiber segment lengths, rotation angle in the birefringence axes and the birefringence of the hi-bi fibers.

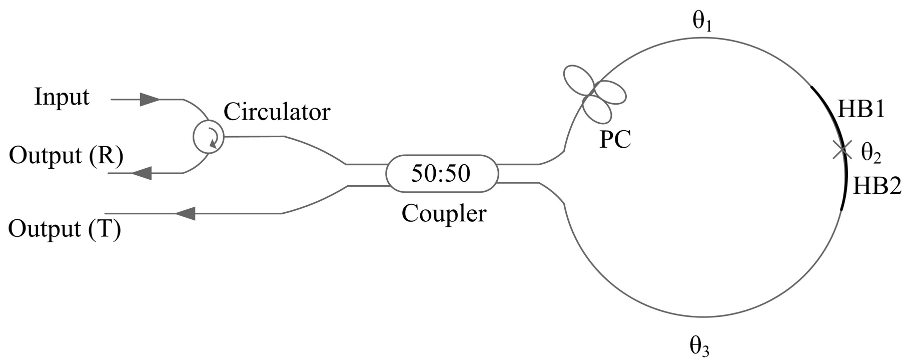

Fig. 3.5 Schematic diagram of the Sagnac loop interferometer with two-stage Hi-Bi fibers.

The Sagnac loop interferometer may be theoretically analyzed by the use of the

Jones Matrix method. With a 3-dB coupler, the Sagnac loop interferometer functions as a comb filter and the relationship between input and output is described as:

$$\begin{bmatrix} [E_{out-R}] \\ [E_{out-T}] \end{bmatrix} = [J_c] \begin{bmatrix} R(-\theta_1)J_1R(-\theta_2)J_2R(-\theta_3) & 0 \\ 0 & R(\theta_3)J_2R(\theta_2)J_1R(\theta_1) \end{bmatrix} [J_c] \begin{bmatrix} [E_{in}] \\ [0] \end{bmatrix} \quad (3.17)$$

In Eq. 3.17 $[E_{in}]$ denotes the input field, which is a 2D vector. J_c, $R(\theta_n)$ and J_n represent respectively the matrix of the fiber coupler, the rotation of birefringence axes, and the additional phase difference induced by Hi-Bi MNFs.

$$J_c = \begin{bmatrix} \sqrt{0.5} & j\sqrt{0.5} \\ j\sqrt{0.5} & \sqrt{0.5} \end{bmatrix},\ R(\theta) = \begin{pmatrix} \cos\theta & \sin\theta \\ -\sin\theta & \cos\theta \end{pmatrix},\ J_n = \begin{bmatrix} e^{-j\Delta\varphi_n/2} & 0 \\ 0 & e^{j\Delta\varphi_n/2} \end{bmatrix} \quad (3.18)$$

where θ represents the angle between the birefringent axes of the two MNFs, $\Delta\varphi_n = 2\pi B_n L_n / \lambda$ (n=1, 2) is the phase difference generated due to birefringence, L is the length of the Hi-Bi MNFs, and B is the effective phase birefringence. The transfer functions at the transmitted and the reflected output is expressed as:

$$T = \left[\cos\left(\frac{\pi\Delta n_1 L_1 + \pi\Delta n_2 L_2}{\lambda} \right) \cos\theta_2 \sin(\theta_1 + \theta_3) + \cos\left(\frac{\pi\Delta n_1 L_1 - \pi\Delta n_2 L_2}{\lambda} \right) \sin\theta_2 \cos(\theta_1 + \theta_3) \right]^2 \quad (3.19)$$

$$R = 1 - T \quad (3.20)$$

Next, we study the influence of the polarization controller and the phase difference induced by Hi-Bi fibers on the output spectrum, which is calculated by the above equations. When the lengths and the birefringence of the two Hi-Bi are equal, Equation 3.19 is simplified to:

$$T = \left[\cos\left(\frac{\pi\Delta n_1 L_1 + \pi\Delta n_2 L_2}{\lambda} \right) \cos\theta_2 \sin(\theta_1 + \theta_3) \right]^2 \quad (3.21)$$

$$T=\left[\cos\left(\frac{\pi\Delta n_1 L_1+\pi\Delta n_2 L_2}{\lambda}\right)\cos\theta_2\right]^2$$

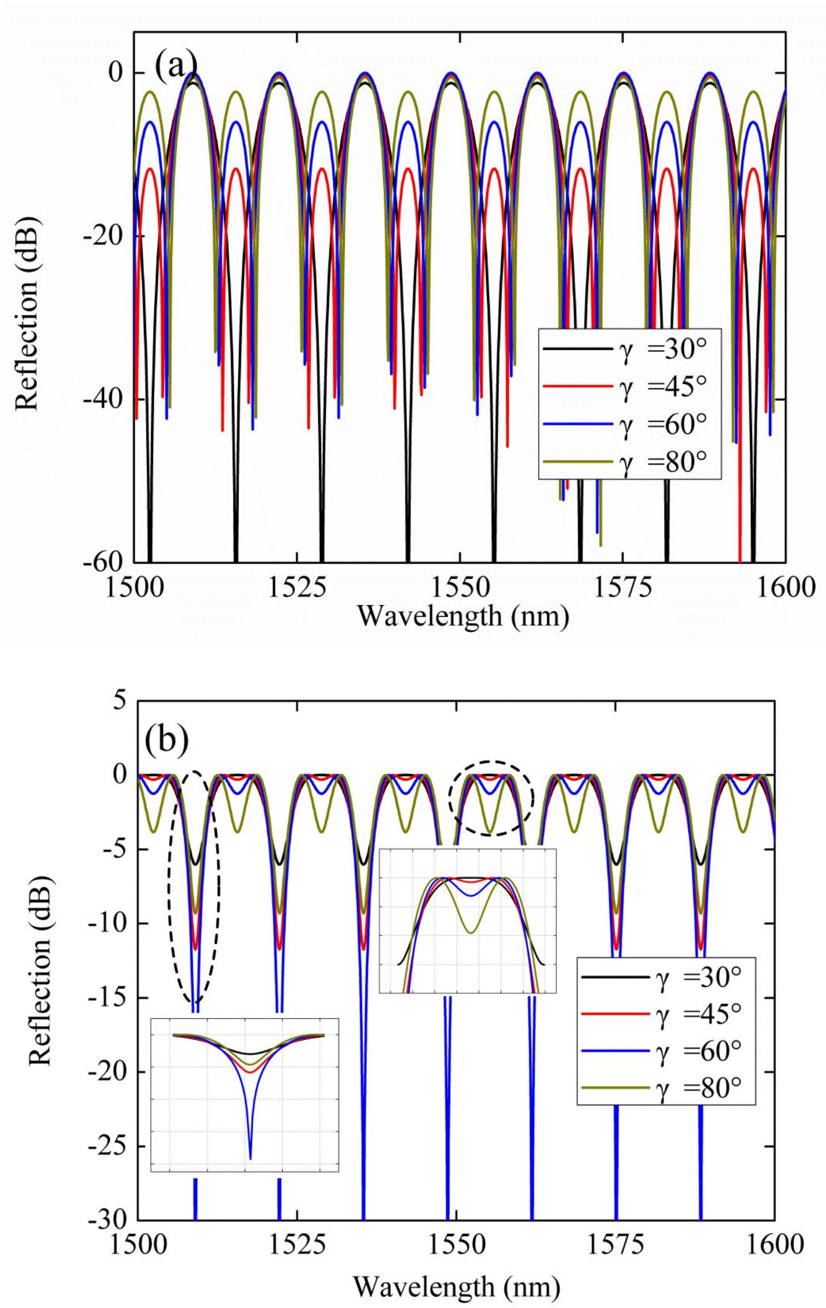

Fig. 3.6 Calculated reflection spectra for different γ with L_1=L_2=2 cm, $\theta_2=30°$

The spectrum characteristics are determined by $\cos\left(\frac{\pi\Delta n_1 L_1+\pi\Delta n_2 L_2}{\lambda}\right)$. The transmission spectrum band is not flat but always having a cosine shape, and the reflection spectra can realize the flat-top output, as shown in Fig. 3.6. The rotation angle between the birefringent axes of the two Hi-Bi fibers are set to be $\pi/6$, and the output spectra with different $\gamma = \theta_1 + \theta_3$ by adjusting polarization controller are simulated in Fig. 3.6, γ does not change the spacing between the two maximum wavelength, while change the peak-to-notch ratio and the top flatness of the reflection spectrum. The peak-to-notch ratio firstly increase and then decrease with the γ increase with the stable rotation angle of θ_2, meanwhile the top flatness of the spectrum becomes worse with the γ increase.

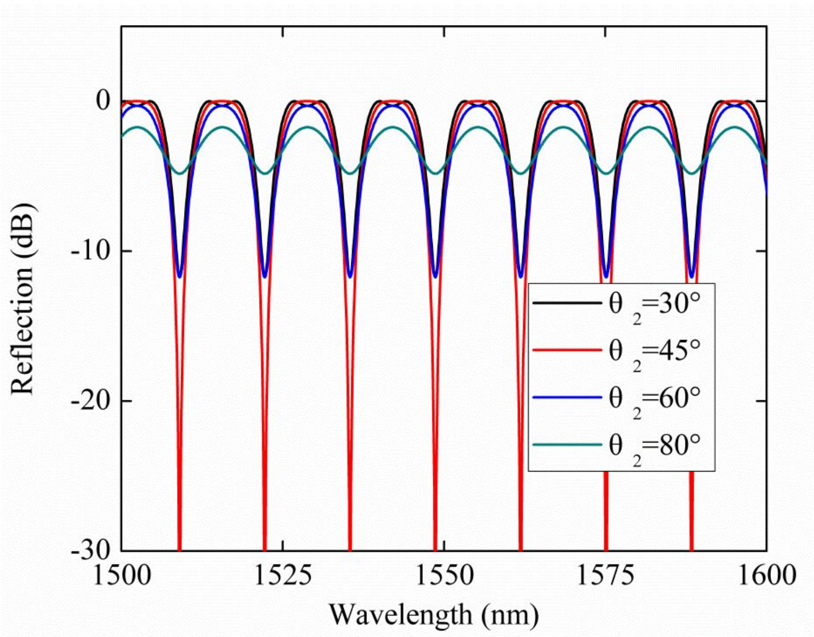

Fig. 3.7 Calculated reflection spectra for different angle between the birefringent axes θ_2 with L_1=L_2=2 cm, and $\gamma = 45°$.

The transmission spectrum characteristics with different angle between the birefringent axes is also simulated with $\gamma = 45°$, θ_2 does not change the spacing between the two maximum wavelength, changing the peak-to-notch ratio and the top flatness of the reflection spectrum. The optimal peak-to-notch ratio and top flatness of the reflection spectrum is achieved with $\gamma = 45°$ and $\theta_2 = 45°$.

3.4.2 Fabrication and experimental results

In this chapter, we investigate the use of Hi-Bi MNF-based Sagnac loop interferometers for comb filters [24]. Two different configurations are studied. One incorporates a single piece of twisted Hi-Bi MNF in a Sagnac loop, while the other includes two pieces of Hi-Bi MNFs cascaded along a fiber with a rotation of their birefringence axes, as shown in Fig. 3.8. This work on MNFs may result in novel applications such as wavelength-scale light transmission and interconnection which are useful for photonic integration, computing, and nano-scale sensing.

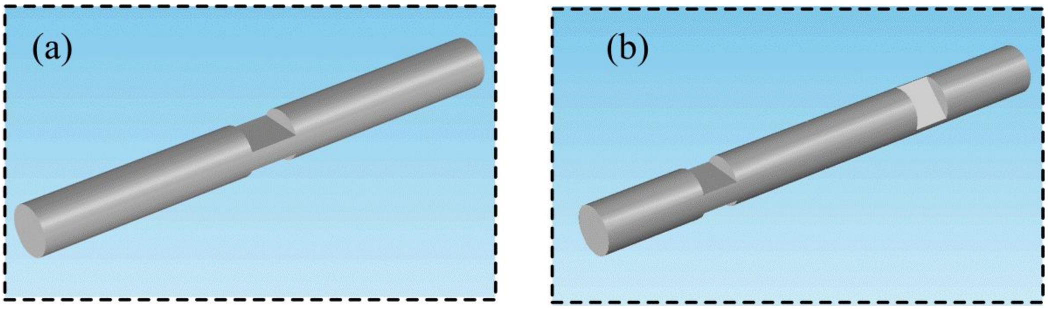

Fig. 3.8 (a) Artistic view of the idealized "processed" one section SMF and (b) Artistic view of the idealized "processed" SMF section from which cascaded Hi-Bi MNFs are taper-drawn.

Fig. 3.9 shows the measured transmission spectra of a Sagnac loop interferometer containing a 2 cm long Hi-Bi elliptical MNF with a diameter of ~2.8 μm for its major axis, the insertion loss of this MNF is less than 0.2 dB. From the upper curve birefringence of the MNF is estimated to be about 8.5×10^{-3} [25] (at wavelength of 1550 nm).

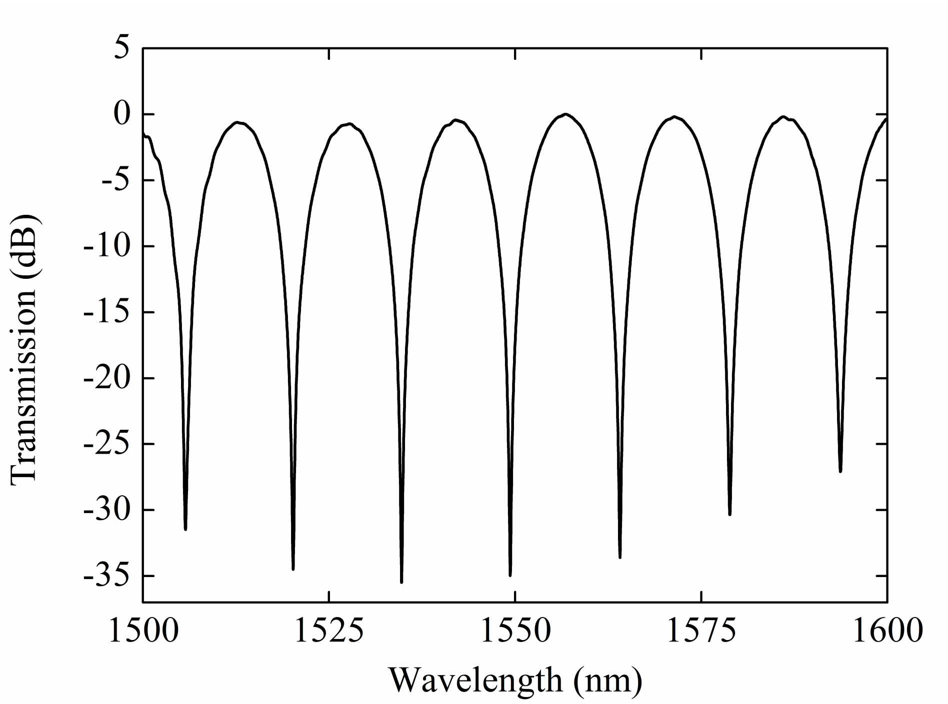

Fig. 3.9 Transmission spectrum of a Sagnac loop interferometer system with one section of Hi-Bi MNF

The use of two cascaded MNFs in a Sagnac loop interferometer would allow more flexibility in the design of comb filters. Fig. 3.10 shows the calculated reflection spectra for two cascaded MNFs with different parameters. The calculation is based on Eq. (3.31) and Eq. (3.32) with $\Delta n_1 = \Delta n_2 = 8.5\times10^{-3}$ (at wavelength of 1550 nm). For Fig. 3.10 (a), we used L_1=L_2=1 cm and $\theta_1 + \theta_3 = 60°$, while the angle between the two Hi-Bi MNFs (θ_2) was varied from 30° to 75°. Fig. 3.10 (b), L_1=L_2 =2 cm and $\theta_2 = 30°$ were used and $\theta_1 + \theta_3$ was varied from 35° to 80°.

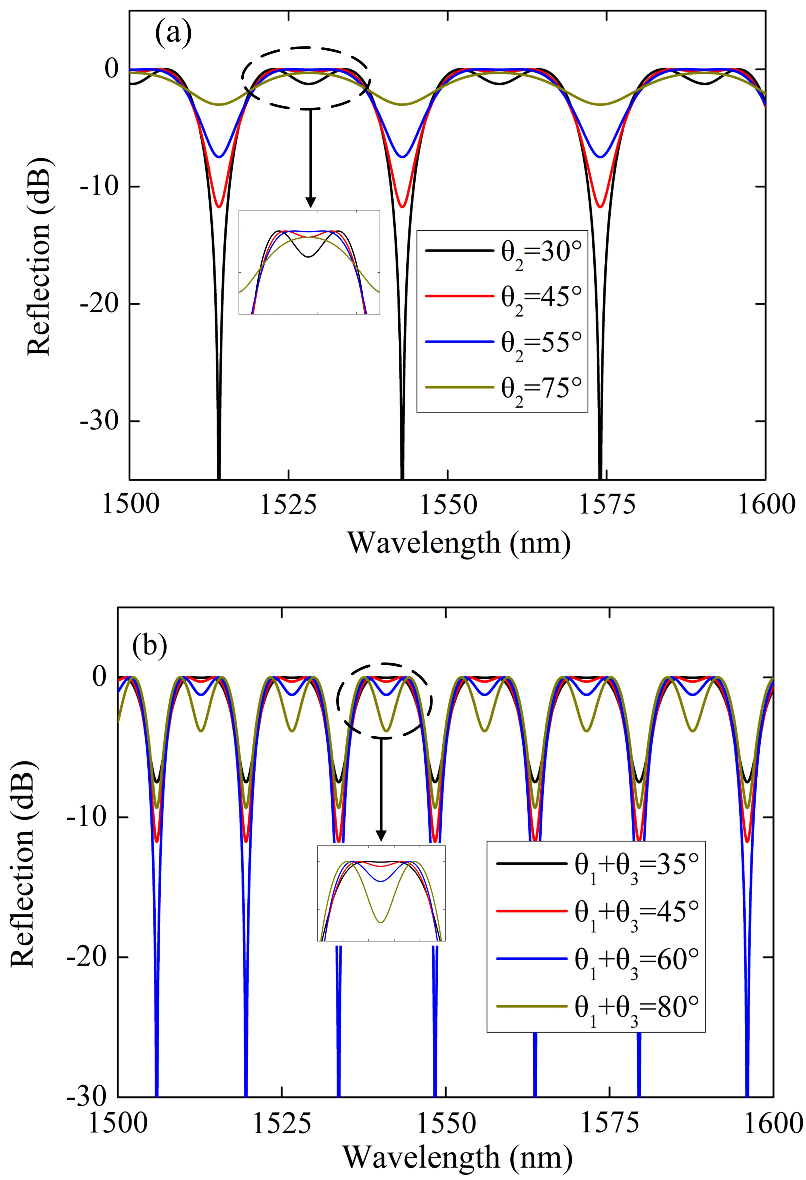

Fig.3.10 Calculated reflection spectra for (a) L_1=L_2=1 cm, $\theta_1+\theta_3=60°$, and (b) L_1=L_2=2 cm , $\theta_2=30°$

The calculated results illustrate that for the reflection spectra, θ_2 and $\theta_1+\theta_3$ affect the flatness of the wave top and the peak-to-notch contrast ratio while the birefringence and the length of Hi-Bi MNFs determines the channel spacing, indicating comb filters with desired properties may be designed by selecting the length and birefringence of the MNFs, as well as the angle of rotation of the birefringent axes.

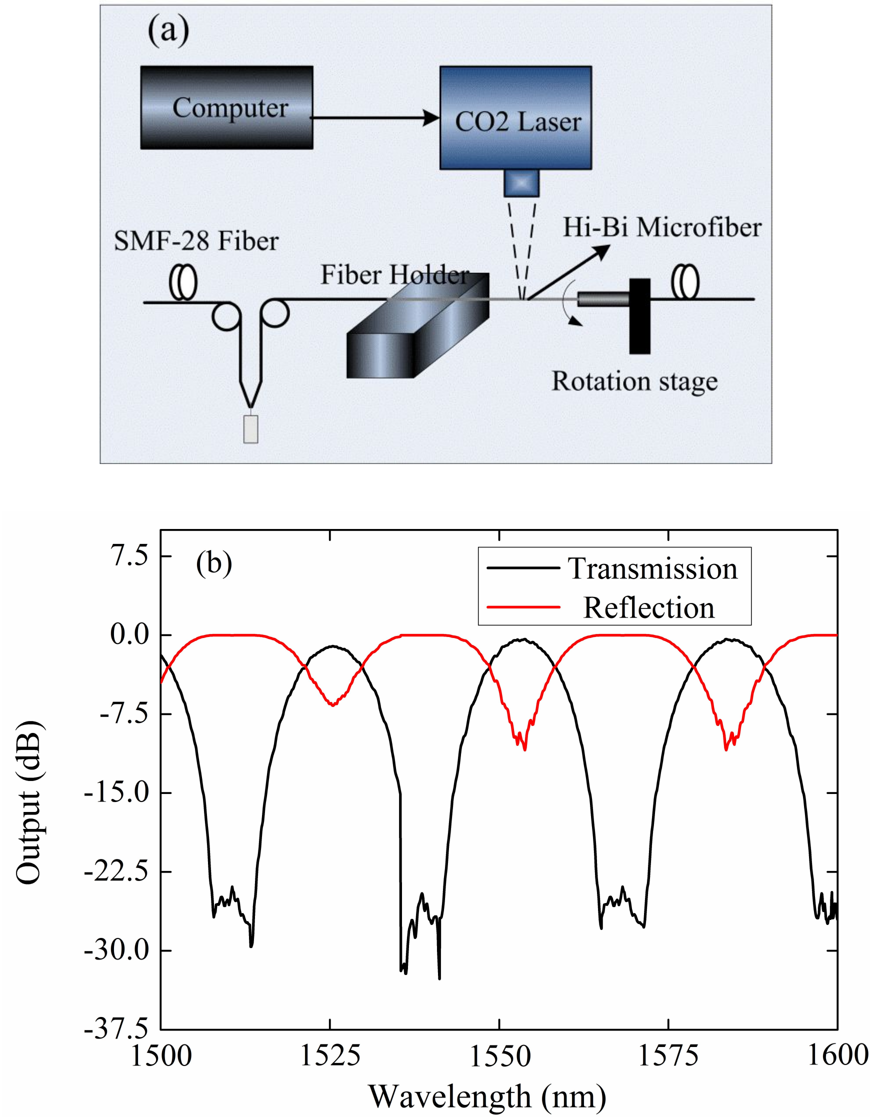

Fig. 3.11 (a) Experimental setup to twist one section of Hi-Bi MNFs. (b) Transmission and reflection spectra

Experiments were conducted with Sagnac loop interferometers containing two cascaded Hi-Bi MNFs. The first Sagnac loop interferometer used one section 2 cm long tapered Hi-Bi MNF with a 55° twist angle in the middle, equivalent to two cascaded 1 cm long MNFs with an angle between the birefringence axes of $\theta_2 = 55°$.

The cascaded MNF sample was prepared by the following procedure. The 2 cm long Hi-Bi MNF is fixed to the middle between two clamps with 12 cm separation between them, one of the clamps is fixed to a motor-driving rotation stage through which a 120 degree rotation is applied, as shown in Fig. 3.11 (a). The CO_2 laser beam with a spot size of ~40 μm in diameter is scanned transversely across the fiber at the middle point between the clamps, resulting in local heating of the fiber and inducing a permanent twist of the fiber at the mid-point with a twist angle ~55°. The average power of CO_2 laser was set to 0.015 W, which is sufficient to induce a permanent twist but with little deformation on the surface of the MNF. The loss due to twist was found to be ~0.2 dB.

The transmission and reflection spectra of this Sagnac loop interferometer are shown in Fig. 3.12, which agrees well with the calculated spectrum for $\theta_1 + \theta_3 = 60°$ and $\theta_2 = 55°$. The comb filter has channel spacing of ~32 nm and peak-to-notch contrast ratio of ~10 dB.

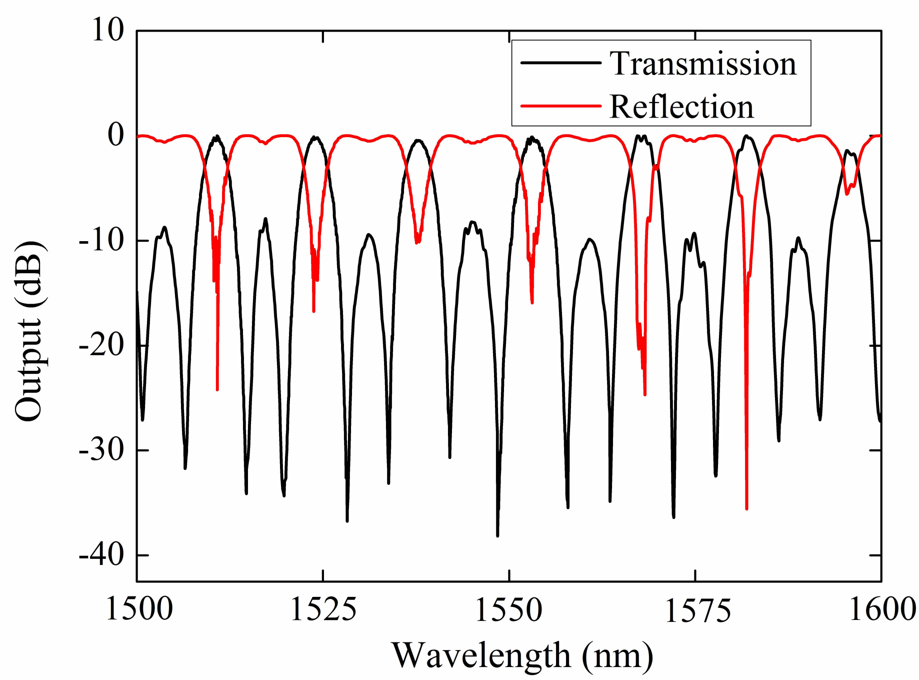

Fig. 3.12 Measured transmission and reflection spectra for a Sagnac loop interferometer containing two cascaded Hi-Bi MNFs.

The second Sagnac loop interferometer contains two 2 cm long Hi-Bi MNFs operated on the same SMF, which is much simple than the first one, and the rotated angle was induced in the pre-processed SMF shown in Fig. 3.8. The angle between the birefringent axes is $30°$. Fig. 3.12 shows measured transmission and reflection spectra of the second Sagnac loop interferometer, which is close to the calculated results for $\theta_2 = 30°$ and $\theta_1 + \theta_3 = 60°$.

3.5 Summary

In this chapter, we have analyzed Sagnac loop interferometer based on hi-bi fibers theoretically with the Jones matrix method to show that reflection and transmission property of the Sagnac loop interferometer. The Sagnac loop system containing a single Hi-Bi MNF and two cascaded Hi-Bi MNFs are demonstrated for comb filters. Compared with Sagnac loop interferometer comb filters based on the conventional Hi-Bi fibers [26], the current devices need very short length of MNFs and the transmission/reflection spectra may be designed more flexible. The device could be useful for optical signal processing and switching, power equalization, and management for WDM network.

References of Chapter 3

1. G. A. Pavlath and H. J. Shaw, “Birefringence and polarization effects in fiber gyroscopes,” Appl. Opt., Vol. 21, pp. 1752–1757 (1982).
2. W. K. Burns and A. D. Kersey, “Fiber-optic gyroscopes with depolarized light,” J. Lightwave Technol., Vol. 10, pp. 992–999 (1992).
3. B. Szafraniec and J. Blake, “Polarization modulation errors in all-fiber depolarized gyroscopes,” J. Lightwave Technol., Vol. 12, pp. 1679–1684 (1994).

4. M. Campbell, G. Zheng, A. S. Holmes-Smith, and P. A. Wallace, “A frequency-modulated continuous wave birefringenfibre-optic strain sensor based on a Sagnac ring configuration,” Meas. Sci. Technol., Vol. 10, pp. 218–224 (1999).
5. E. De La Rosa, L. A. Zenteno, A. N. Starodumov, and D. Monzon, “All-fiber absolute temperature sensor using an unbalanced high-birefringence Sagnac loop,” Opt. Lett., Vol. 22, pp. 481–483 (1997).
6. A. N. Starodumov, L. A. Zenteno, D. Monzon, and E. De La Rosa, “Fiber Sagnac interferometer temperature sensor,” Appl. Phys. Lett.,Vol. 70, pp. 19–21 (1997).
7. Jinno, M. and T. Matsumoto, “Nonlinear Sagnac interferometer switch and its applications," IEEE J. Quantum Electron., Vol. 28, pp. 875-882 (1992).
8. Mirza, M. A. and G. Stewart, “Theory and design of a simple tunable Sagnac loop filter for multiwavelength fiber lasers," Appl. Opt., Vol. 47, pp. 5242-5252 (2008).
9. Valiv, R. W. Shorthill, “Fiber ring interferometer,” Appl. Opt.., Vol. 15, pp. 1099-1100 (1979).
10. A. N. Starodumov, L. A. Zenteno, D. Monzon, and E. De La Rosa, “Fiber Sagnac interferometer temperature sensor,” Appl. Phys. Lett., vol. 70, pp. 19–21 (1997).
11. S. C. Rashleigh, "Measurement of fiber birefringence by wavelength scanning: effect of dispersion," Opt. Lett., Vol. 8, pp. 336-338 (1983).
12. X. Chen, M.-J. Li, N. Venkataraman, M. Gallagher, W. Wood, A. Crowley, J. Carberry, L. Zenteno, and K. Koch, "Highly birefringent hollow-core photonic bandgap fiber," Opt. Express, Vol. 12, pp. 3888-3893 (2004).

13. J. R. Folkenberg, M. D. Nielsen, N. A. Mortensen, C. Jakobsen, and H. R. Simonsen, "Polarization maintaining large mode area photonic crystal fiber," Opt. Express, Vol. 12, pp. 956-960 (2004).
14. H. F. Xuan, W. Jin, M. Zhang, J. Ju, and Y. B. Liao, "In-fiber polarimeters based on hollow-core photonic bandgap fibers," Opt. Express, Vol. 17, pp. 13246-13254 (2009).
15. J. W. Wu, X. D. Tian, and H. B. Bao, "A designed model about amplification and compression of picosecond pulse using cascaded soa and NOLM device," Progress In Electromagnetics Research, Vol. 76, pp. 127-139 (2007).
16. G Y Sun, Dae Seung Moon, A. X. Lin, W. T. Han, and Y Chung, "A subnanosecond polarization-independent tunable filter/wavelength router using a Sagnac interferometer," Opt. Express, Vol. **16**, pp. 3652-3658 (2008).
17. S. Hu, L. Zhan, Y. J. Song, W. Li, S. Y. Luo, andY. X. Xia, "Switchable multiwavelength erbium-doped fiber ring laser with a multisection high-birefringence fiber loop mirror," IEEE Photon. Technol. Lett.,Vol. 17, pp. 1387-1389 (2005).
18. G. Rossi, o. Jerphagnon, B. E. Olsson, and D. J. Blumenthal, "Optical SCM data extraction using a fiber-loop mirror for WDM network systems," IEEE Photon. Technol. Lett., Vol. **12**, pp. 897-899 (2000).
19. Y. W. Lee, K. J. Han, B. Lee and J. Jung, "Polarization independent all-fiber multiwavelength-switchable filter based on a polarization-diversity loop confguration", Opt. Express, Vol. 25, pp. 3359-3364 (2003).
20. A. P. Luo, Z. C. Luo, W C. Xu and H. Cui, "Wavelength switchable fat-top all-fiber comb filter based on a double-loop Mach-Zehnder interferometer", Opt. Express, Vol. 6, pp. 6056-6063 (2010).

21. M. Menard and A. G Kirk, "Integrated Fabry-Perot comb flters for optical space switching", J. Lightwave Technol., Vol. 28, pp. 768-775 (2010).
22. I. Navruz, N. F. GuIer, "A novel technique for optical dense comb filters using sampled fiber Bragg gratings", Optical Fiber Technology, Vol. 14, pp. 114-118 (2008).
23. K. L. Lee, M. P. Fok, S. M. Wan and C. Shu, "Optically controlled Sagnac loop comb filter", Opt. Express, Vol. 25, pp. 6335-6340 (2004).
24. W. Jin, C. Wang, H. Xuan, and W. Jin, "Tunable comb filters and refractive index sensors based on fiber loop mirror with inline high birefringence MNF," Opt. Lett., Vol. 38, pp. 4277-4280 (2013).
25. Haifeng Xuan, Jian Ju, and Wei Jin, "Highly birefringent optical MNFs," Opt. Express, Vol. 18, pp. 3828-3839 (2010).
26. Jing Wang, Kai Zheng, Jian Peng, Lisong Liu, Jian Li, and Shuisheng Jian, "Theory and experiment of a fiber loop mirror filter of two-stage polarization-maintaining fibers and polarization controllers for multiwavelength fiber ring laser," Opt. Express, Vol. 17, 10573-10583 (2009).

Chapter 4

Photonic microcells

4.1 Introduction

In this chapter, we report a simple and low cost method for fabricating encapsulated MNF photonic microcells. The MNFs are made by bi-tapering a conventional SMFs and suspended along the center area of a capillary tube. The MNFs are kept straight within the capillary while their SMF pigtails are glued to the two ends of the capillary. The encapsulation does not change the optical property of the MNF but the capillary tube protects the MNF from external disturbance and contamination. Side holes are made on the capillary wall and act as ingress/egress channels for sample liquids or gases. The photonic microcells of such made are robust and stable, and can be easily integrated into standard fiber-optic circuits with low loss, making the MNF-based devices more practical for real-world applications. To illustrate the potential applications of such photonic microcells, we demonstrated refractive index (RI) sensors by incorporating an encapsulated Hi-Bi MNF photonic microcell into a fiber-optic Sagnac loop interferometer and achieved RI sensitivity of 2,024 nm per RI unit (RIU) around RI=1 and 21,231 nm/RIU around RI=1.33. Such microcells may be used as low loss evanescent-wave-coupled optical absorption, florescent and gain cells, photoacoustic cells, and so on.

4.2 Experimental setup for encapsulating MNF

The experimental setup for fabricating encapsulated MNF photonic microcells is schematically shown in Fig. 4.1. An additional three-axis translation stage with a tube holder is used to support a capillary tube within which the MNF will be housed. The SMF is firstly inserted into the capillary mounted on the tube holder and the SMF tails on the two sides of the capillary are clamped to two fiber holders on the tapering rig. Before tapering, the position of the capillary is adjusted carefully to ensure the SMF is located approximately along the central axis of the capillary tube. The capillary is initially moved away from the central flame-brushing region so that the MNF taper can be made by the standard taper-draw process. After the tapering process is completed, the capillary is carefully moved back to cover the tapered region. The length of the selected capillary is longer than the tapered region so that the two ends of the capillary can be glued to the SMF pigtails without disturbing the MNF section. The capillary used in our experiment has inner and outer diameters of ~660 μm and ~900 μm, respectively. To ensure the MNF is suspended along the central axis of the capillary, two shorter capillaries (~3 mm in length) with inner and outer diameters of ~300 μm and 500 μm were inserted to the two ends of the larger capillary and they are fixed together by glue. The SMF and the capillary assembly was then glued together and the MNF was then encapsulated inside the capillary tube. Fig. 4.2 shows a sketch, photos and microscope images of a photonic microcell and the details of the MNF inside the capillary are shown in Fig. 4.2 (c) and 4.2 (d), and the MNF is straight and suspended along the central axis of the capillary tube.

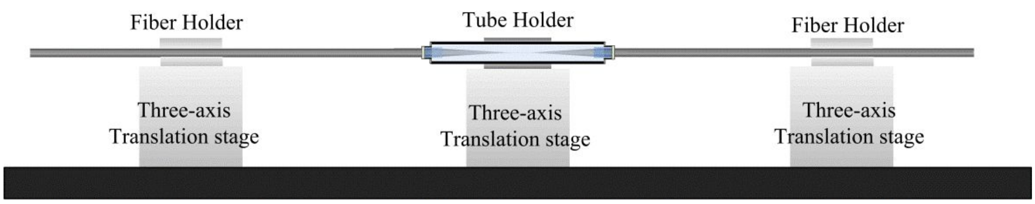

Fig. 4.1 Experimental setup to insert the MNF into the capillary tube.

During the process of tapering and encapsulation, the transmission spectrum of the device is monitored by connecting the input and output ends of the SMF, respectively, to a broadband light source (BLS) and an optical spectrum analyzer

(OSA). A large transmission loss was observed if the MNF was broken or adhered to the inner wall of the capillary. A loss of ~0.2 dB was achieved with a photonic microcell with an encapsulated 5 cm-long and ~1 μm-diameter photonic microcell.

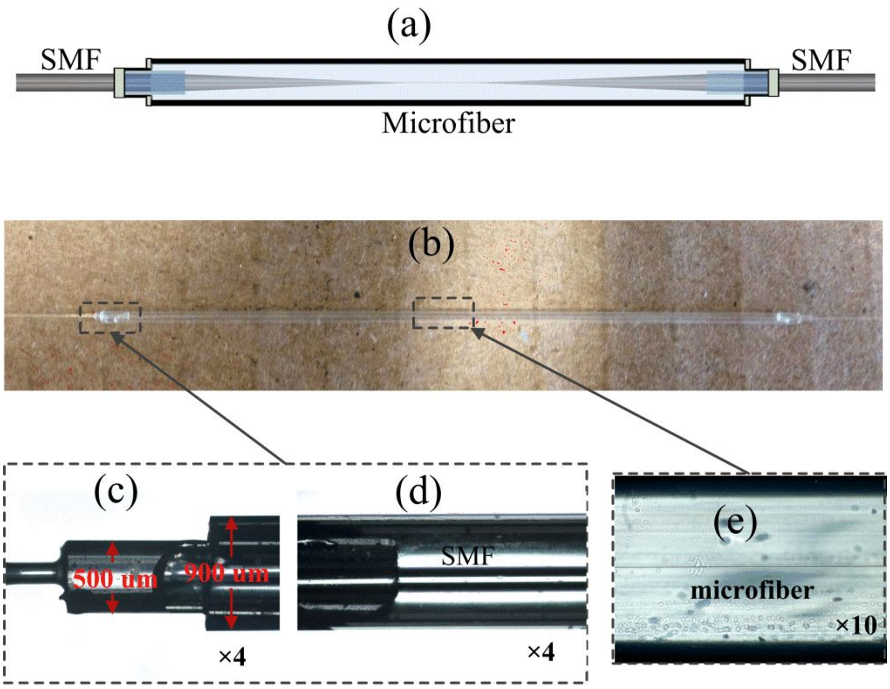

Fig. 4.2 (a) Schematic and (b) photo of a photonic microcell with an encapsulated MNF; (c-d) microscope images of the photonic microcell: (c) the external and (d) internal of the capillary end, (e) the MNF inside the capillary.

There have been researches on the method and effect of embedment of MFs/MF-based devices, most of them encapsulated MFs with some low-loss, low-refractive-index material.. Although some coatings such as Teflon [1, 2], and EFORON PC-373 [3] could improve robustness, stability and provide some protection against degradation, they also brought some challenges, including complicated and difficult fabrication resulting in low efficience in coating MFs, encapsulation-induced loss (~2 dB/mm for 900 nm diameter [1] and 0.4 dB/mm for 1000 nm diameter [2] at 1550 nm wavelength for teflon coating), undesirable changes in light confinement and dispersion [1, 3] due to the high refractive index of the encapsulant (teflon, n=1.31 and EFORON PC-373, n=1.38), and evanescent sensing disability (encapsulation prevented evanescent sensing unless the encapsulant was thinned to allow the evanescent field to reach the external medium). Even if the silica aerogel coating [4] has low refractive index (typically 1.01-1.05) and allows evanescent sensing for gases, however, the brittle aerogel block does not eliminate changes in optical property and evanescent sensing in liquid of MFs. The PMCs overcomes the aforementioned limitations, the encapsulation does not change the optical properties of the MF but provide a miniature container for sample liquids or gases, avoiding the use of bulky gas or liquid chambers.

4.3 Encapsulated Hi-Bi MNF photonic cells and sensors

Sagnac loop interferometer has been shown to be an attractive device for optical fiber sensing [5] and possessing many advantages including simple design, ease of manufacture, high sensitivity and low cost., Besides the gyroscope application [6], The Sagnac loop interferometer has been used as temperature sensors [7, 8], strain sensors [9-12] and bio-chemical sensors [13, 14] where two different polarization modes exhibit different responses to measurands.

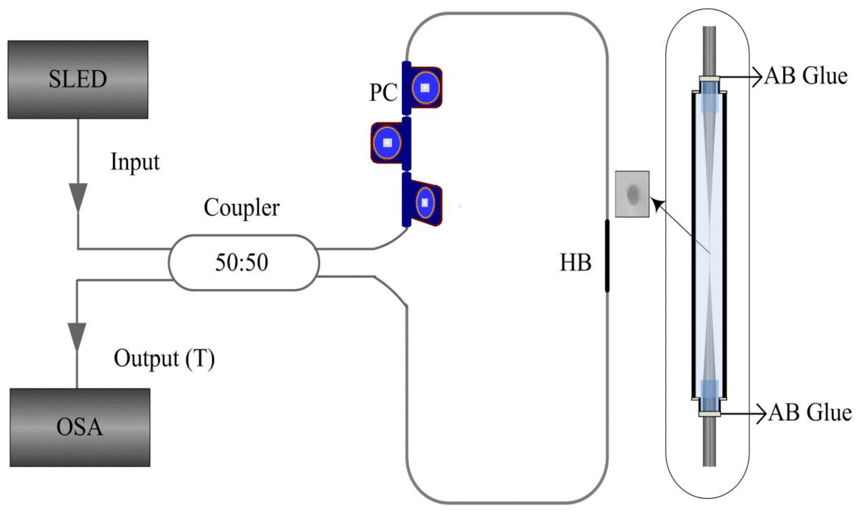

Fig. 4.3 Experimental setup for sensing measurement. Insert: Schematic diagram of the sealed Hi-Bi MNF in a pressure tube.

With the above described technique, we fabricated photonic microcells with a Hi-Bi MNF encapsulated inside a silica capillary tube with AB glue. In our experiments, the depth of cutting away is about 22 μm, and the length is 3mm. The uniform length of the Hi-Bi MNF we used here is ~ 1 cm and the diameter of the major axis is ~2.8 μm. The obtained Hi-Bi MNF was inserted in the designed capillary tube with a length of 5 cm. The MNF was encapsulated inside a silica capillary with an outer diameter of ~900 μm and two side-holes with a diameter of ~500 μm were made near the two ends of the capillary. Before the start of tapering, the cut SMF was spliced into a Sagnac loop interferometer, as shown in Fig. 4.3, and the evolution of loss and birefringence of the MNF was monitored continuously by observing the transmission spectrum of the interferometer. No variation in the transmission spectrum was observed before and after encapsulation.

4.3.1 Temperature stability in air

The transmission spectra of the Sagnac loop interferometer with the sealed Hi-Bi MNF is shown in Fig. 4.4 (the black line), which was preserved well while the MNF was inserted into the capillary and encapsulated. The transmission spectrum was monitored when temperature surrounding the Hi-Bi MNF was varied from 25 °C to 100 °C in steps of 25 ℃ by use of a digitally controlled oven after drilling two holes with a diameter of 400 μm at the two ends of the capillary with femtosecond laser, as shown in Fig. 4.4. The measured temperature sensitivity is only 7.72 pm/℃ at 1550 nm in air due to the low thermal-expansion coefficient of the silica fiber, which is more stable and repeatable, because the capillary tube can avoid the particles which moves faster resulting from the higher temperature in the air to adhere to the surface of the MNF. Due to the low sensitivity of the Hi-Bi MNF to temperature, this sensing system can be effectively applied to other measurements to avoid the cross-sensitivity.

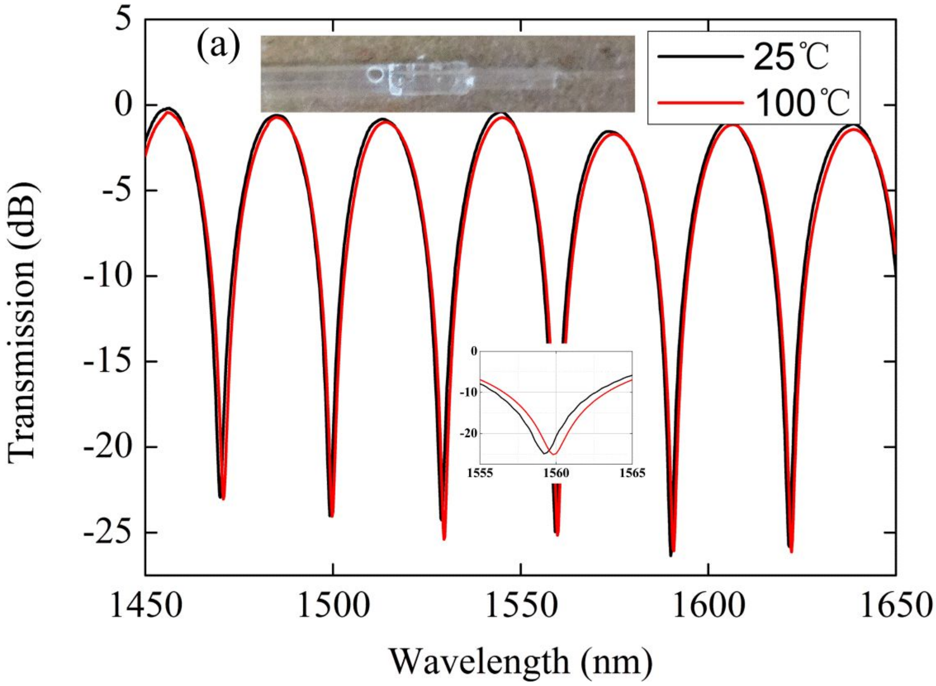

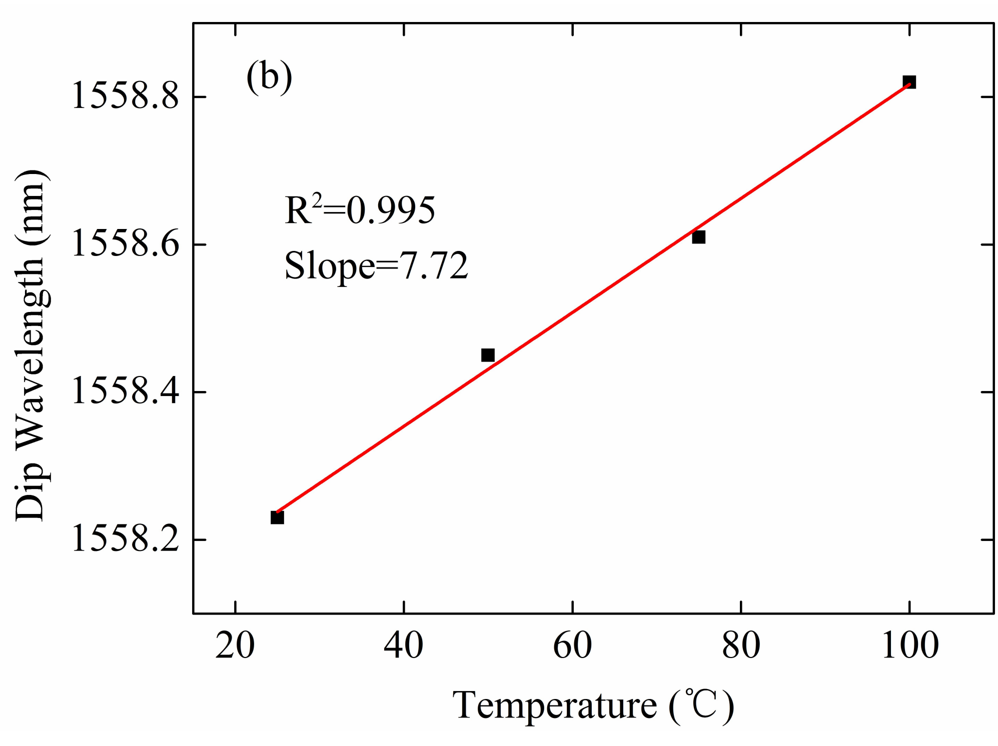

Fig. 4.4 (a) Transmission spectra evolution of Sagnac loop interferometer system with encapsulated Hi-Bi MNF from room temperature (25 ℃) to 100 ℃. (b) Dip wavelength at 1558.23 nm as a function of temperature.

4.3.2 Gas concentration measurement

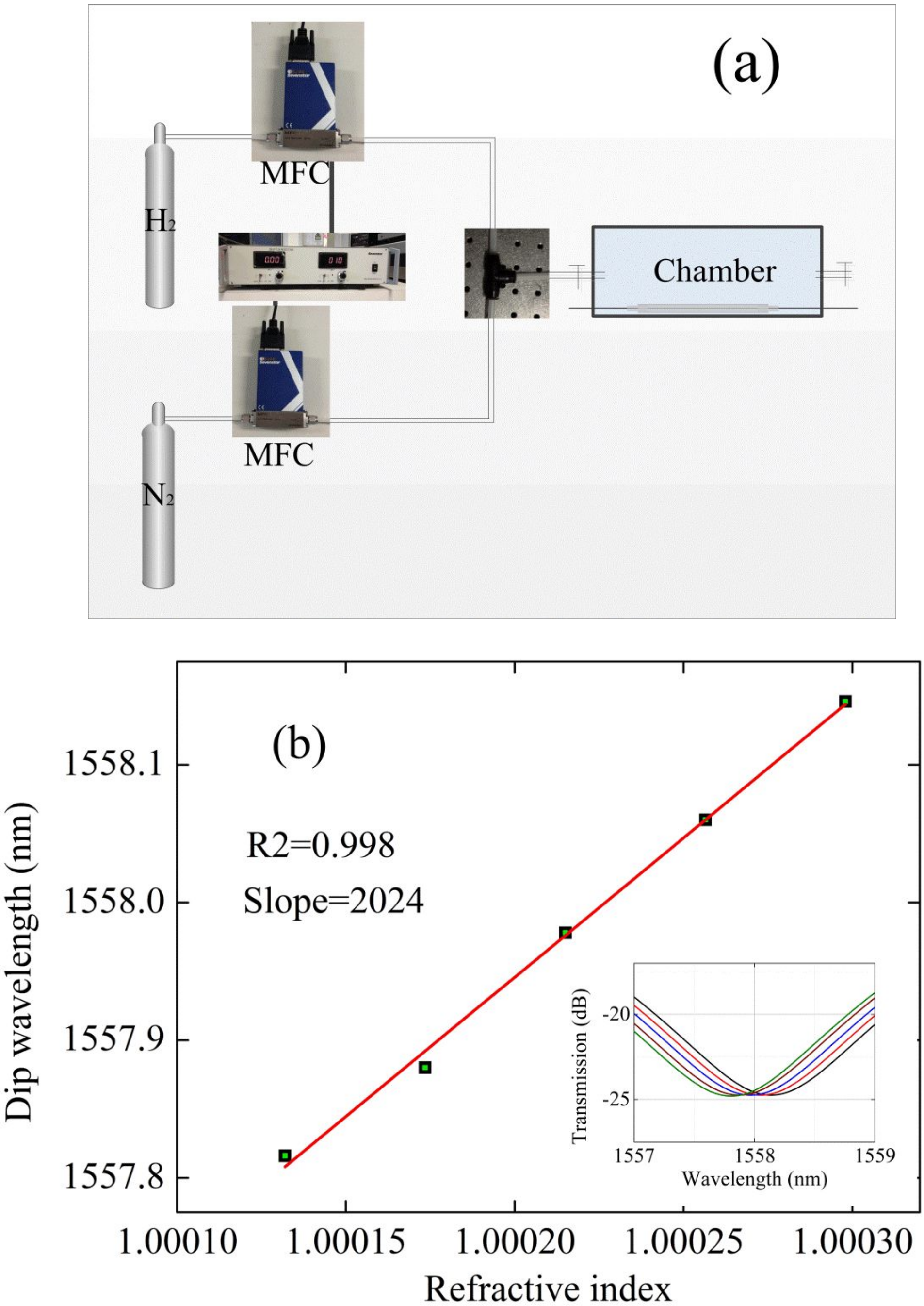

Fig. 4.5 (a) Experimental setup for measuring refractive index of gas mixture. MFC: mass flow controller. (b) Dip wavelength shift as a function of refractive index around 1 at wavelength 1558 nm. Inset: spectrum evolution.

The two holes at the end can ensure the pressure stable inside the capillary, this structure was used to measure the changes in the refractive index of gas mixture. The capillary with Hi-Bi MNF was placed into a gas chamber, as shown in Fig.4.5 (a), the inlet and outlet of the chamber were open to make the pressure in the chamber stable, the 100% standard hydrogen gas and nitrogen gas were mixed with different proportions by varied the flow of the two gas which was controlled by the digital mass flow controller, then the gas mixture was injected into the gas chamber. For the small gas chamber, the gas concentration of the small chamber and the capillary can reach that of the gas mixture in seconds. The refractive index of the mixture gas can be calculated by [15]

$$n_m = v_{H_2} n_{H_2} + v_{N_2} n_{N_2} \tag{4.1}$$

where n_m is the refractive index of the mixture and n_i and v_i are the refractive index and the fraction of component *i*, respectively.

The experimental process was conducted as follows: firstly, the hydrogen gas was switched off and the nitrogen gas with a flow rate of 150 sccm (standard cubic centimeter per minute) was continually injected into the chamber, and the spectrum was recorded when it became stable. The flow rate of hydrogen gas was then set to 50, 150 and 450 sccm, the evolution of spectra were recorded. Then the flow of nitrogen gas was set to 0 sccm and only the hydrogen gas was injected into the chamber, the spectrum was recorded when the chamber was fully filled with hydrogen. The five recorded spectra correspond, respectively, to (v_i , v_i) = (1,0), (3/4,1/4), (1/2, 1/2), (1/4, 3/4) and (0,1). Fig. 4 (b) shows the dip wavelength around 1558 nm as a function of the RI of the gas mixture, and the detailed spectra for the five gas mixtures are shown in the inset of Fig. 4 (b). The dip wavelength shifts to the longer wavelength with an increasing refractive index and the slope coefficient or sensitivity is 2024 nm/RIU.

4.3.3 Gas pressure measurement

As known, the refractive index of gas changes with gas pressure, and the refractive index sensor was also used to measure nitrogen gas pressure. For the purpose of applying different gas pressure into the glass tube, only one hole with a diameter of 200 μm was left at one end of the capillary, and a three port tube was used to let the gas inject into the caapillary, as shown in the inset in Fig. 4.6. The gas can be ramped up or down by the gas pump, the experiments were carried out at room temperature (~25℃). With the changing of the relative gas pressure surrounding the Hi-Bi MNF, the phase difference (φ) altered due to the refractive index variation, the peak of wavelength shifted, as shown in inset in Fig. 4.6.

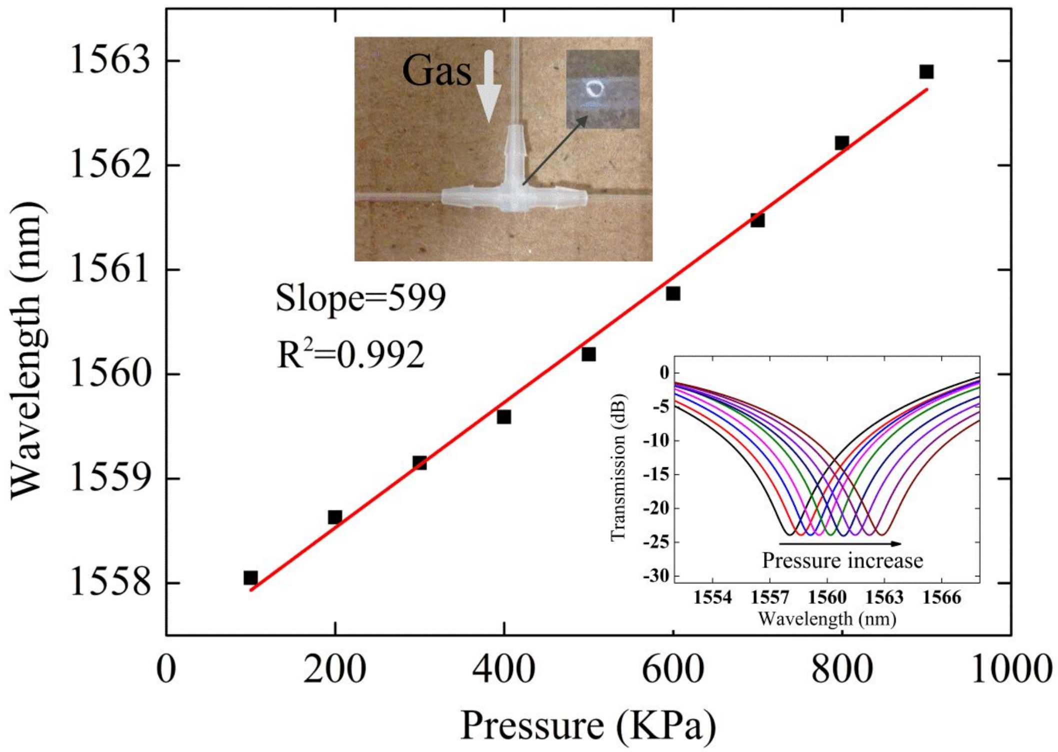

Fig. 4.6 Wavelength of the dip around 1558 nm (at room temperature) as a function of gas pressure when pressure is varied from 1 bar to 9 bar.

The gas used in this experiment is nitrogen whose refractive index is a function of temperature and pressure, and the refractive index at any two conditions of temperature and pressure can be expressed [16]

$$\frac{n_1-1}{n_2-1}=\frac{P_1T_2}{P_2T_1}\frac{Z_2}{Z_1}[1+\frac{n_1-1}{6}\left(1-\frac{P_2T_1}{P_1T_2}\right) \tag{4.2}$$

where Z is the compressibility of nitrogen

$$Z=1-\frac{P(317.6-T)\times10^{-5}}{101325} \tag{4.3}$$

This formula requires pressure P to be in pascals and the temperature T to be in degrees Kelvin. In our experiments, the temperature was not changed, thus the refractive index differed by a simple factor of pressure, and the pressure in the tested pressure tube was changed from 1 bar to 9 bar in steps of 1 bar, corresponding to the refractive index of air changing from 1.00029 to 1.00262. The test results are shown in Fig. 5.5, where the interference valley shifts linearly to gas pressure changes, and the sensitivity of the 599 pm/ bar at the dip of wavelength is around 1558 nm, which is much higher than that of other optical fiber devices[17, 18], and the corresponding to refractive index sensitivity of 2285 nm/RIU.

4.3.4 Refractive index measurement

The capillary with two holes open at the two ends was filled with water to explore its potential application for biosensors. One hole of the capillary was immersed into water, with the water filling the region between the two holes of the capillary in just a few seconds via the capillarity, as shown in the inset Fig. 4.7 (a).The refractive index of water was changed by varying its temperature. The thermo-optic coefficient of water refractive index is in the order of ~ -1×10^{-4}/℃, and the refractive index of water may be obtained by use of the look-up table in [19] once the temperature is known. The temperature sensitivity of the Sagnac loop interferometer with the MNF in air is only about 0.008 nm/℃ at 1550nm as measured above and is neglected in these experiments. Fig. 4.7 (b) shows the wavelength for the dip around 1550 nm versus the refractive index when the water temperature is varied from 25 to 50℃, corresponding to the refractive index change from 1.33335 to 1.3301, and the refractive index sensitivity obtained is ~21,231 nm/RIU.

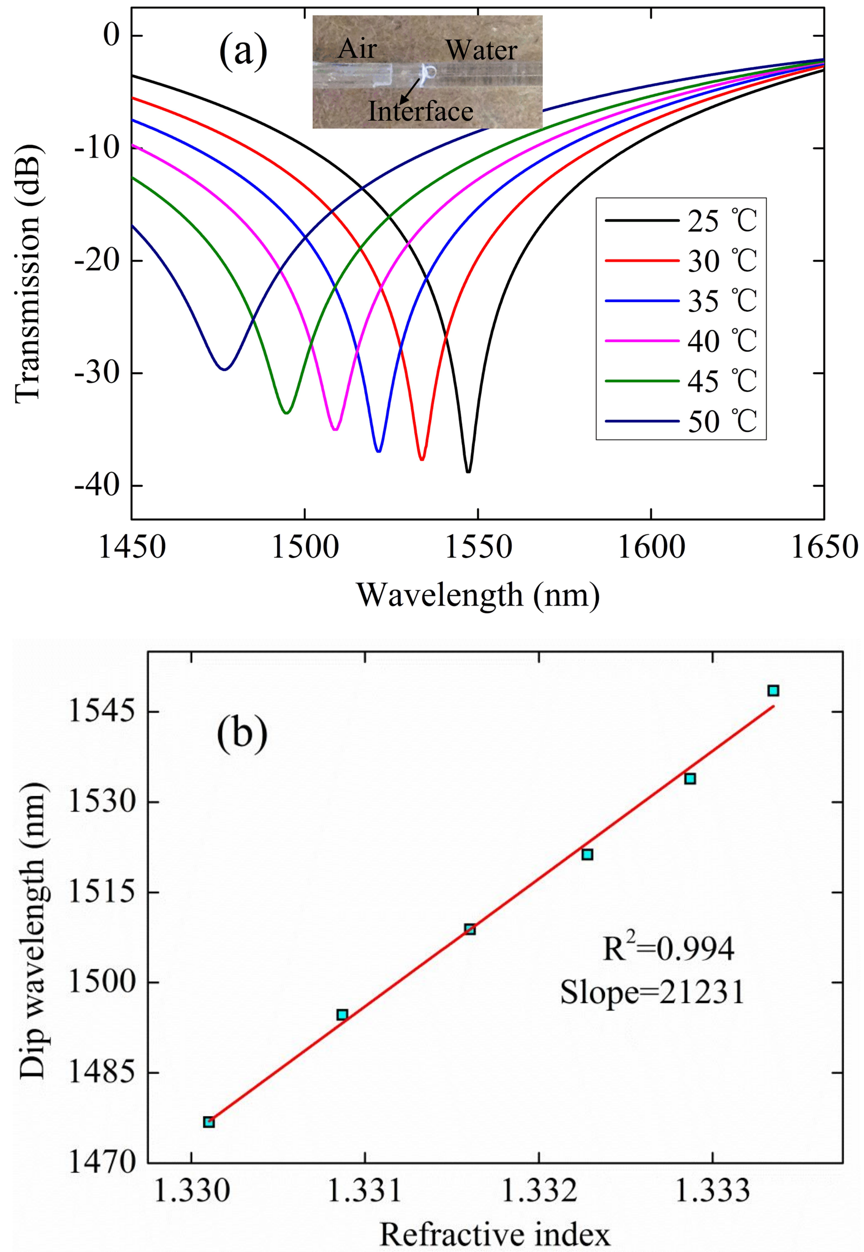

Fig. 4.7 (a) Measured transmission spectra when temperature is varied from 25 to 50 ℃, inset: the region around hole at the end of the capillarity. (b) Wavelength of the dip around 1548 nm as a function of refractive index.

4.3.5 Temperature sensor

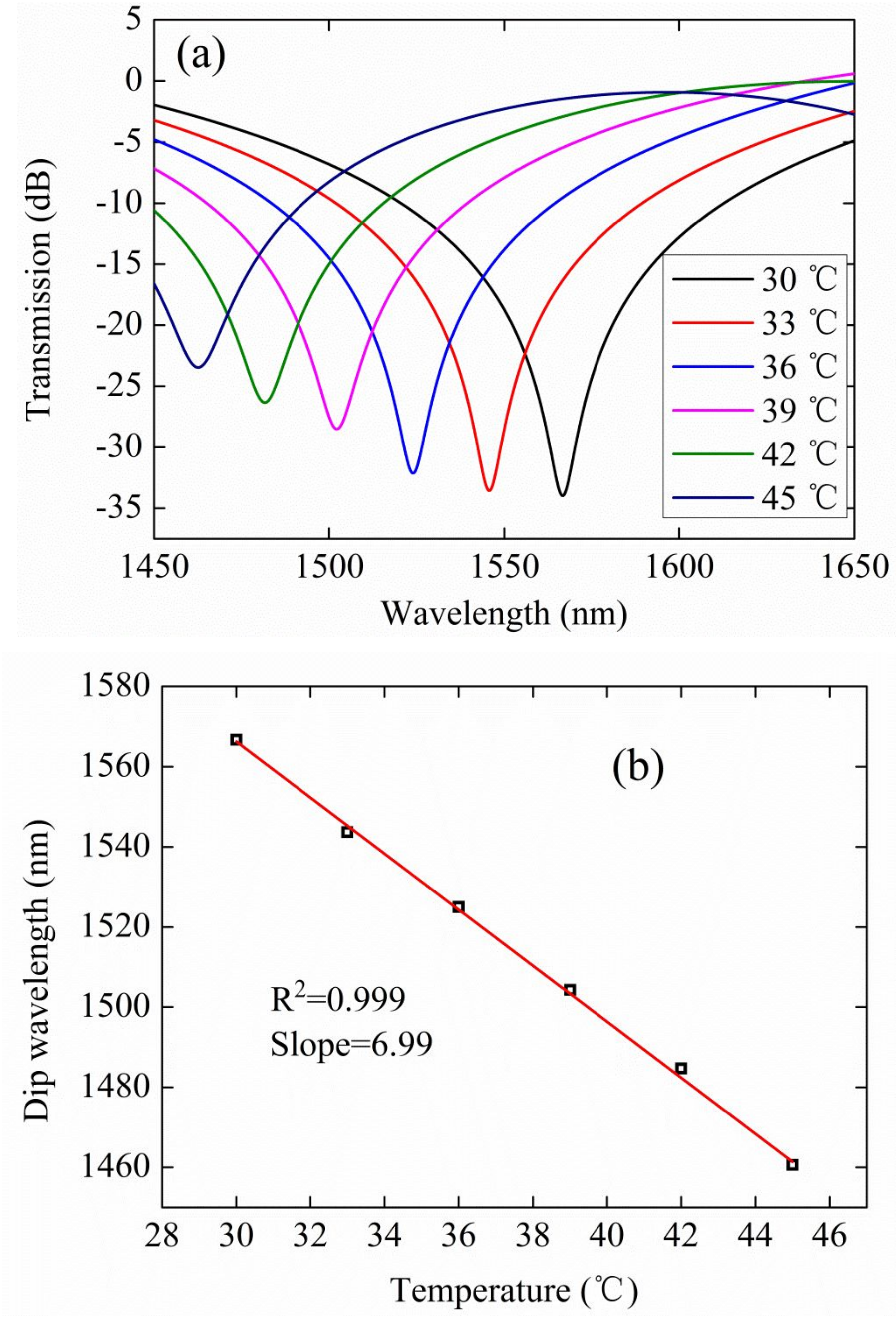

Fig. 4.8 (a) Measured transmission spectra when temperature is varied from 30 to 45 ℃. (b) Dip wavelength as a function of temperature.

The photonic microcell can be cleaned and re-used. By use of a piece of absorbent paper to cover one of the holes on the capillary wall, the majority of water within the microcell can be removed within seconds. The cell was then re-filled with 99.5% propyl alcohol, which was removed by placing the absorbent paper on the hole. This process was repeated a number times and the microcell left in air for a few minutes to dry out the alcohol. The transmission spectrum of the Sagnac loop interferometer was found returned to the initial spectrum shown in Fig. 4.4, indicating that no water was left within the cell. Then microcell was then filled with a refractive index oil with n=1.3 and a high thermo-optic coefficient of $-3.34\times10^{-4}/℃$. The transmission spectra are monitored when temperature surrounding the sealed Hi-Bi MNF was varied from 30 to 45°C, as shown in Fig. 4.8 (a). In the temperature range of 30°C–45°C, the refractive index value of refractive index oil was estimated to change from 1.29833–1.29332, where the Sagnac loop interferometer showed a high refractive index sensitivity, linear response, and good extinction ratio, as shown in Fig. 4.8 (b). With temperature augmentation, the refractive index around the Hi-Bi MNF decreases rapidly, leading to the transmission spectrum blue shift with a temperature sensitivity of -6.99 nm/°C, corresponding to the refractive index sensitivity of 20,928 nm/°C.

4.3.6 Results discussion

With a change of the refractive index surrounding the sensing element Hi-Bi MNF, the phase difference φ alters, the peak of the wavelength will shift, so the sensitivity S can be express as [20]

$$S = \frac{d\lambda}{dn} = \frac{\lambda\,\partial B/\partial n}{B - \lambda\,\partial B/\partial\lambda} = \frac{\lambda\,\partial B/\partial n}{G} \tag{4.4}$$

Eq. (4.4) shows that the sensitivity S is determined by the refractive index induced birefringence variation $\partial B/\partial n$ and the wavelength-dependent dispersion of birefringence $\partial B/\partial\lambda$, G is group birefringence. For the Hi-Bi elliptical MNF used in our experiments, the birefringence decreases with the external refractive index, as shown in Fig. 4.9 (a), that is $\partial B/\partial n<0$, and the birefringence does not change monotonically with the wavelength.

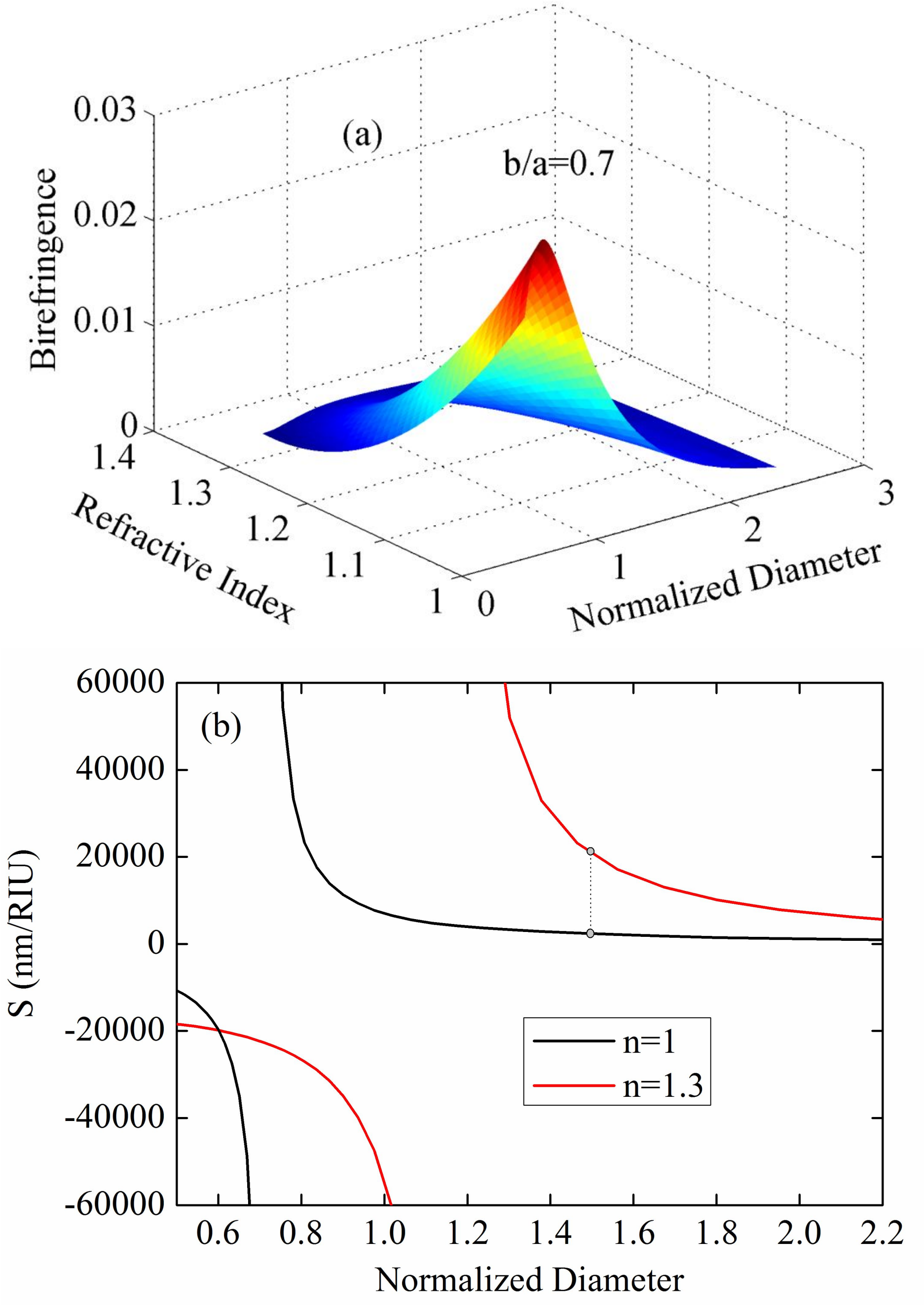

Fig. 4.9 (a) Simulated birefringence as a function of external refractive index and normalized diameter. (b) Simulated sensitivity as a function of normalized diameter

The numerical simulations are given to show the sensitivity for different dimension of the Hi-Bi MNFs when they are surrounded by gas (when the refractive index is around 1) and liquid (when the refractive index is around 1.3), as shown in Fig. 4.9 (b). The sensitivity is enhanced significantly when the group birefringence G approaches zero. Note that the sensitivity characteristics given in Eq. (4.4) is calculated for a specific wavelength. Considering a spectral width in an interferometric dip, the infinite sensitivity can't be achieved [18].

4.4 Summary

We have demonstrated a simple, effective method for fabricating in-line photonic microcells with a tapered micro/nano meter-sized core encapsulated within a capillary tube. This microcell structure proved to be robust, stable, not susceptible to contamination, and can be integrated into standard fiber optic systems, making MNFs easier for some practical applications.

With an encapsulated Hi-Bi MNF photonic microcell spliced into a Sagnac loop interferometer system, we demonstrated gas pressure and refractive index sensors with a pressure sensitivity of 599 pm/bar and an refractive index sensitivity of 2024 nm/RIU at RI~1. With the same photonic microcell, we also demonstrated liquid refractive index and temperature sensors and achieved an refractive index sensitivity of 21231 nm/RIU at RI~1.33 and temperature sensitivity of −6.99 nm/°C with the refractive index oil of 1.3 filling in the capillary.

References of Chapter 4

1. F. Xu, and G. Brambilla, "Preservation of micro-optical fibers by embedding," Jpn. J. Appl. Phys. Vol. 47, 6675–6677 (2008).
2. N. Lou, R. Jha, J. L. Domínguez-Juárez, V. Finazzi, J. Villatoro, G. Badenes,

and V. Pruneri, “Embedded optical micro/nano-fibers for stable devices,” Opt. Lett. Vol. 35, 571–573 (2010).

3. G. Vienne, Y. Li, and L. M. Tong, “Effect of Host Polymer on Microfiber Resonator,” IEEE Photon. Technol. Lett. Vol. 19, 1386–1388 (2007).
4. L. M. Xiao, M. D. W. Grogan, W. J. Wadsworth, R. England, T. A. Birks, “ Stable low-loss optical nanofibers embedded in hydrophobic aerogel,”Opt. Express, Vol. 19, 764-769 (2011).
5. V. Vali and R. W. Shorthill, “Fiber ring interferometer,” Appl. Opt., Vol. 15, 1099–1100 (1976).
6. B. Culshaw, “The optical fiber Sagnag interferometer: an overview of its principles and applications, ” Meas. Sci. Technol., Vol.17, pp. R1-R16 (2006).
7. E. De la Rosa, L. A. Zenteno, A. N. Starodumov, and D. Monzon, “All-fiber absolute temperature sensor using an unbalanced high-birefringence Sagnac loop,” *Opt. Lett.*, vol. 22, pp. 481–483 (1997).
8. Y. Yu, X. Li, X. Hong, Y. 4.Deng, K. Song, Y. Geng, H. Wei, and W. Tong, “Some features of the photonic crystal fiber temperature sensor with liquid ethanol filling,” Opt. Express, vol. 18, pp. 15383–15388 (2010).
9. M. Campbell, G. Zheng, A. S. Holmes-Smith, and P. A. A. Wallace, “Frequency-modulated continuous wave birefringent fiber-optic strain sensor based on a Sagnac ring configuration,” Meas. Sci. Technol., vol.10, pp. 218–224 (1999).
10. X. Y. Dong, H. Y. Tam, and P. Shum, “Temperature-insensitive strain sensor with polarization-maintaining photonic crystal fiber based Sagnac interferometer,” *Appl. Phys. Lett.*, vol. 90, no. 15, pp. 151113-1–151113-3 (2007).
11. J. Villatoro, V.P. Minkovich, D. Monzo´ n-Herna´ ndez, “Temperature-independent strain sensor made from tapered holey optical fiber,”

Opt. Lett., Vol. 31, pp. 305-307 (2006).

12. C. Shen, C. Zhong, J. Chu, X. Zou, Y. Jin, J. Wang, X. Dong, Y. Li, L. Wang, and C. Shen, “Temperature-insensitive strain sensor using a fiber loop mirror based on low-birefringence polarization-maintaining fibers ”, Opt. Commun. Vol. 287, pp. 31-34 (2013).
13. Chun-Liu Zhao, X. Yang, C. Lu, W. Jin, M.S. Demokan, Temperature-insensitive interferometer using a highly birefringent photonic crystal fiber loop mirror, IEEE Photon. Technol. Lett., 16(11): 2535-2537, 2004.
14. O. Frazão, B. V. Marques, P. Jorge, J. M. Baptista, and J. L. Santos, “High birefringence D-type fiber loop mirror used as refractometer,” *Sens. Actuators B, Chem.*, vol. 135, no. 1, pp. 108–111, 2008.
15. Sibel GEACAI, Irina NIŢĂ, Olga IULIAN, Elis GEACAI, "REFRACTIVE INDICES FOR BIODIESEL MIXTURES," U.P.B. Sci. Bull., Series B, Vol. 74, pp. 149-160, 2012.
16. E. R. Peck and B. N. Khanna, J. Opt. Soc. Am, vol. 56,1059, 1966.
17. D.-W. Duan, Y.-J. Rao, and T. Zhu, "High sensitivity gas refractometer based on all-fiber open-cavity Fabry–Perot interferometer formed by large lateral offset splicing," J. Opt. Soc. Am. B, vol. **29**, pp. 912-915, 2012.
18. Z. Liu, C. Wu, M.-L. V. Tse, C. Lu, and H.-Y. Tam, "Ultrahigh birefringence index-guiding photonic crystal fiber and its application for pressure and temperature discrimination," Opt. Lett. **38**, pp. 1385-1387, 2013.
19. P. Schiebener, J. Straub, J. M. H. Levelt Sengers, and J. S. Gallagher, “Refractive index of water and steam as function of wavelength, temperature and density,” J. Phys. Chem. Ref. Data **19**, pp. 677–717 (1990).
20. J. Li, L.-P. Sun, S. Gao, Z. Quan, Y.-L. Chang, Y. Ran, L. Jin, and B.-O. Guan, “Ultrasensitive refractive-index sensors based on rectangular silica MNFs,” Opt. Lett., vol. 36, pp. 3593-3595 (2011).

Chapter 5

Long period gratings in Hi-Bi MNFs

5.1 Introduction

The guiding properties of MNFs have been studied and the results show that the thin silica fibers or wires with diameters from a few hundred nanometers to a couple of micrometers typically guide a single mode (with two orthogonal polarization states) or a small number of modes for light wavelength (in air) from 600 nm to 1.5 μm [1], hence it would be possible to fabricate in-line devices by exploiting the coupling between the fiber modes. Long period gratings (LPGs) are probably one of the most important in-line fiber devices that have widespread applications in telecommunication and sensing, as it possesses a periodical RI modulation along the fiber length, which couples the light energy from the fundamental mode to the other co-directional mode and hence creating resonant dips in its transmission spectrum [2], in this chapter, the long period gratings in Hi-Bi MNFs were investigated.

5.2 Modes in Hi-Bi MNFs

When the circular guide is made elliptical, the modes that are degenerate in the circular guide become non-degenerate in the elliptical waveguide because the circular symmetry is broken. According to the appropriate solutions of the wave equation for the elliptical waveguide [3], all modes on an elliptical dielectric cylinder are hybrid, for which neither field is purely transverse and there is a component of both electric and magnetic fields in the direction of propagation. It is therefore necessary to use the second system, calling EH or HE and putting the dominant field first. For instance, as the fundamental HE_{11} in circular guide splits into the oHE_{11} and eHE_{11} [4]. The same applies to higher order modes. The pattern of the transverse electric fields and the power density distribution for the first few higher order modes are shown in Fig. 5.1.

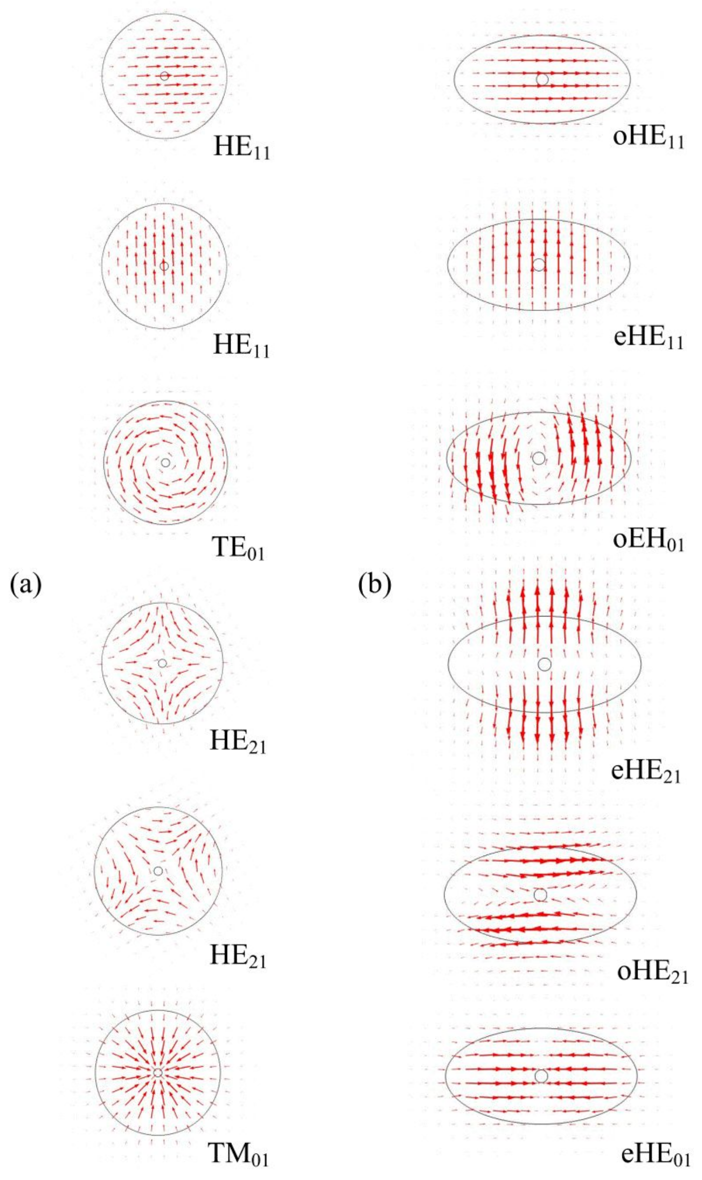

Fig. 5.1 Distribution of transverse electric field for modes in (a) MNF with circular cross-section, (b) Hi-Bi MNF with elliptical cross-section.

5.3 Long period gratings in Hi-Bi MNFs

The development of long period gratings (LPGs) has made a significant impact in optical fiber communication [5] and sensors [6]. Various fabrication techniques, such as the traditional UV writing technique [2, 5-9], a femtosecond laser writing technique [10-14], CO_2 laser irradiation [15-19], arc discharge [20-23], chemical etching [24-25], and periodic mechanical stress techniques [26-28] are used to fabricate LPGs in both the standard telecommunication fibers [6] and microstructured optical fibers [29-31]. There has been investigations of LPGs on smaller size optical fibers, including surface-corrugated [32] and CO_2 laser-induced [33] LPGs on fiber taper with diameter from 10-15 μm, and recently, LPGs have been fabricated in thinner fibers (or MNFs) with a diameter of about a few micrometers with femtosecond laser[34] and CO_2 laser irradiation [35].

The resonant wavelength in the LPG can be obtained through the following expression [35]:

$$\Lambda = \lambda / \left(n_{eff,0} - n_{eff,\nu}\right) \tag{5.1}$$

where λ is the resonant wavelength, Λ is the grating pitch, and $n_{eff,0}$ and $n_{eff,\nu}$ are, respectively, the effective refractive indices of the fundamental and the υ-order mode. In the case of a Hi-Bi MNF, the resonant wavelengths for which coupling condition (Eq.(5.1)) is satisfied are different depending on the two principal input polarizations (two orthogonal polarizations aligned along the principal axes of the Hi-Bi MNF), the birefringence cause each input polarization corresponding to each axis (slow or fast axis) have different effective refractive indices of core and high order modes. This can result in a splitting of wavelength-dependent loss band and cause the codirectional mode coupling condition to be different at the two principal input polarizations.

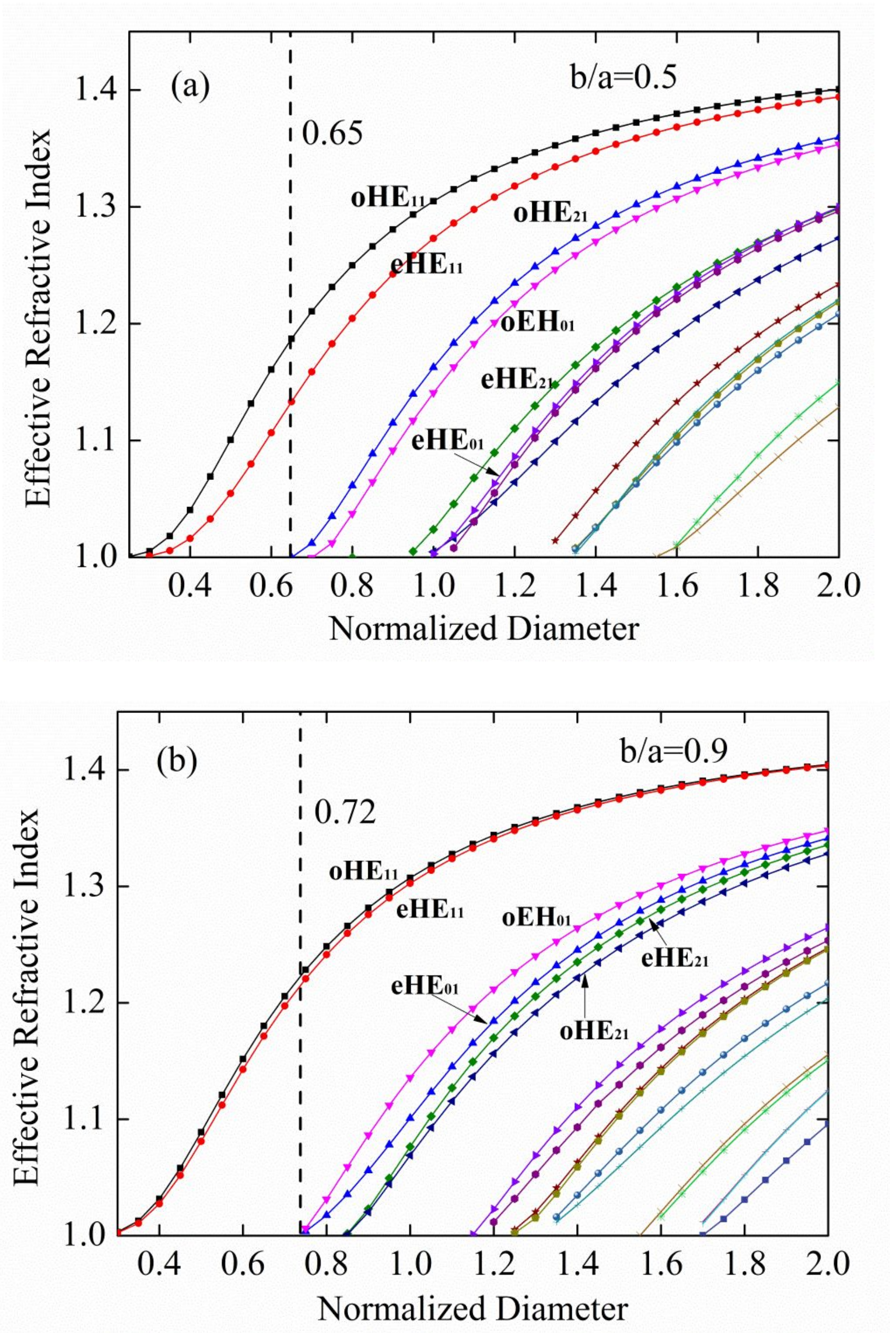

Fig. 5.2 Effective indexes of lower-order modes as functions of normalized fiber diameter ($\sqrt{2a*2b}/\lambda$) for *b/a*=0.5 (a) and *b/a*=0.9 (b)

Fig. 5.2 (a) shows the effective index n_{eff} of the modes in air clad silica Hi-Bi MNFs as a function of a normalized fiber diameter $\sqrt{2a*2b}/\lambda$ for MNFs with *b/a*=0.5 and *b/a*=0.9, respectively. It is clear that, when the normalized diameter is larger than a certain value as denoted as the vertical dotted line in Fig. 5.2 (a) and (b), the Hi-Bi MNF is a multi-mode waveguide, which is the diameter of the MNFs used for fabricating the LPG, the Hi-Bi MNF can support a few modes. Hence, by introducing a LPG satisfying the phase matching condition given in Eq. (5.1), resonant mode coupling devices may be implemented.

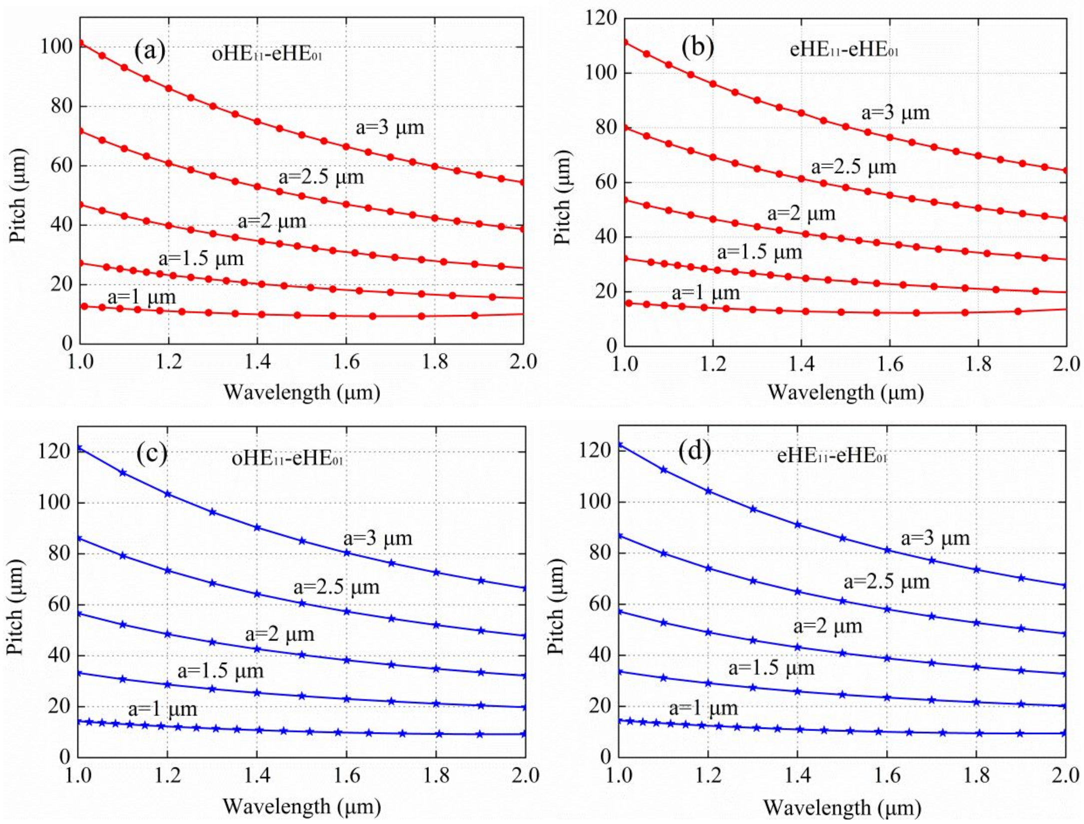

Fig. 5.3 Phase matching curves for MNFs with different size. (a) and (b) Coupling between oHE_{11}, eHE_{11} and eHE_{01} for b/a=0.5; (a) and (b) Coupling between oHE_{11}, eHE_{11} and eHE_{01} for b/a=0.9.

As can be seen from Fig. 5.2, the refractive index difference between fundamental and higher-order modes in a Hi-Bi MNF is much larger than that in conventional SMFs. According to Eq. (5.1), this large index difference will require a much smaller grating pitch to achieve phase matching. Fig. 5.2 show the phase matching (Λ-λ) curves of Hi-Bi MNFs with different diameters. The phase matching conditions between the two polarization states of fundamental mode and the eHE_{01} mode for the Hi-Bi MNF with a b/a=0.5 and b/a=0.9 are shown in Fig. 5.3.

5.4 Fabrication of LPGs in Hi-Bi MNFs

LPGs have been fabricated in MNFs by periodically inducing micro-tapers along the MNF by the use of a focused pulsed CO_2-laser in combination with a small applied longitudinal tensile strain [35], and by periodically modifying the surface along one side of the fiber with a femtosecond laser [34]. These two methods are also used to realize mode couplings in wavelength-scale Hi-Bi MNFs.

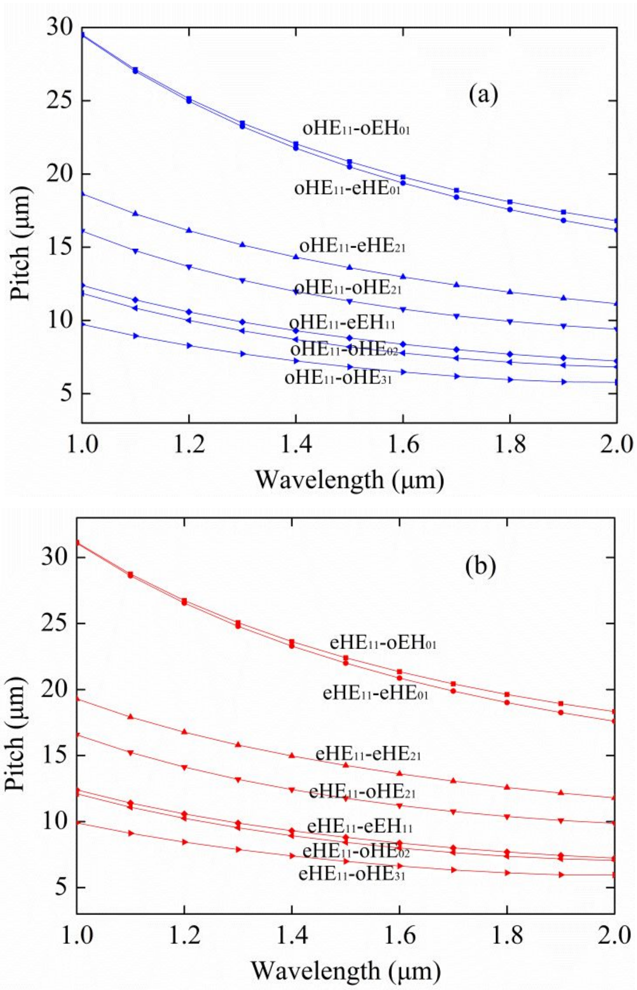

Fig. 5.4 Phase matching curves for a Hi-Bi MNF with a major-diameter of 2.8 μm and ellipticity of 0.7. (a) Coupling between oHE_{11} and high-order modes. (b) Coupling between eHE_{11} and high order modes.

The Hi-Bi MNFs used in this investigation have a uniform waist of ~1.7 cm in length, a major-diameter of ~2.8 μm and an ellipticity of ~0.7. In such a small-size MNF, the refractive index differences between fundamental and higher-order modes are much larger than in a standard-sized optical fiber, and the gratings pitch required to satisfy the phase matching condition are hence much shorter. Fig.5.4 shows the phase matching (Λ-λ) curves of the Hi-Bi MNF for coupling from the fundamental to the first few high-order modes. The curves are different for the orthogonal polarization eigen states.

For the CO_2 laser irradiation method [35], the perturbation was induced by the periodical taper-region. The high-frequency CO_2 laser pulses hit repeatedly on the MNF and induced a local high temperature to soften the silica of the fiber. By applying a small weight, a small constant longitudinal tensile strain is induced and the soften region, i.e., the CO_2 laser hit region, of the MNF will be drawn slightly, which creates a micro-taper, shown in Fig. 5.5.

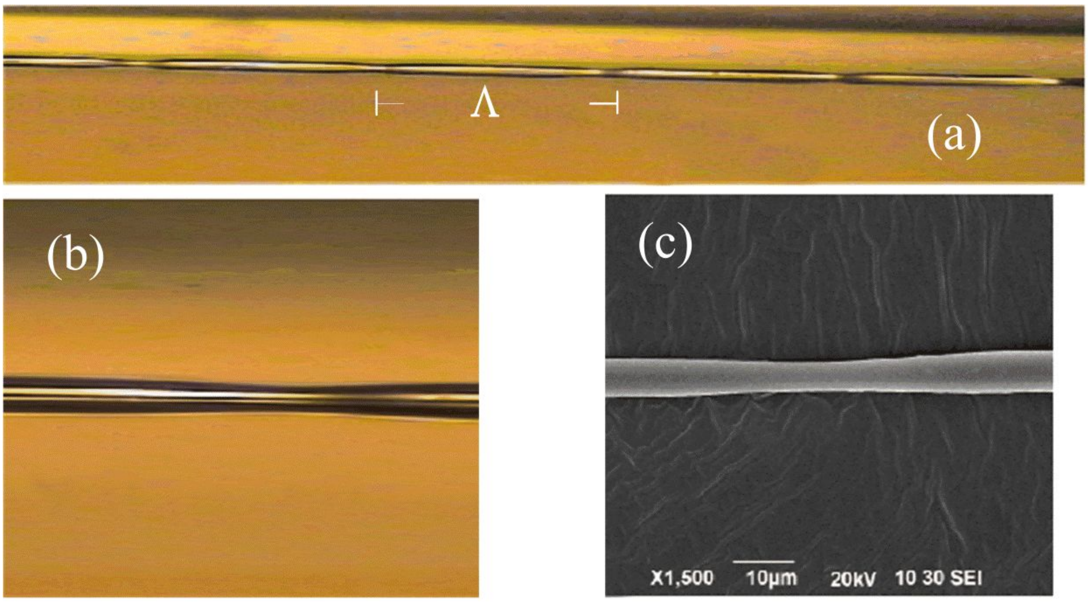

Fig. 5.5 (a) Microscope image showing the periodic micro-tapers along the fiber. (b) Microscope and (c) SEM images showing the details of micro-taper[35].

The experimental setup is shown in Fig. 5.6, and indicates a high-frequency pulsed laser that incorporated a computer-controlled beam scanner. A polarizer is used to launch linearly polarized light into the fibers. The two SMF pigtails of the Hi-Bi MNF are, respectively, connected to a Light-Emitting Diode (LED) and an optical spectrum analyzer (OSA). The CO_2 laser is adjusted to the following parameters: pulses width 2.0 µs, repetition rate 8 kHz, and average power ~0.02W. This power level is significantly smaller than the one used for LPG fabrication in normal-sized optical fibers [36, 37]. The CO_2 beam is focused to a spot with ~40µm in diameter and has a ~50µm depth of focus. The size of the focal spot is considerably larger than the diameter of the MNF. The laser beam advanced along the fiber in steps with the distance of each step equal to half of the grating period. At each step, the laser beam scanned across the fiber transversely. A scanning cycle was completed when the desired number of periods was reached. This procedure is repeated for N times in order to fabricate a LPG with N-1 periods. The process of making N successive transverse scans is called one scanning cycle. By controlling the number of scanning cycles, the depth of the attenuation dip in the transmission may be controlled. The writing process was computer-controlled and fully automatic via a computer controlled two-dimensional optical scanner, transversely and longitudinally as instructed by a preprogrammed routing.

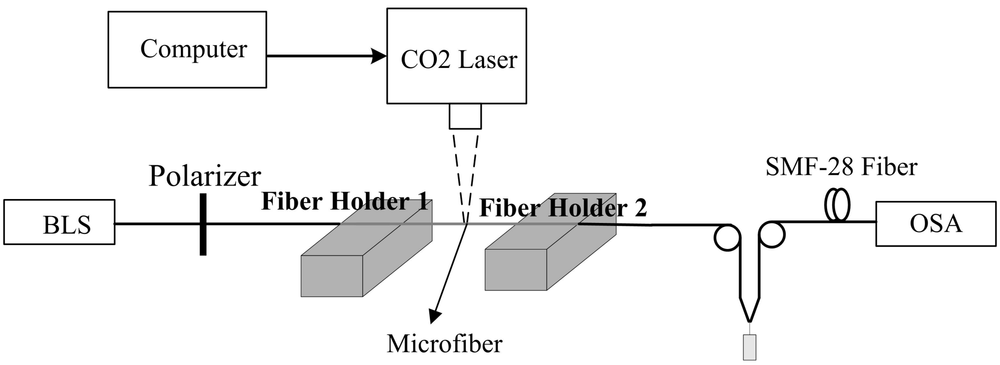

Fig. 5.6 Experimental setup of the CO_2 laser system for fabricating LPGs in Hi-Bi MNFs.

It should be mentioned that the LPGs made with the CO_2 laser are higher order gratings and have grating pitches several times larger than the first order gratings. It is difficult to write first order LPGs with such a CO_2 laser because that the spot size of the focused CO_2 laser is over 30 μm, which is considerably larger than the grating pitches required to produce first order gratings.

Fig. 5.7 shows the measured transmitted spectrum of a LPG made in a Hi-Bi MNF with a diameter of ~2.8 μm. The grating has a pitch of ~150 μm and 16 periods with the resonance wavelengths for the two polarization modes of 1445.5 and 1575.6 nm, respectively, and the attenuation dip of 12.5 dB and 20 dB, respectively. Because the spot size of a focused CO_2 laser is larger than 30 μm, hence it is difficult to fabricate an LPG with a pitch smaller than this value, and small pitch in thin fiber will also induce the modal beat length, in this experiment, the pitch of this Hi-Bi MNF is designed to be larger than the numerical pitch to realize a higher order coupling. The obtained grating was encapsulated in the designed capillary tube, and kept the transmission property well for over one month.

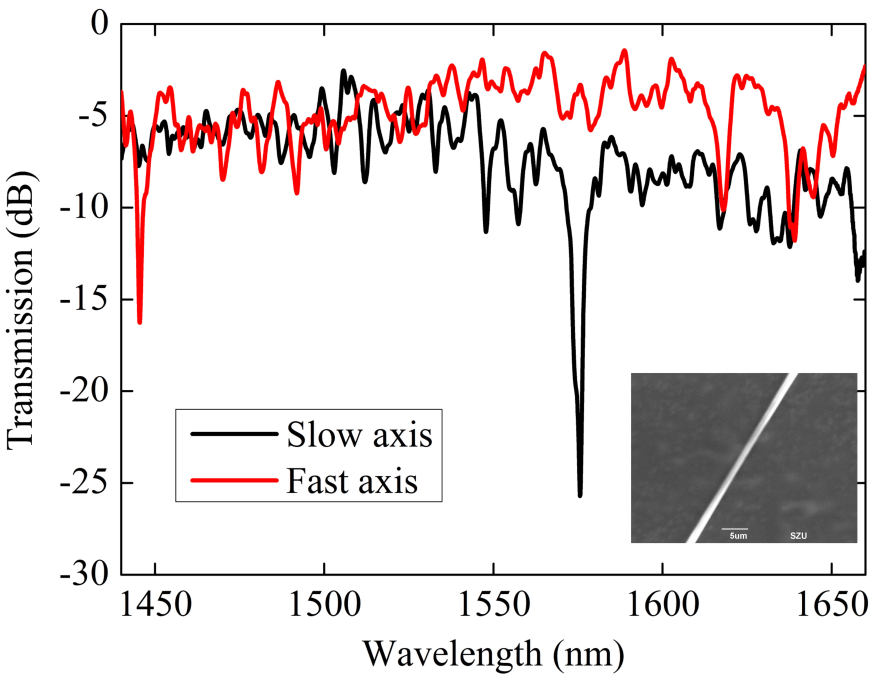

Fig. 5.7 Transmission spectra of LPG written in a Hi-Bi MNF with CO_2 laser irradiation.

The LPG can also be written on the encapsulated Hi-Bi MNFs with a femtosecond laser by periodically modifying the surface along one side of the fiber [34] to achieve the mode coupling, as shown in Fig. 5.8. One pigtail is connected to a broadband source (BLS) covering a wavelength from 1450 nm to 1650 nm, while the other pigtail is connected to an optical spectrum analyzer to record the transmission spectrum during the LPG fabrication process. During LPG fabrication, a polarizer was used to launch a linearly polarized light beam to the fiber to optimize the transmission dips.

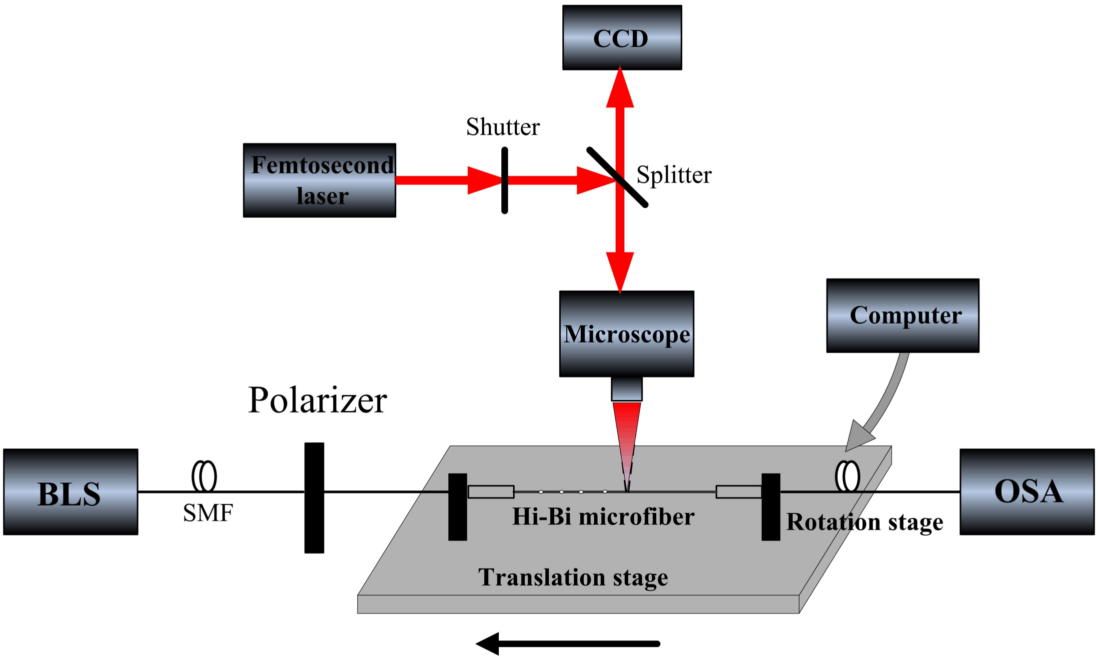

Fig. 5.8 Schematic of the femtosecond laser system for fabricating LPGs in MNFs. Inset: (a) Microscope image showing the periodic notches along the fiber. (b) SEM image showing two adjacent notches. (c) SEM image showing the details of a notch induced by femtosecond laser pulses .

With the assistance of an optical microscope, the laser focal position can be monitored and displayed on an LCD monitor, through which the location of the focal point on the MNF can be accurately adjusted via the computer-controlled translation stage. The LPG is fabricated by a point-by-point (PBP) process. Compared with the mask approach [5], the PBP process is more flexible, although it requires accurate control of the beam position with respect to the fiber.

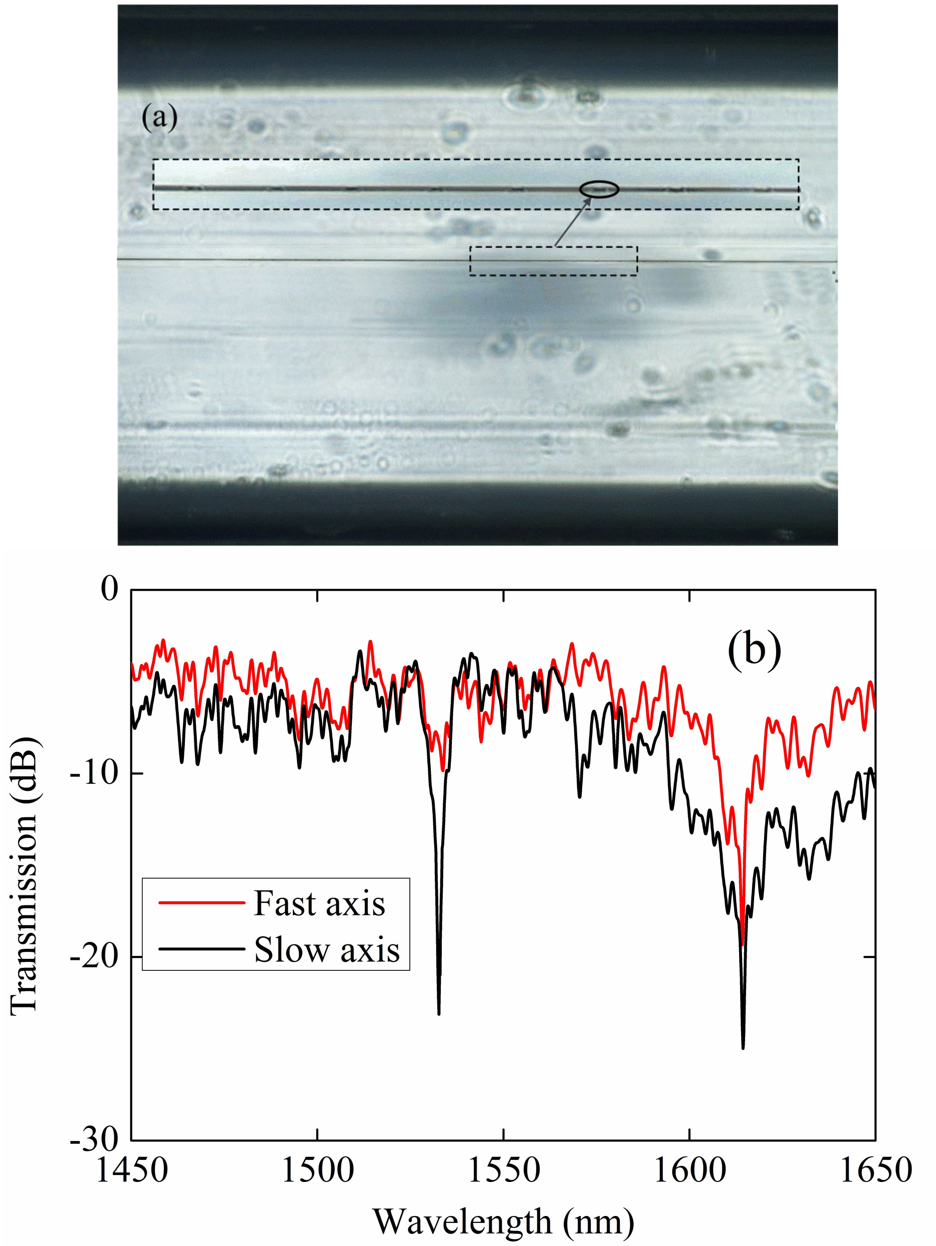

Fig. 5.9 (a) Microscope image showing the periodic notches along the encapsulated MNF. (b) Transmission spectra of LPG written in a Hi-Bi MNF.

The laser pulses with an irradiation intensity of 0.1 J/cm^2 are focused on the center of the upper surface of Hi-Bi MNF with an exposure time of 1s, and the focal spot is then moved to the next point along the fiber by use of the three-axis translation stage.The periods of the LPGs in such Hi-Bi MNF are on the order a few tens of micrometers. A polarizer is used to launch polarized light into the SM pigtail of the Hi-Bi MNF. Fig. 5.9 shows the transmission spectrum of an LPG fabricated on the encapsulated Hi-Bi MNFs with the diameter of the major axis of ~2.8 μm and a pitch of 20 μm. After inscribing 15 notches, the maximum coupling is realized with the resonance wavelengths for the two polarization modes of 1532.7 and 1614.2 nm, respectively, and the corresponding grating strengths of 19.2 and 15.2 dB, respectively.

5.5 Refractive index sensitivity measurement

A potential application of LPGs made in MNFs is for high sensitivity refractive index sensing. In [35], a LPG was fabricated on MNFs with a diameter of 6.3 μm and a refractive index sensitivity of ~1900 nm/RIU around RI=1.32 was achieved. For the LPG with its transmission spectrum shown in Fig. 5.7 and Fig. 5.9, however the resonance dips disappeared when it was immersed in water, it is difficult to achieve the mode coupling conditions when the refractive index of the cladding surrounded the MNFs changed a lot.

We then fabricated another LPG with a grating pitch of 200 μm by use of the femtosecond laser, the transmission spectra in air and in water are shown in Fig. 5.10. The existence of resonant couplings when the LPG is surrounded by a water-like solution is important for a range of chemical and biological applications. We then performed a refractive index measurement by varying the refractive index of the water via temperature. The temperature coefficient of refractive index of water is in the order of ~ -1×10^{-4} /℃, and the refractive index of water may be obtained by use of the look-up table in [38] once the temperature is known. Figure 5.11(a) shows the changes of transmission spectrum when the water temperature was varied from 22 to 30℃. The resonance wavelength for the dip around 1569 nm versus the refractive index is shown in Fig. 5.11 (b) and a refractive index sensitivity of ~4623 nm/RIU, over two times bigger than the value reported in [35], was achieved. The temperature sensitivity of the LPG in air was measured to be ~8 pm/℃, significantly smaller than the contribution of temperature-induced change of water refractive index .

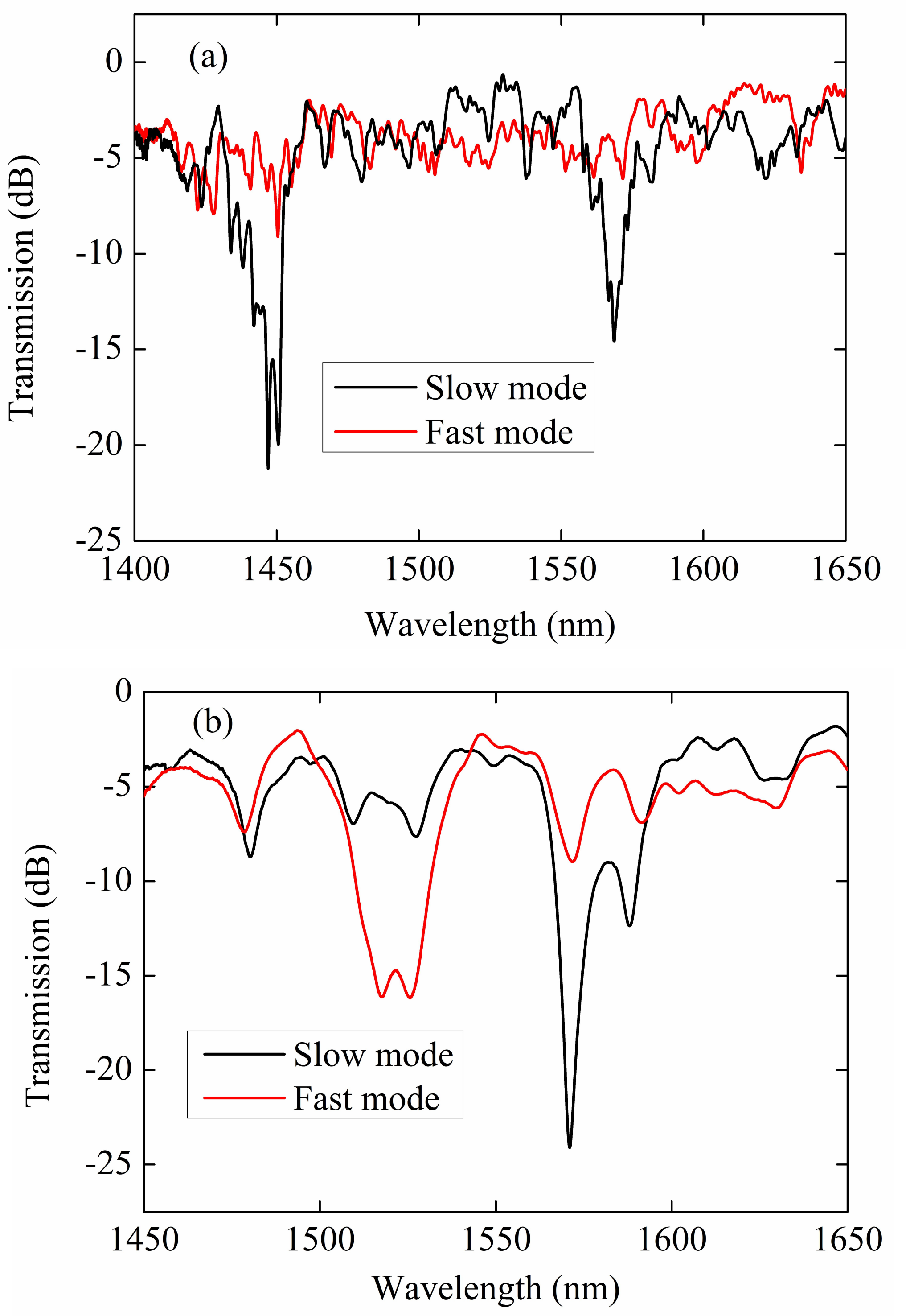

Fig. 5.10 Transmission spectra of a LPG for orthogonal input polarizations. The grating pitch is 200 μm. (a) in air and (b) in water.

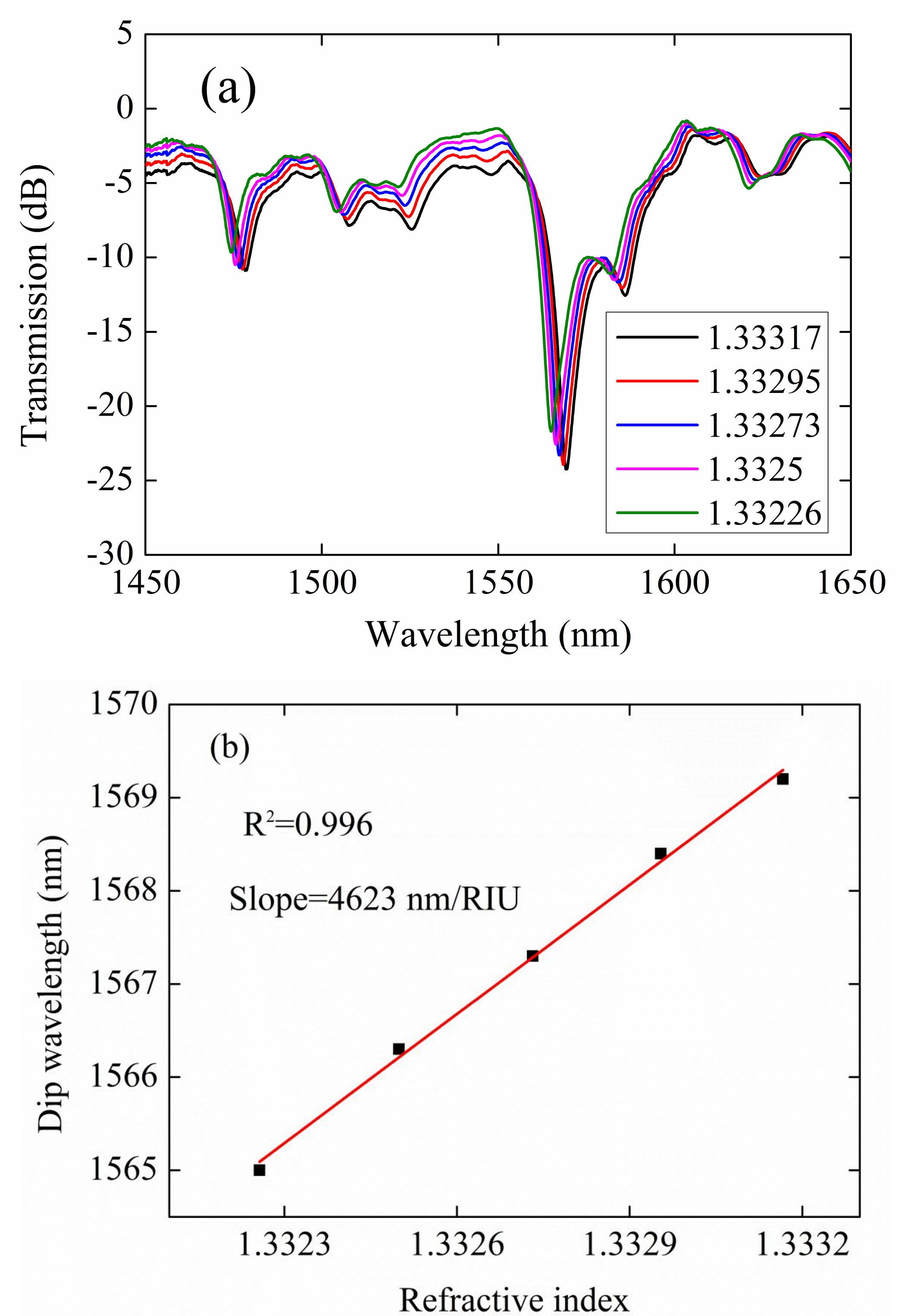

Fig. 5.11 (a) Measured transmission spectra when refractive index varied from 1.3317 to 1.33226. (b) Wavelength of the dip around 1548 nm as a function of refractive index.

5.6 Summary

Coupling between guided modes in Hi-Bi MNFs are realized by fabricating LPGs along the Hi-Bi MNFs. The LPGs are fabricated by periodically inducing micro-tapers along the MNFs by use of focused pulsed CO_2 laser in combination with small applied longitudinal tensile strain. We show that a 16-period LPG with the resonance wavelengths for the fast and slow modes of 1445.5 and 1575.6 nm, respectively, and the attenuation dip of 12.5 and 20 dB, respectively. The obtained grating was also encapsulated into the designed capillary tube, and kept the transmission property well for one month and more. The LPGs are fabricated by periodically modifying the surface along one side of the fiber with a femtosecond laser. The periods of the LPGs in such Hi-Bi MNFs are on the order a few tens of micrometers,a LPG made on the encapsulated Hi-Bi MNFs with the diameter of the major axis of ~2.8 μm and a pitch of 20 μm. The polarization selected resonant dip of 19.2 dB and 15.2 dB was achieved with 15 periods corresponding to the resonant wavelength of 1532.7 and 1614.2 nm, respectively. Such an LPG is predicted with small temperature sensitivity and is truly a compact device with a grating length on an order of magnitude of micrometers. High order couplings were achieved by using these two methods, and a high order LPG made in a MNF with a major axis diameter of ~2.8 μm diameter and ~0.7 ellipticity with femtosecond laser method demonstrated a RI sensitivity of ~4623 nm/RIU in water. These LPGs would find applications in MNF wavelength filters, gain equalizers for MNF amplifiers, and wavelength-encoded evanescent-wave biosensors.

References of Chapter 5

1. L. Tong, J. Lou and E. Mazur, "Single-mode guiding properties of subwavelength-diameter silica and silicon wire waveguides," Opt. Express 12, 1025-1035 (2004).
2. A. M. Vengsarkar, P. J. Lemaire, J. B. Judkins, et al, “Long-period fiber gratings as band rejection filters,” J. Lightwave Technol., Vol. 14, pp. 58–65 (1996).
3. Yeh, C., "Elliptical Dielectric Waveguides," J. Appl. Phys., Vol. 33, 3235-3243 (1962).
4. Richard B. Dyott, “Elliptical fiber waveguides,” Artech House Publisher, Boston, London (1995).
5. A. M. Vengsarkar, J. R. Pedrazzani, J. B. Judkins, P. J. Lemaire, N. S. Bergano, and C. R. Davidson, “Long period fiber-grating-based gain equalizers,” Opt. Lett. , Vol. **21**, pp. 336–338 (1996).
6. V. Bhatia, and A. M. Vengsarkar, “Optical fiber long-period grating sensors,” Opt. Lett., Vol. **21**, pp. 692–694 (1996).
7. B. J. Eggleton, P. S. Westbrook, R. S. Windeler, et al, “Grating resonances in air-silica microstructured optical fibers,” Opt. Lett., Vol. **24**, pp. 1460-1462 (1999).
8. B. J. Eggleton, P. S. Westbrook, C. A. White, et al, “Cladding-Mode-Resonances in Air-Silica Microstructure Optical Fibers,” J. Lightwave Technol., Vol. **18**, pp. 1084-1100 (2000).
9. V. Bhatia, “Applications of long-period gratings to single and multiparameter sensing,” Opt. Express., Vol. **4**, pp. 457-466 (1999).
10. Y. Kondo, K. Nouchi, T. Mitsuyu, et al, “Fabrication of long-period fiber gratings by focused irradiation of infrared femtosecond laser pulses,” Opt. Lett., Vol. 24, 646-648 (1990).

11. E. Fertein, C. Przygodzki, H. Delbarre, “Refractive-index changes of standard telecommunication fiber through exposure to femtosecond laser pulses at 810 cm,” Appl. Opt., Vol. 40, 3506-3508 (2001).
12. A. I. Kalachev, D. N. Nikogosyan, G. Brambilla, “Long-period fiber grating fabrication by high-intensity femtosecond pulses at 211 nm,” J. Lightwave. Technol., Vol. 23, 2568-2578 (2005).
13. T. Allsop, M. Dubov, A. Martinez, et al, “Bending characteristics of fiber long-period gratings with cladding index modified by femtosecond laser,” J. Lightwave. Technol., Vol. 24, 3147-3154 (2006).
14. C. R. Liao, Y. Wang, D. N. Wang, et al, “Femtosecond laser inscribed longperiod gratings in all-solid photonic bandgap fibers,” IEEE Photon. Technol. Lett., Vol. 22, 425-427 (2010).
15. D. D. Davis, T. K. Gaylord, E. N. Glytsis, et al, “Long-period fibre grating fabrication with focused CO_2 laser pulses,” Electron. Lett., Vol. 34, 302-303 (1998).
16. G. Kakarantzas, T. E. Dimmick, T. A. Birks, et al, “Miniature all-fiber devices based on CO_2 laser microstructuring of tapered fibers,” Opt. Lett., Vol. 26, 1137-1139 (2001).
17. Y. J. Rao, Y. P. Wang, Z. L. Ran, et al, “Novel fiber-optic sensors based on long-period fiber gratings written by nigh-frequency CO_2 laser pulses,” J. Lightwave. Technol., Vol. 21, 1320-1327 (2003).
18. Y. P. Wang, L. M. Xiao, D. N. Wang, et al, “Highly sensitive long-period fiber-grating strain sensor with low temperature sensitivity,” Opt. Lett., Vol. 31, 3414-3416 (2006).
19. Y. Wang, W. Jin, J. Ju, et al, “Long period gratings in air-core photonic bandgap fibers,” Opt. Express, Vol. 16, 2784-2790 (2008).

20. G. Rego, O. Okhotnikov, E. Dianov, et al, “High-temperature stability of long-period fiber gratings produced using an electric arc,” J. Lightwave. Technol., Vol. 19, 1574-1579 (2001)
21. H. Dobb, K. Kalli, D.J. Webb, “Temperature-insensitive long period grating sensors in photonic crystal fibre,” Electron. Lett., Vol. 40, 657-658 (2004).
22. G. Humbert, A. Malki, S. Février, et al, “Characterizations at high temperatures of long-period gratings written in germanium-free air silica microstructure fiber,” Opt. Lett., Vol. 29, 38-40 (2004).
23. G, Rego, R. Falate, J. L Santos, “Arc-induced long-period gratings in aluminosilicate glass fibers,” Opt. Lett., Vol. 30, 2065-2067 (2005).
24. C. Y. Lin, L. A. Wang, G. W. Chern, “Corrugated long-period fiber gratings as strain, torsion, and bending sensors,” J. Lightwave. Technol., Vol. 19, 1159-1168 (2001).
25. Y. Jiang, Q. Li, C. H. Lin, et al, “A novel strain-induced thermally tuned long-period fiber grating fabricated on a periodic corrugated silicon fixture,” IEEE Photon. Technol. Lett., Vol. 14, 941-943 (2002).
26. I. K. Hwang, S. H. Yun, B. Y. Kim, “Long-period fiber gratings based on periodic microbends,” Opt. Lett., Vol. 24, 1263-1265 (1999).
27. S. Savin, M. J. F. Digonnet, G. S. Kino, et al, “Tunable mechanically induced long-period fiber gratings,” Opt. Lett., Vol. 25, 710-712 (2000).
28. P. Steinvurzel, E. D. Moore1, E. C. Mägi, et al, “Long period grating resonances in photonic bandgap fiber,” Opt. Express., Vol. 14, 3007-3014 (2006).
29. Y.-P. Wang, L. Xiao, D. N. Wang, and W. Jin, “Highly sensitive long-period fiber-grating strain sensor with low temperature sensitivity,” Opt. Lett., Vol. 31, 3414–3416 (2006).

30. P. Steinvurzel, E. D. Moore, E. C. Mägi, B. T. Kuhlmey, and B. J. Eggleton, "Long period grating resonances in photonic bandgap fiber," Opt. Express, Vol. 14, 3007–3014 (2006)

31. Y. Wang, W. Jin, J. Ju, H. Xuan, H. L. Ho, L. Xiao, and D. Wang, "Long period gratings in air-core photonic bandgap fibers," Opt. Express, Vol. 16, 2784–2790 (2008).

32. W. Ding, S. R. Andrews, and S. A. Maier, "Modal coupling in surface-corrugated long-period-grating fibertapers," Opt. Lett., Vol. 33, 717–719 (2008).

33. G. Kakarantzas, T. E. Dimmick, T. A. Birks, R. Le Roux, and P. S. J. Russell, "Miniature all-fiber devices basedon CO(2) laser microstructuring of tapered fibers," Opt. Lett., Vol. 26, 1137–1139 (2001).

34. H. F. Xuan, W. Jin, and S. J. Liu, "Long-period gratings in wavelength-scale MNFs," Opt. Lett., Vol. 35, pp. 85–87 (2010).

35. H. F. Xuan, W. Jin, and M. Zhang, "CO_2 laser induced long period gratings in optical MNFs," Opt. Express , Vol. 17, pp. 21882–21890 (2009).

36. Y. Wang, W. Jin, J. Ju, H. Xuan, H. L. Ho, L. Xiao, and D. Wang, "Long period gratings in air-core photonicbandgap fibers," Opt. Express, Vol. 16, 2784–2790 (2008).

37. H. F. Xuan, W. Jin, J. Ju, Y. P. Wang, M. Zhang, Y. B. Liao, and M. H. Chen, "Hollow-core photonic bandgapfiber polarizer," Opt. Lett., Vol. 33, 845–847 (2008).

38. P. Schiebener, J. Straub, J. M. H. Levelt Sengers, and J. S. Gallagher, "Refractive index of water and steam as function of wavelength, temperature and density," J. Phys. Chem. Ref. Data, Vol. 19, 677–717 (1990).

Chapter 6

Polarization rocking filters in Hi-Bi MNFs

6.1 Introduction

A polarization rocking filter (PRF) is a special grating which generally couples between the two polarizations of a fiber which are guided in the core, and which can be realized by twisting back and forth the principle axis of the polarization maintaining fiber. The realization of the twist depends on the type of the polarization maintaining fiber. Permanent twist deformation of Hi-Bi fiber structure [1-3], changing the photosensitivity [4-6] of the material, or applying acoustic optic waves[7, 8] into the fiber are all effective. In this chapter, PRF based on the Hi-Bi MNF was analyzed theoretically and experimentally, and the application of this PRF as a refractive index sensor was explored.

6.2 Numerical analysis

6.2.1 Principle

A simple case of Šolc filter [9] is considered first as it is straightforward to understand how the two polarization states can be coupled to each other [10]. Fig. 6.1 (a) shows the stack of half wave plates, Fig. 6.1 (b) denotes the rotation of principal axis as a function of the length z. In each section of the half wave plate, the fast and slow waves will have π phase difference in propagation. At each connecting point, the principal axis is rotated $2\theta_m$. The change of the electric field shows that for rocking angle amplitude (peak to peak) $2\theta_m$, the electric field is rotated $4\theta_m$ per period.

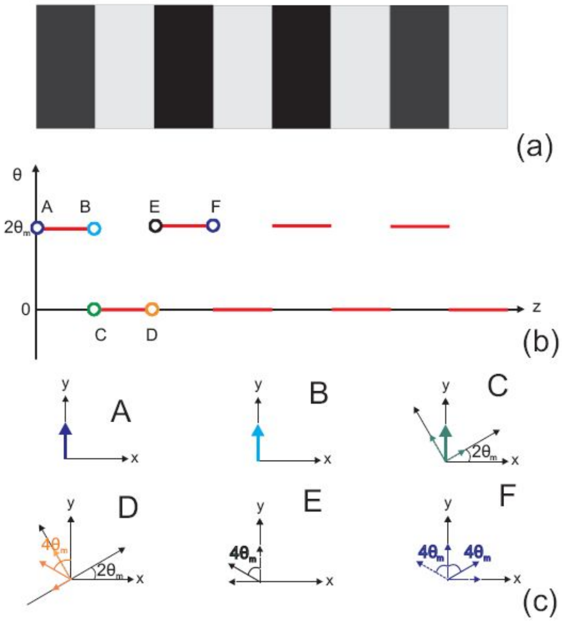

Fig. 6.1: Demonstration of Šolc filter. (a) A series of half wave plates are stacked together alternatively in a periodic way. The Black half wave plates have a rotation angle of 2θm with respect to the grey ones; (b) Angle function as a function of z, the grey ones are defined as 0; (c) Electric field decomposition at each point is designated as A, B, C, D, E and F along the stack [10].

In general, the orthogonal polarization modes of a birefringent medium can be coupled together by twisting the principal polarization axes forth and back periodically with distance [9, 11-17]. When the medium is a polarization maintaining optical fiber, such devices are known as rocking filters. Rocking filters inscribed in Hi-Bi MNFs are attractive because the birefringence can reach values many times higher than in conventional Hi - Bi fiber [1, 4]. This shorter beat-length makes it possible to fabricate more compact rocking filters for the same operating bandwidth [11]. Most of the previous researches have concentrated on using rocking filters as wavelength-selective polarization couplers, which can also act as wavelength filters when combined with polarizers placed at both input and output ports, for Hi-Bi

MNFs, it can be function as the basic elements in micro–nano photonics and sensors.

6.2.2 Theory of transmission spectra for rocking filters

The PRFs fabricated with different techniques may have different angular profiles $\theta(z)$ along the fiber, as shown in Fig. 6.2 [10]. When light propagates along a twist birefringent medium, the electrical field components along the fast and slow principle axes of the medium can be represented by the coupled differential equations [18, 19]:

$$\frac{dE(z)}{dz}=\frac{d}{dz}\begin{bmatrix}E_f(z)\\E_s(z)\end{bmatrix}=\begin{bmatrix}i\beta_f & (1-\rho)\Omega(z)\\-(1+\rho)\Omega(z) & i\beta_s\end{bmatrix}\begin{bmatrix}E_f(z)\\E_s(z)\end{bmatrix} \tag{6.1}$$

where $\Omega(z)=d\theta(z)/dz$ is the angle profile, and β_f and β_s are the propagation constants of the fast and slow modes of the unperturbed medium. The parameter $\rho=(\beta_s-\beta_f)/(\beta_s+\beta_f)$ ensures that power is strictly conserved, and the stress induced photoelastic effect is neglected in this thesis. The electrical field can be described by [10]:

$$E(z)=\begin{bmatrix}E_f(z)\\E_s(z)\end{bmatrix}=\begin{bmatrix}\exp(i\beta_f z) & 0\\0 & \exp(i\beta_s z)\end{bmatrix}\begin{bmatrix}e_f(z)\\e_s(z)\end{bmatrix}=m_p(z)\cdot e(z) \tag{6.2}$$

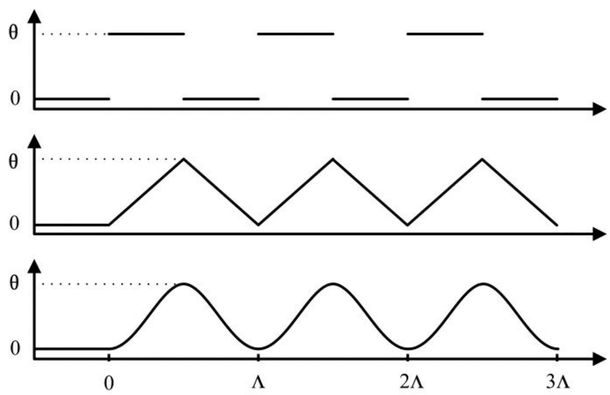

Fig. 6.2 Examples of rocking angle profiles.

By combining Eq. (6.2) and Eq. (6.1), the evolution of the slowly varying amplitude e(z) can be shown as:

$$\frac{de}{dz}=\frac{d}{dz}\begin{bmatrix} e_f \\ e_s \end{bmatrix}=\begin{bmatrix} 0 & (1-\rho)\Omega(z)\exp(i\Delta\beta z) \\ -(1+\rho)\Omega(z)\exp(-i\Delta\beta z) & 0 \end{bmatrix}\cdot e(z)=m_p(z)\cdot e(z) \tag{6.3}$$

where $\Delta\beta=\beta_s-\beta_f$. Then the transfer matrix M corresponding to propagation from z to z+L can be written as:

$$E(z+L)=M\cdot E(z) \tag{6.4}$$

By dividing the propagation distance L into a large number of thin slices and evaluating the product of the transfer matrices for each slice, the matrix M can be described by:

$$M=m_p(z+L)\cdot\prod_{i=1}^{N}\left(I+m_p(z_i)\Delta z\right)\cdot m_p^*(z) \tag{6.5}$$

where Δz is the slice width, N is the total number of slices (L=NΔz), and I is the identity matrix.

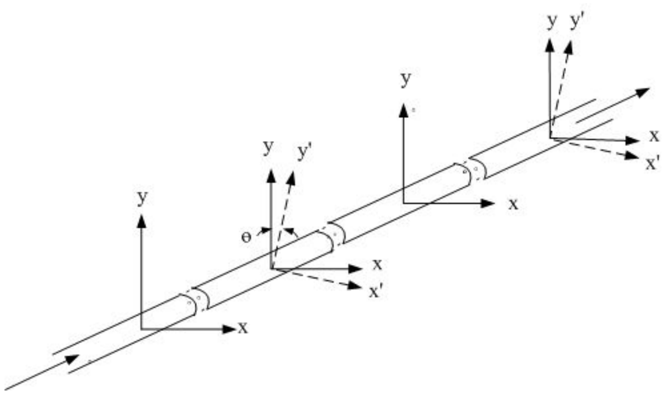

Fig. 6.3 Schematic diagram showing the structure of rocking filter

We now investigate rocking filters inscribed in Hi-Bi MNFs in this thesis, as schematically shown in Fig. 6.3. Coupled mode theory can be used to analyze the behavior of rocking filters with small twist angles. There have been intensive studies reporting on coupled mode theory, and this theory has been used to explain the properties of many kinds of periodic perturbation in fiber structures where two modes are coupled to each other. In this subsection, we used coupled mode theory to describe the PRFs and discuss the properties of the transmission spectra [10].

The electric fields of the two polarization states as a function of propagation length z can be written as follows [9]:

$$E_f = A_f(z)\exp(-i\omega t + i\beta_f z) \tag{6.6}$$

$$E_s = A_s(z)\exp(-i\omega t + i\beta_s z) \tag{6.7}$$

In the equation, $A_f(z)$ and $A_s(z)$ are the amplitudes of the two polarizations respectively. Substituting the two equations into Maxwell equations, we can derive the evolution of the amplitude:

$$\frac{dA_f}{dz} = ikA_s e^{i\delta z} \tag{6.8}$$

$$\frac{dA_s}{dz} = ik^* A_f e^{i\delta z} \tag{6.9}$$

$$\delta = (\beta_f - \beta_s) - \frac{2m\pi}{\Lambda} = 2\pi\left(\frac{1}{L_B} - \frac{m}{\Lambda}\right) \tag{6.10}$$

κ is the average coupling coefficient between the two polarization modes and treated as constant. It is related to the twist embedded in the fiber and is linearly proportional to the twist angle amplitude when the angle is small.

δ represents the phase-mismatch factor between the beat-length L_B and rocking filter period Λ, m=1,2,3, ⋯ ⋯ . When one polarization (fast axis here) is launched into the system and converted to the other mode as traveling in the twisted region with a length *L*, the coupling ratio can be calculated by solving the above equation and the solution is as follows

$$\frac{|A_s(z=L)|^2}{|A_f(z=0)|^2} = \frac{\kappa^2}{\kappa^2 + (\delta/2)^2}\sin^2\left(\sqrt{\kappa^2 + (\delta/2)^2}\,L\right) \tag{6.11}$$

6.2.3 Bandwidth

One feature of the transmission spectrum is the bandwidth of the spectrum. Here we derive the analytical expression for the bandwidth of the transmission spectrum. While first full coupling is realized at resonance, 50% coupling is realized at the place where $\Delta\beta/2\kappa \cong 0.8$ [20]. The expression for bandwidth of the transmission spectrum is derived as follows.

$$\Delta\beta = 2\pi\left(\frac{1}{L_B(\lambda)} - \frac{1}{\Lambda}\right)$$

$$= 2\pi\left(\frac{1}{L_B(\lambda_0)} + \frac{d\left(1/L_B(\lambda)\right)}{d\lambda}\Big|_{\lambda=\lambda_0}(\lambda-\lambda_0) - \frac{1}{\Lambda}\right)$$

$$= 2\pi\frac{d\left(1/L_B(\lambda)\right)}{d\lambda}\Big|_{\lambda=\lambda_0}(\lambda-\lambda_0)$$

$$= \frac{d\left(\Delta n/\lambda\right)}{d\lambda}\Big|_{\lambda=\lambda_0}(\lambda-\lambda_0)$$

$$= \left[-\frac{\Delta n}{\lambda_0^2} + \frac{d\Delta n}{d\lambda}\frac{1}{\lambda}\Big|_{\lambda=\lambda_0}\right](\lambda-\lambda_0) \tag{6.12}$$

$$\Delta\lambda_{3dB} = \frac{0.8}{L}\frac{1}{\dfrac{\Delta n}{\lambda_0^2} - \dfrac{1}{\lambda_0}\dfrac{d\Delta n}{d\lambda}\Big|_{\lambda=\lambda_0}}$$

$$= \frac{0.8\lambda_0^2}{L}\frac{1}{\Delta n - \lambda_0\dfrac{d\Delta n}{d\lambda}\Big|_{\lambda=\lambda_0}}$$

$$= \frac{0.8\lambda_0^2}{LB_g} \tag{6.13}$$

The bandwidth of the rocking filter is parabolicly proportional to the resonance wavelength , and inversely proportional to the device length and group birefringence. Fig. 6.4 gives the simulation results of the hi-bi MNF with parameter mentioned in proceeding chapter. For Fig. 6.4 (a), the pitch of the rocking filter is 240 μm, and the coupled ratio of maximum 1 can be achieved at the same resonant wavelength for different device lengths. The bandwidth is increased as the length decrease. Fig. 6.4 (b) gives the bandwidth as a function of the device length. The fitted curve with a function of $y = a / x$ is consistent with the theory value, indicating that the bandwidth is inversely proportional to the length, which agrees well with the theory analysis.

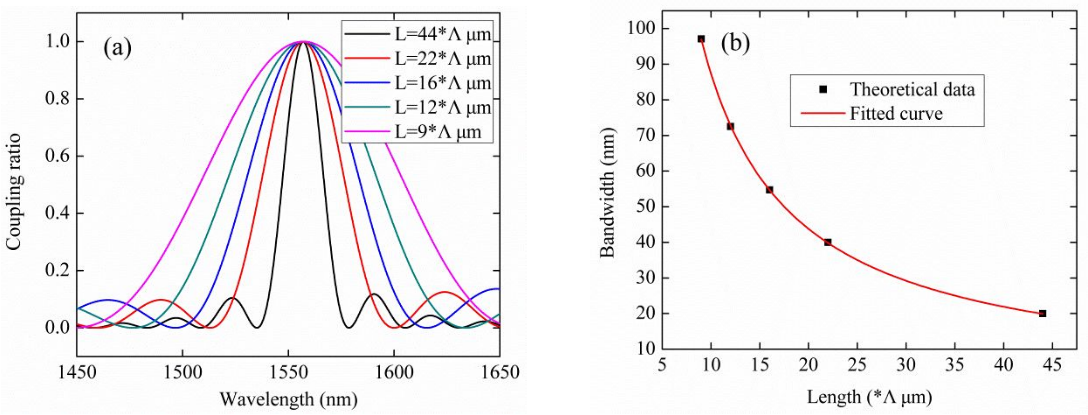

Fig. 6.4 (a) Transmission spectrums for different device length; (b) Bandwidth as a function of length.

The relationship between the resonant wavelength and bandwidth is also studied. The MNFs used in this simulation has the same parameters of the sample H2. These rocking filters have the same device length whereas different pitches and different numbers of periods. The transmission spectra of the rocking filters with different resonant wavelengths are shown in Fig. 6.5 (a). The bandwidth increases when the resonant wavelength is shifted to the longer wavelength and follows a parabola approximation as shown in Fig. 6.5 (b). The black line is the result of the theory simulation, and the red line is a parabola fitted curve. In conclusion, the simulation studies verify the relationship between the bandwidth and the device length and the resonant wavelength.

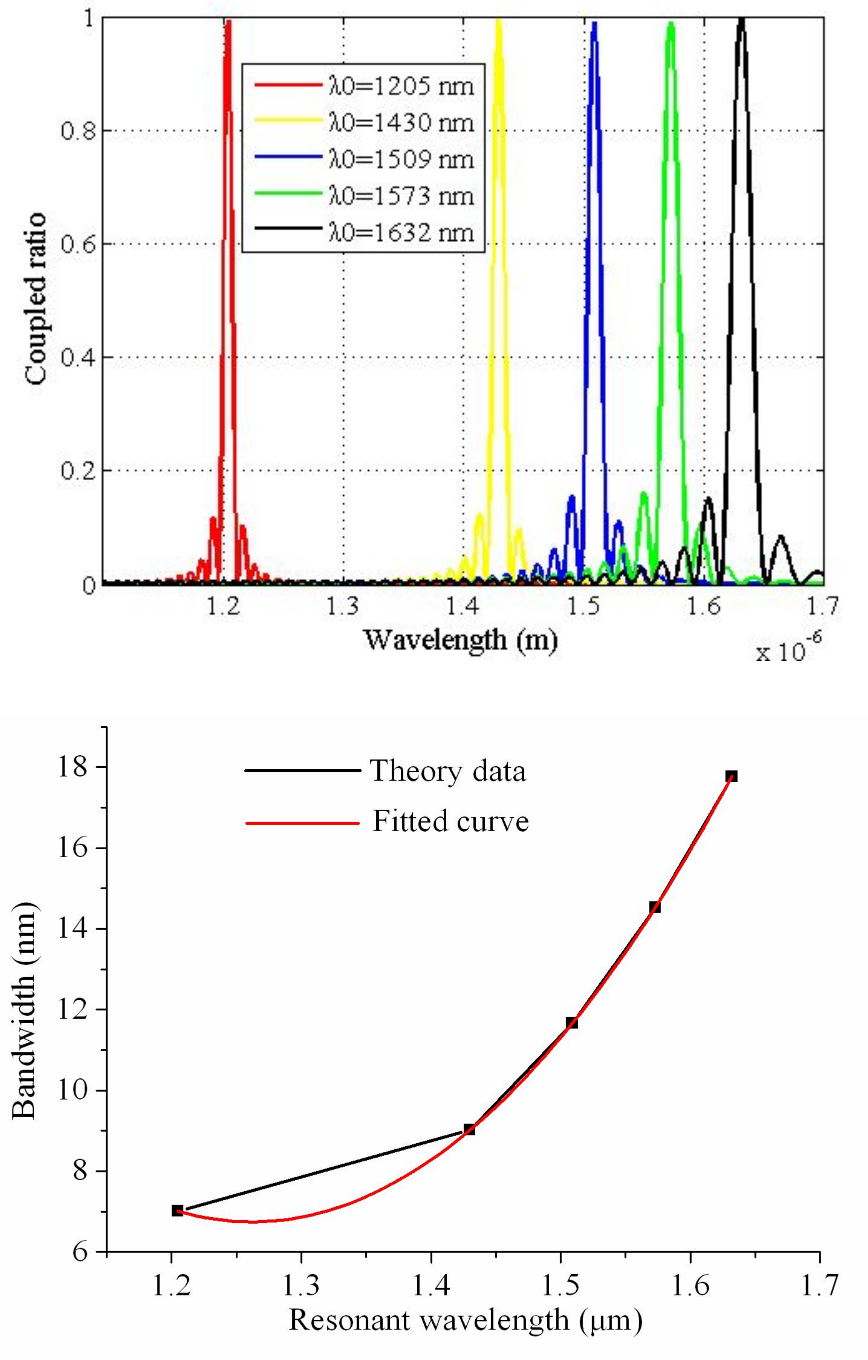

Fig. 6.5 (a) Transmission spectra for different resonant wavelength. (b) Bandwidth as a function of resonant wavelength.

6.2.4 Resonance wavelength and coupling

Fig. 6.6 shows the calculated pitches as functions of wavelength for mode coupling between the two polarization modes.

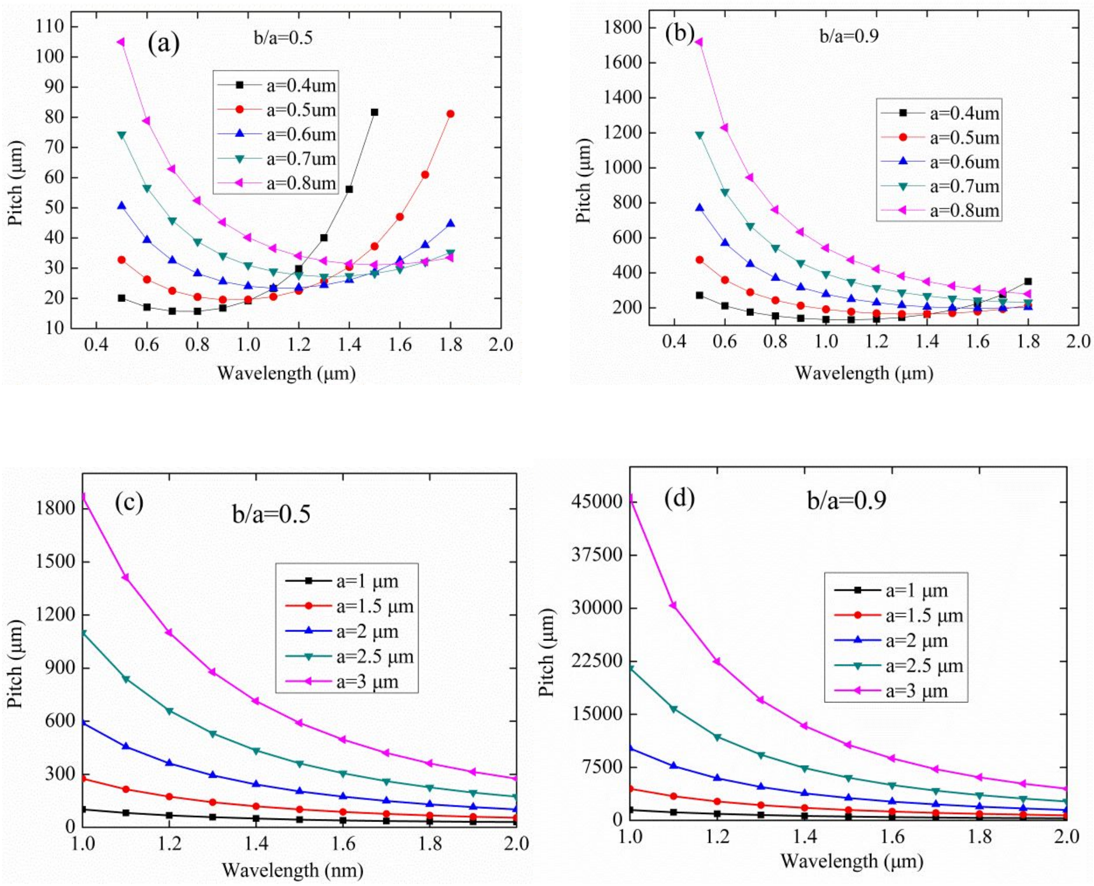

Fig. 6.6 Phase matching curves for for various fiber dimensions and ellipticities. (a) *b/a*=0.5, *a* from 0.4 to 0.8μm; (b) *b/a*=0.9, *a* from 0.4 to 0.8μm; (c) *b/a*=0.5, *a* from 1 to 3 μm; (b) *b/a*=0.9, *a* from 1 to 3 μm.

It is obvious that 100% coupling is only possible when phase-matching condition is satisfied, for the first order coupling that is

$$\delta = \left(\beta_s - \beta_f\right) - \frac{2\pi}{\Lambda} = 0 \tag{6.14}$$

$$\Lambda = \frac{\lambda}{n_{eff,s} - n_{eff,f}} \tag{6.15}$$

where resonance wavelength λ is the optical wavelength at which the phase-matching condition is satisfied, Λ is the pitch, and $n_{eff,s}$ and $n_{eff,f}$ are respectively the effective refractive indices of the fast and slow modes.

Fig. 6.7 shows the coupled ratio as a function of wavelength with different pitch for the Hi-Bi MNFs which has the ellipticities of 0.5 with a=0.4 μm and rocking angle $\theta = 1^{\circ}$. From the figure, we can see that changing the rocking filter period can be used to tune the resonant wavelength in a rocking filter device. At resonance, the power of two polarizations is exchanged between the two polarization states. The first full coupling is realized when $\kappa L = \pi/2$. Coupling is due to the beat between two polarization states, and the beat length determines the length with which full coupling is needed.

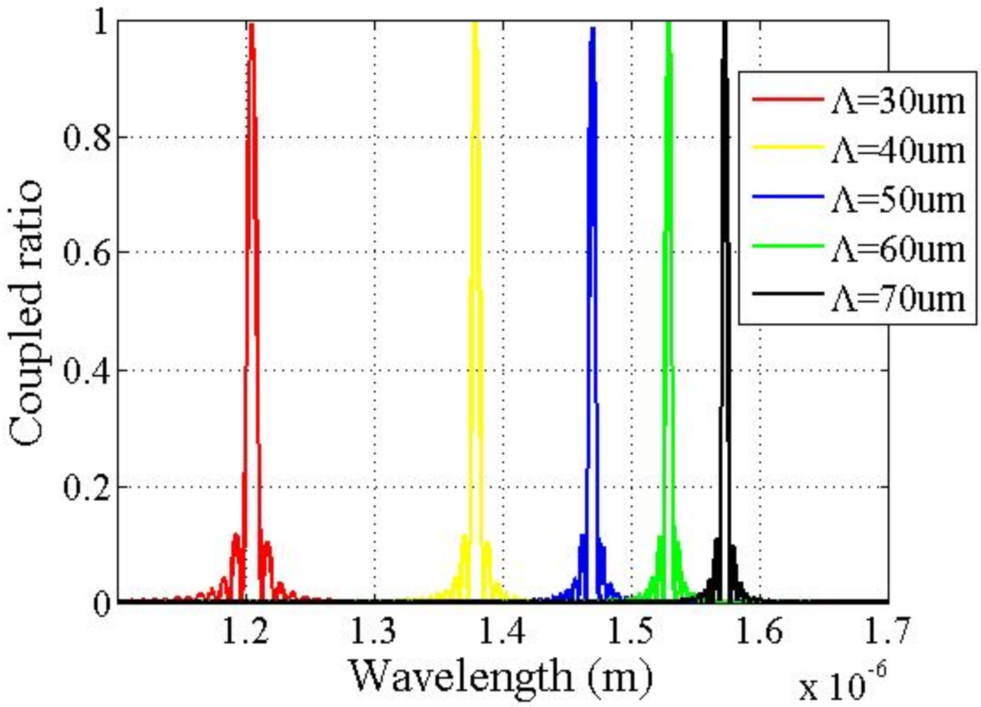

Fig. 6.7 Transmission spectra of the rocking filter in MNFs with various pitches

6.3 Experimental setup for fabricating rocking fibers

PRFs have been fabricated by various techniques, in this dissertation, we use CO_2 laser to induce permanent periodic twist along the fiber. The experimental setup for rocking filter fabrication is shown in Fig. 6.8. A piece of fiber is fixed to two clamps with 12 cm separation between them, one of the clamps is fixed to a motor-driving rotation stage through which twist can be applied to the fiber. Permanent twist can be induced at particular locations along the fiber by heating up the twisted fiber with a CO_2 laser beam. The focused beam can be scanned, via a computer controlled two-dimensional optical scanner, transversely and longitudinally as instructed by a preprogrammed routing.

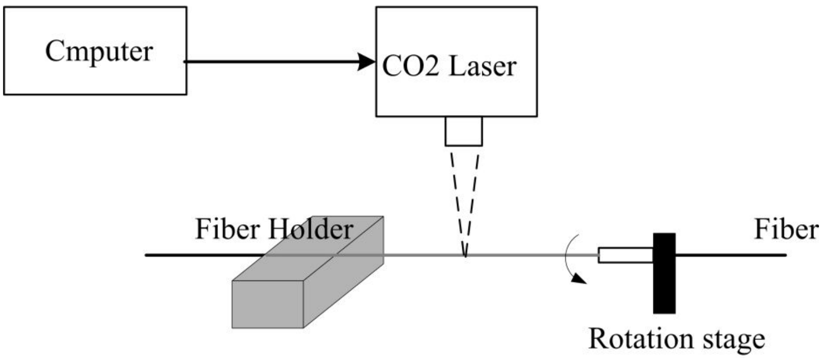

Fig. 6.8 Experimental setup for fabricating rocking fibers.

The fabrication process of the rocking filter may be described as follows: the rotatable motor-driven clamp is firstly rotated by θ, the CO_2 laser beam is then scanned transversely across the fiber, resulting in local heating of the fiber and inducing a permanent twist of the fiber at the heated section. After the fiber is naturally cooled down, the clamp is rotated back by the same angle and the CO_2 laser beam moves longitudinally by a half of the grating pitch (i.e., $\Lambda/2$) along the fiber and performs another transverse scan to produce another permanent twist. This procedure is repeated for 2N+1 times to produce an R-LPG with N periods and a period of Λ. During the fabrication process, the motor rotates back and forth while the CO_2 laser moves along the fiber, there was no hysteresis observed for up to 50 periods. The limitations for the length of the fiber is 15 cm, the period is usually roughly several micrometers, the rocking angle can be quite large as there is no limitation for the rotary motor rotation angle. The rotary motor are from Newport and the precision of the instruments is 0.02° second, and can rotate back and forth automatically controlled by a Labview program, as shown in Fig. 6.9. During the fabrication process, the fiber chuck is fixed at the right position and kept straight.

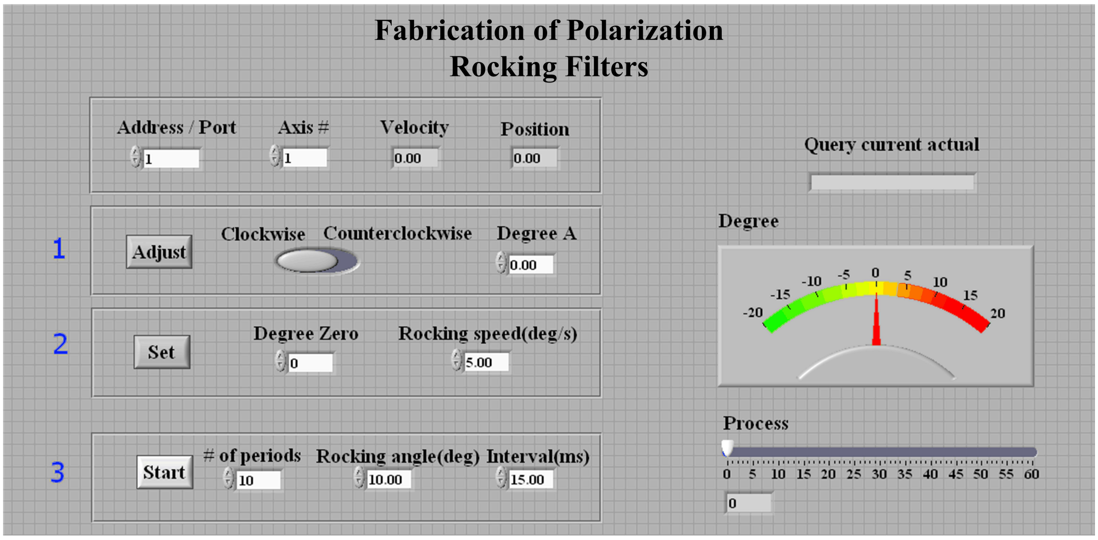

Fig. 6.9 Front panel of the rocking filter fabrication LabVIEW controlling program.

6.4 Fabrication rocking gratings in single mode fibers

In order to identify the angle applied to the fiber, the SMFs samples were initially twisted periodically forth and back, which induced a novel technique to produce rocking long period gratings [20].

The rocking LPG or R-LPG is made by locally heating a twisted fiber with a pulsed CO_2 laser. Permanent twist is induced in a short length of the fiber defined by the spot size of the CO_2 laser beam, which results in a rotation of the cross-sectional plane and induces a large torsion strain. This torsion strain causes changes in the dielectric permittivity, resulting in the mode coupling [21]. We fabricated a 23-period R-LPG with a 2 degree rocking angle and 1.3 mm grating pitch and demonstrated a resonant attenuation of 32.5 dB. The novel R-LPG is found to have a temperature sensitivity of ~88 pm/°C, a strain sensitivity of -0.08 nm/mε, and insensitive to twist. Such LPG structures would have potential applications in optical fiber communication and sensing systems.

6.4.1 Fabrication

A schematic diagram of the experimental setup for fabricating the R-LPG is shown in Fig. 6.8. A piece of SMF is fixed to two clamps, while the input and output ends of the SMF are connected respectively to a broadband light source (BLS) and an optical spectrum analyzer (OSA) to monitor the transmission spectrum. Permanent twist can be induced at particular locations along the fiber by heating up the twisted fiber with a CO_2 laser beam. The CO_2 laser is adjusted to have the following operational parameters: pulse width 450 μs, repetition rate 10 kHz, average power ~0.2 W. The laser beam is focused to a spot of ~ 50 μm in diameter.

During each transverse scanning, the CO_2 laser pulses hit on the fiber and induce a local high temperature to soften the glass. A permanent twist is then induced in the heated region. To show the profile of the R-LPG and measure the effective twist angle, a straight line was carved, before the start of the fabrication process, on the surface along the fiber by a femtosecond IR laser. Figs. 6.10 (a)-(c) show a particular twist profile made by rotating the clamp by 21 degree. This large rotation is intentionally chosen so that the induced permanent twist is clearly seen by visual inspection of the fiber under microscope. Smaller rotation angles are actually used for fabricating LPGs reported in the preceding sections of this paper. A schematic of rocking angle as a function of position along the fiber is given in Fig. 6.10 (d). As shown in Figs. 6.10 (a)-(c), the twist region is about 50 μm long and the separation between the two twists is 420 μm. The actual twist angle was directly measured from the microscopic images and found to be about 7 degree, indicating about 1/3 of the applied rotation is transferred to permanent twists in the CO_2 laser heated regions

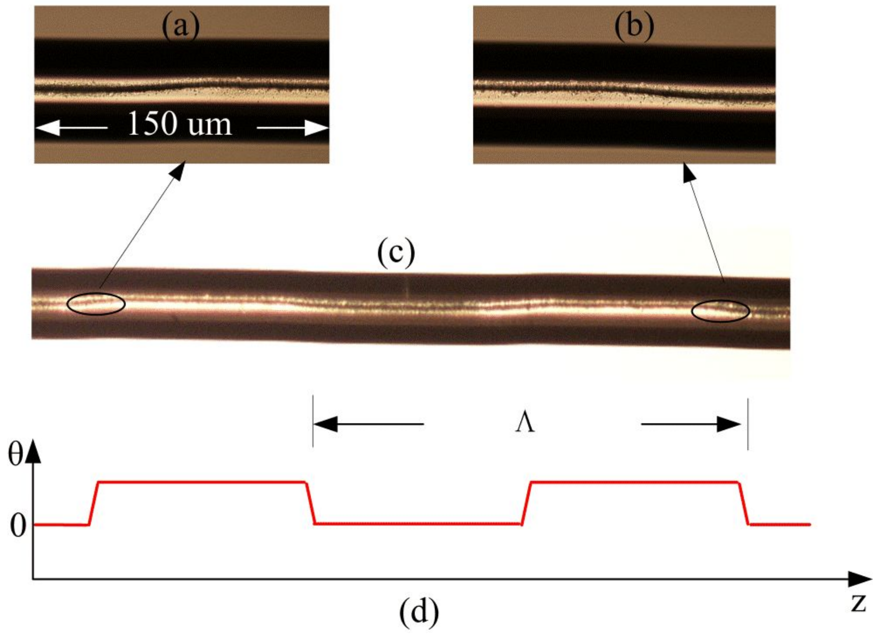

Fig. 6.10 A R-LPG fabricated in a SMF. (a) and (b) microscope images of the CO_2 laser heated regions, (c) side view of showing one grating period, (d) schematic diagram showing the rocking angle as a function of the position along the fiber. The darker line over the fiber core region in (a) to (c) is a maker made on the surface of the fiber cladding, which helps to visualize the induced twist of the fiber.

6.4.2 Transmission spectrum

It should be mentioned that the line carved on the fiber surface serves as a marker to visualize the induced twist along the optical fiber, and this helps us to determine the effective twist angle induced to the fiber. For the R-LPGs described in the following sections, they are fabricated on fibers without any marker carved on the surface. Fig. 6.11 shows the measured transmitted spectrum of a R-LPG made in a SMF with a grating pitch of 1300 μm and 23 periods. The resonance wavelength is 1531.8 nm. The extinction at the resonance is -32.5 dB, corresponding to a peak mode conversion of 99.9%. The insertion loss of the R-LPG is less than ~0.4 dB. The rotation angle of the clamp is 6 degree, and the effective rocking angle is about 2 degree. The mode intensity profile at 1531.8 nm (the inset in Fig. 6.11) suggests that the resonance is probably due to coupling to the LP_{15} mode.

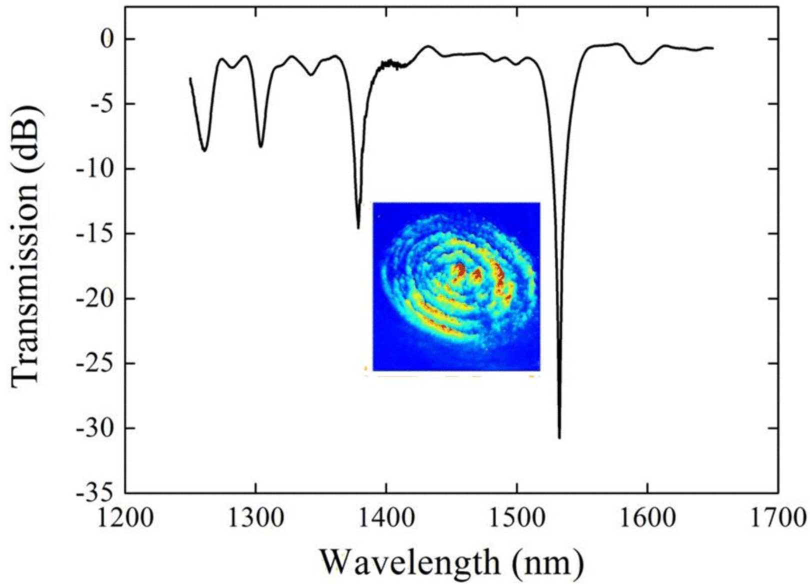

Fig. 6.11 Spectrum of a R-LPG with 2° twist angle and 23 periods .

6.4.3 Theoretical analysis

The mode coupling for the R-LPG may be complex. However, we may intuitively understand the physics by the following a simplified process. In the CO_2 laser irradiation region, twist induces torsion strain, which results in changes in the refractive index or the dielectric permittivity [21]. Since the CO_2 laser is irradiated from one side of the fiber, asymmetric change of permittivity occurs in the cross-section of the CO_2 laser irradiated section. The periodic perturbation of the permittivity along the fiber, according to the well-known coupled-mode theory, results in resonant coupling between the fundamental core mode and higher order cladding modes and forms a LPG.

The perturbation of the dielectric tensor may be written in the form:

$$\vec{\varepsilon}(z) = R(\theta)\begin{pmatrix} \varepsilon_a & 0 \\ 0 & \varepsilon_b \end{pmatrix} R(-\theta) f(z) \tag{6.16}$$

where ε_a and ε_b are respectively the maximum and minimum of the susceptibility ellipsoid in the CO_2 laser irradiated region. ε_a and ε_b are affected by the built-in shear stress, which are mainly determined by the magnitude of the twist applied. θ is an effective twist angle.

$$\mathrm{R}(\theta) = \begin{pmatrix} \cos\theta & -\sin\theta \\ \sin\theta & \cos\theta \end{pmatrix} \tag{6.17}$$

$f(z)$ is a periodic function of z and takes non-zero value only in the CO_2 laser irradiated region. $f(z)$ may be expressed in terms of a Fourier series:

$$f(z) = \sum_{m \neq 0} f_m \exp\left[-im\left(\frac{2\pi}{\Lambda}\right)z\right] \tag{6.18}$$

The induced change in the dielectric tensor may then be expressed as

$$\Delta\varepsilon = \sum_{m \neq 0} \varepsilon_m \begin{pmatrix} -\sin^2\theta & -\sin\theta\cos\theta \\ \sin\theta\cos\theta & \sin^2\theta \end{pmatrix} \exp\left[-im\left(\frac{2\pi}{\Lambda}\right)z\right] \tag{6.19}$$

ε_m is related to ε_a , ε_b and f_m , which are difficult to quantified since the exact distribution of permittivity variation are not known.

The coupled-mode equation for the fundamental core mode may be derived as

$$\begin{pmatrix} \dfrac{\partial A_{co}^H}{\partial z} \\ \dfrac{\partial A_{co}^V}{\partial z} \end{pmatrix} = -iC_m sign(\beta_{co})$$

$$\begin{pmatrix} \sin^2\theta\left\langle E_{co}^H \middle| E_{cl}^H \right\rangle & -\sin\theta\cos\theta\left\langle E_{co}^H \middle| E_{cl}^V \right\rangle \\ \sin\theta\cos\theta\left\langle E_{co}^V \middle| E_{cl}^H \right\rangle & -\sin^2\theta\left\langle E_{co}^V \middle| E_{cl}^V \right\rangle \end{pmatrix}$$

$$\times \begin{pmatrix} A_{cl}^H \\ A_{cl}^V \end{pmatrix} \exp(i(\beta_{co} - \beta_{cl} - m\frac{2\pi}{\Lambda})z) \tag{6.20}$$

where A_i^H and A_i^V are the field amplitude for the horizontal and vertical polarization states, respectively.

$\left\langle E_{co}^H \middle| E_{cl}^H \right\rangle = \iint E_{co}^{H^*} E_{cl}^H dxdy$ is the field overlap integral of the core and the cladding modes, C_m is a coupling coefficient for m-th order grating. When the twist angle θ is small, the term of $\sin^2\theta$ may be neglected, the coupling constant can be expressed

$$\kappa_m = \frac{C_m}{2}\sin 2\theta \iint E_{co}^{V^*} E_{cl}^H dxdy = \frac{C_m}{2}\sin 2\theta \iint E_{co}^{H^*} E_{cl}^V dxdy \tag{6.21}$$

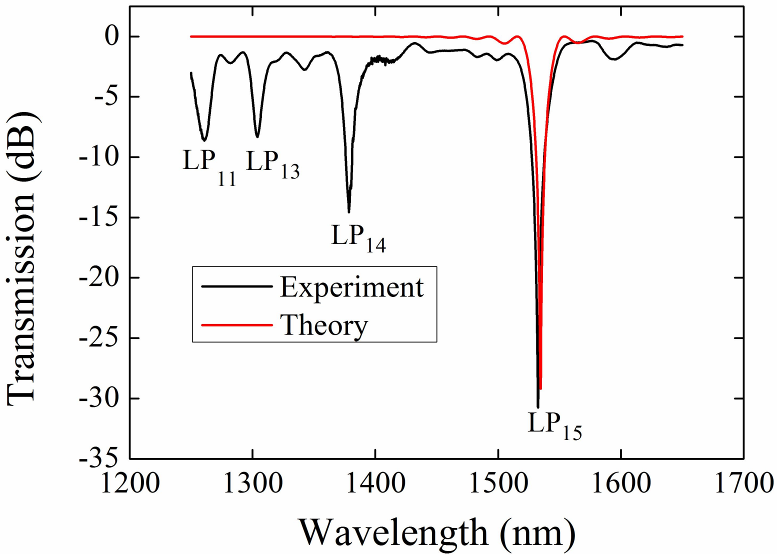

Fig. 6.12 Comparison of calculated and measured transmission spectra of a R-LPG .

By use of the mode index and the field distribution of a standard SMF, C_m as variable fitting parameter, we calculated the transmission of a LPG that couples to the LP_{15} mode, the results are shown in Fig. 6.12. The calculated transmission spectrum agrees well with the experimental results.

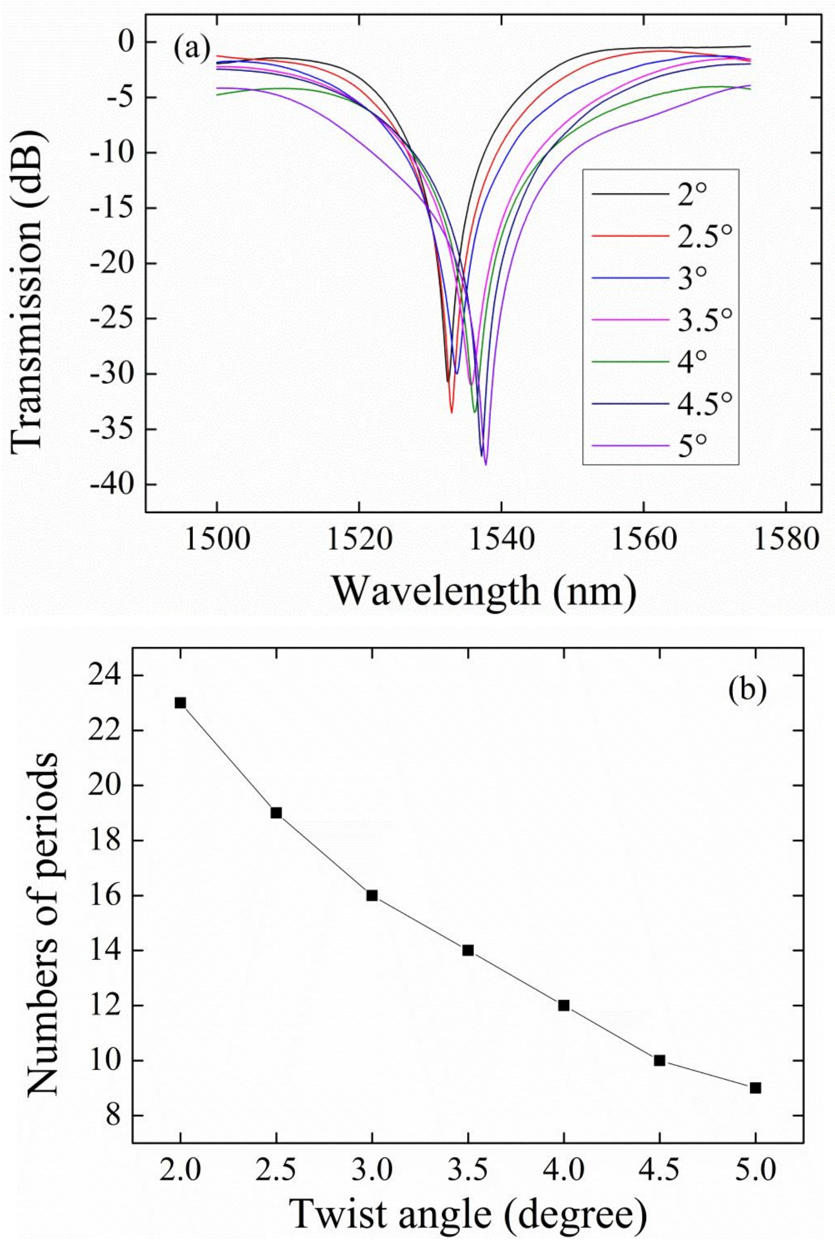

Fig. 6.13 (a) Measured transmission spectra of R-LPGs with different twist angles, (b) the number of periods required to achieve the strongest coupling as function of the twist angle.

From Eq. (6.21), it is seen that the twist angle will affected the coupling constant through $\sin 2\theta$ dependence as well as C_m, which is also affected by θ through the shear stress-induced perturbation of the permittivity. The larger the twist angle, the bigger the induced torsion strain and more change in permittivity. To verify this point, we applied different angles of twist to the fibers, recorded the grating spectra (Fig.6.13 (a)) and the number of grating period required to achieve the strongest coupling to the LP_{15} mode. The number of the required period decreases significantly with the increase of the twist angle as shown in Fig. 6.13 (b). The resonance wavelength shifts slightly toward shorter wavelength with increasing number of grating periods, agreeing with the observation from conventional LPGs [22].

6.4.4 Sensing characterization

To compare the sensing characteristics of the R-LPGs with conventional LPGs, we fabricated a conventional LPG with a similar set of CO_2 laser parameters. The LPG has a period of 650 μm and a length of 29.9 mm (46 periods), the same length with the R-LPG and same number of CO_2 irradiated points. It was found that the efficiency of writing an LPG is much lower compared with a R-LPG, For the R-LPG, the CO_2 laser only needs to scan across the fiber once (one scanning cycle) and the resonant dip is more than 30 dB. However, for the conventional LPGs, after one scanning cycle, the resonant deep is about 0.5 dB. The evolution of the transmission spectrum of the LPG with increasing number of scanning cycles (1st, 30th, and 70th) is shown in Fig. 6.14. After 70 cycles, a resonant dip of -18 dB appeared at the same resonant wavelength of the R-LPG (1529.8 nm). The resonance is also due to coupling to the LP_{15} cladding mode.

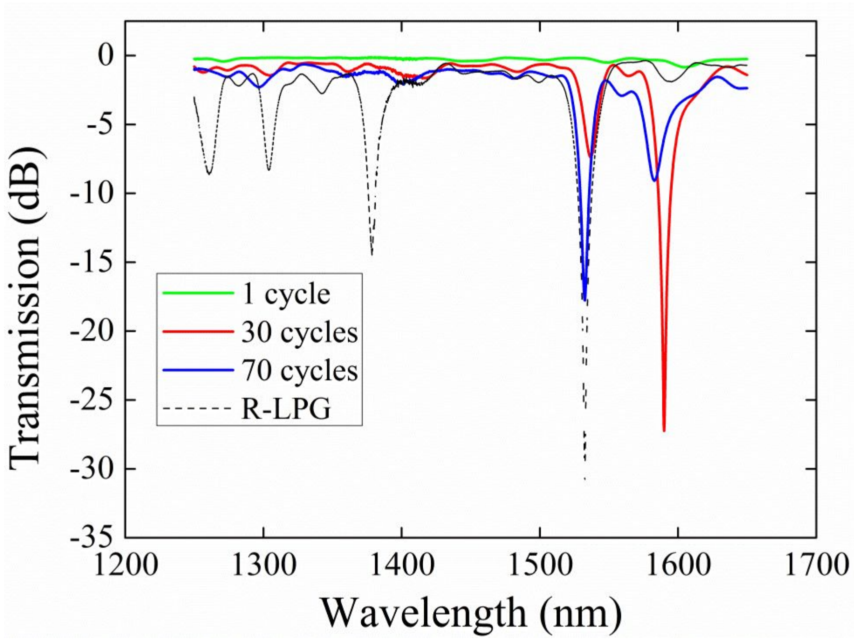

Fig.6.14 Spectrum of a R-LPG and the evolution of a conventional LPG with increasing number of scanning cycles.

6.4.4.1 Temperature measurement

The responses of the R-LPG and the LPG to temperature, longitudinal strain, and twist were tested experimentally. The temperature test was carried out from room temperature (23.2 °C) to 100 °C by putting the gratings into a digitally controlled oven. The variation of transmission spectra of R-LPG is shown in Fig. 6.15 (a). The resonant wavelength shifts toward longer wavelength and follows an approximately linear relationship as shown in Fig. 6.15 (b), corresponding to temperature coefficient of ~ 88 pm/°C, compared with that of ~ 62 pm/°C for the conventional LPG.

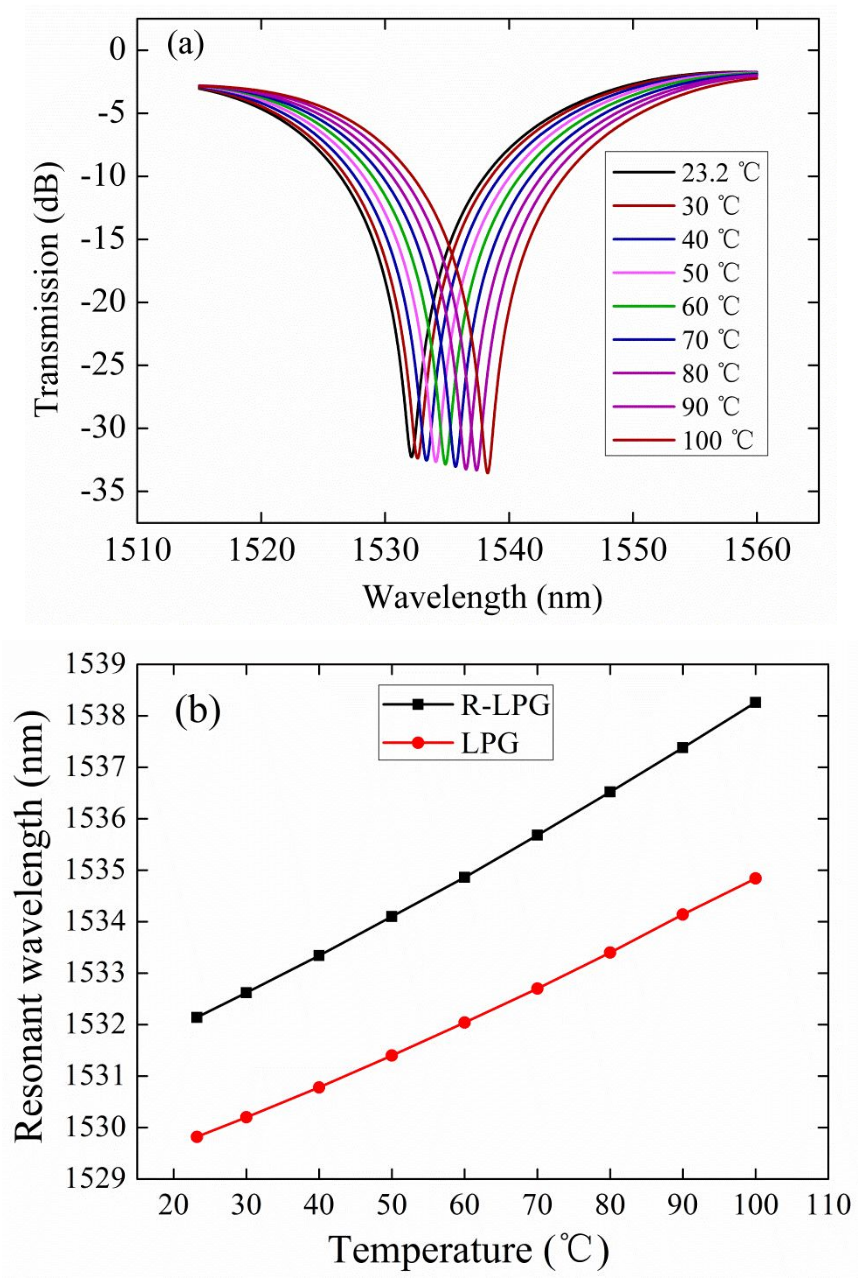

Fig. 6.15 Spectrum evolution of an R-LPG (a) and dip wavelength shifts with the temperature (b) from room temperature to 100 °C.

The high temperature responses of the LPG and the R-LPG were also tested with a higher temperature furnace. Before tests, the two gratings were heated from 23.2 to 800 °C at an average rate of 10 °C/min and pre-annealed at 800 °C for 1 hour. The transmission spectra of gratings at temperatures from 100 to 800 °C are shown in Fig. 6.16 (c), and the shifts of resonant wavelengths with temperature are shown in Fig.

6.16 (d). At higher temperatures, the temperature sensitivity of both gratings increases and the R-LPG is slightly more sensitive than the LPG.

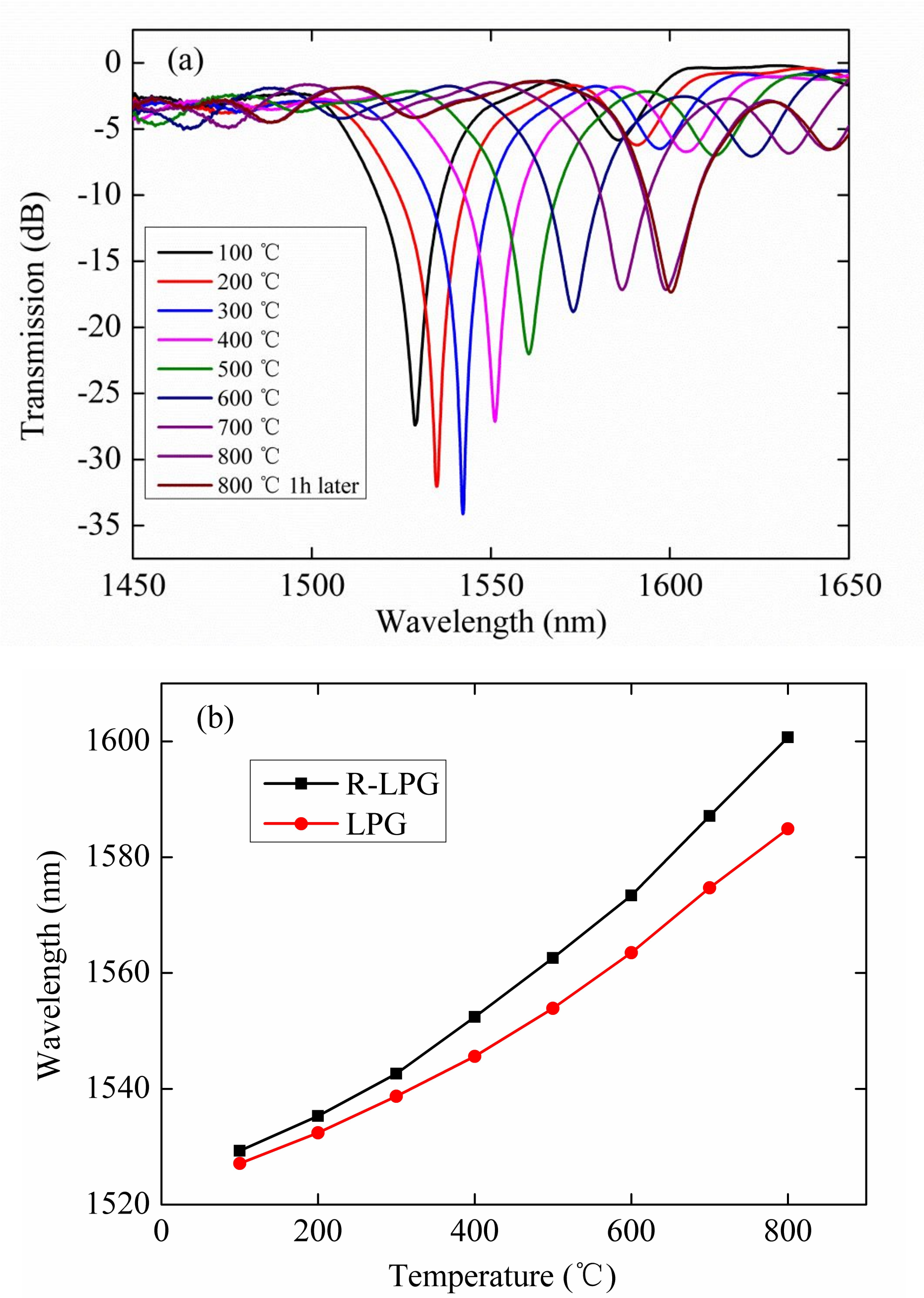

Fig. 6.16 Spectrum evolution of an R-LPG (c) and dip wavelength shifts with the temperature (d) for higher temperature from 100 to 800 °C.

6.4.4.2 Strain sensitivity

The strain test was carried out by fixing the SMF with the R-LPG/LPG on two linear translation stages and then stretching the fiber longitudinally. The separation between two stages is 33 cm, the lengths of the two gratings (R-LPG and LPG) are 2.99 cm. The fibers are stretched in steps of 0.2 mm from 0 to 2 mm at which both gratings broke, indicating the two types of gratings have similar mechanical strength. The measured shift of the resonant wavelength as function of strain is shown in Fig. 6.17. The strain sensitivity of the R-LPG is ~ -0.08 nm/ $m\varepsilon$, about 5 times smaller than the conventional LPG (-0.39 nm/ $m\varepsilon$), which may be because the one scanning induced less deformation on the surface, or the axial strain played the opposite role in the consecutive rotation sections.

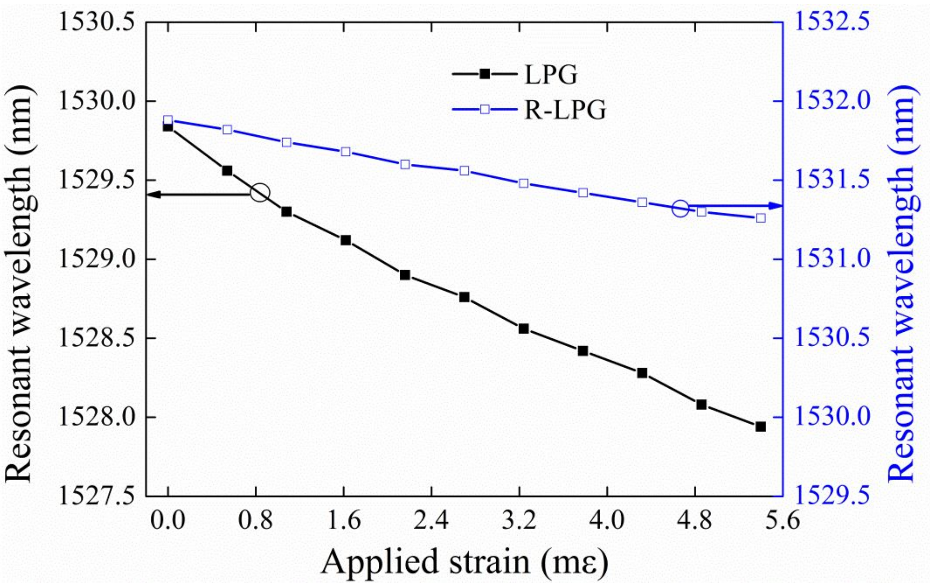

Fig.6.17 Resonant wavelengths of R-LPG and conventional LPF as functions of strain.

6.4.4.3 Twist sensitivity

To study the response of the R-LPG to twist, the two ends of the R-LPG were fixed onto two clamps separated by 130 mm between them, and one of the clamps was fixed to a rotation stage. The applied angle of rotation is from 0 to ±180° with a step of 15°. The R-LPG is insensitive to twist, as shown in Fig. 6.18. This is very different from the conventional LPG, which has a directional twist sensitivity [23] of 0.06 nm/(rad/m). This may be because the codirectional or contradirectional torsion to effectively reduced or enlarged the pitch L, and for one pitch of the R-LPG which includes one codirectional torsion and one contradirectional torsion, the change in the pitch is very small.

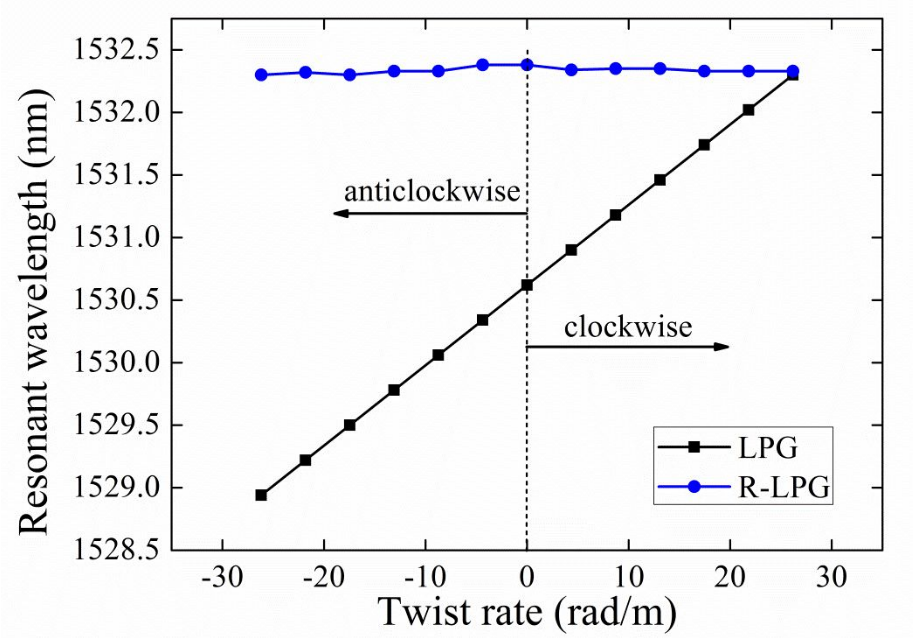

Fig. 6.18 Resonant wavelengths of R-LPG and conventional LPG versus twist rate.

6.4.4.4 Polarization dependent loss

The polarization-dependent loss (PDL) characteristics of R-LPG and LPG were also studied by use of a PDL meter equipped with a tunable laser diode, a motorized polarization controller, and an optical power meter. Since PDL is sensitive to the depth of the attenuation dip [24], we compared the two gratings with similar depths of attenuation dips. Fig. 6.19 shows the measured average loss and PDL results for a R-LPG and a LPG with similar transmission spectra. The maximum PDL is 2.07 dB for the R-LPG, close to that of the conventional LPG (2.45 dB).

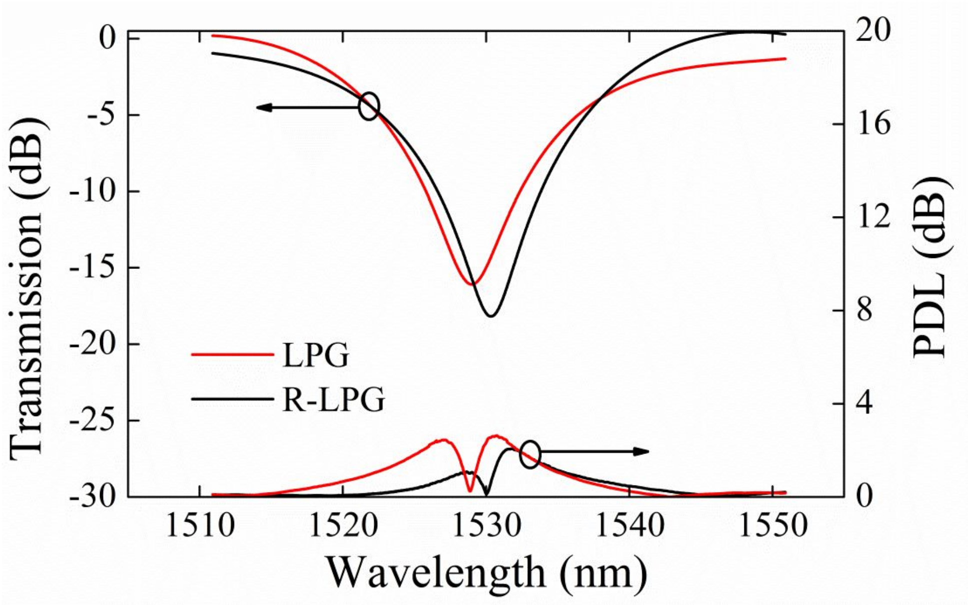

Fig.6.19 Transmission spectra and PDL curves of a R-PFG and a conventional

6.4.5 Summary

A novel type of rocking LPGs was fabricated by scanning a CO_2 laser beam transversely across a SMF while it is being twisted alternatively. Very efficient resonant coupling of 99.96% was achieved for a grating with 23 periods. The response of such R-LPG to temperature, strain and torsion were experimentally investigated. Compared with the conventional LPG made under similar conditions, the resonance dip is found to shift toward longer wavelength with slightly larger temperature sensitivity, and shorter wavelength with a much smaller strain sensitivity, which can effectively reduce the cross sensitivity to temperature. The R-LPG is insensitive to twist.

6.5 Polarization rocking filters in Hi-Bi MNFs

PRFs as a special type of LPGs have been made in Ge-doped D-shaped and elliptical-core polarization-maintaining fibers by photoinducing through an external UV-writing technique, periodic birefringent gratings along the length of the fibers [5, 25]; and in Hi-Bi photonic crystal fibers (PCFs) by periodic twist of the birefringent axis of the fibers through a CO_2 laser-assisted [2] and an arc fusion splicer-assisted technique [3]. The responses of PRFs to strain, temperature, and hydrostatic pressure have been studied [3, 25]. There are also reports on the use of PRFs as polarization-mode couplers to form Mach-Zehnder type fiber interferometers(i.e., in-line polarimeters) for temperature sensors [26], and on simultaneous strain and temperature sensing with a PRF in combination with a fiber Bragg grating(FBG) [27]. A study on the dispersive properties of a PRF in a Hi-Bi PCF was also carried out and shows that the formation of a PRF gives more flexibility in dispersion engineering, which cannot be achieved easily by designing the fiber alone [28]. However, all the PRFs and related devices reported so far are made in normal size optical fibers and there is no report on PRFs made in MNFs to our knowledge.

6.5.1 Fabrication

The Hi-Bi MNF used to fabricate rocking filter had a diameter about 2.8 μm, and the ellipticity of the cross-section is about 0.7, the estimated birefringence is about 0.0065 at the wavelength of 1.55 μm, which gave a beat length as short as 240 μm, and the length of the Hi-Bi MNF with uniform waist is about 2.5 cm. Fig. 6.20 is a schematic diagram of the experimental setup. The fiber was fixed to two clamps with a 8-cm gap between them. One of the clamps rested on the arm of a rotational motor that could oscillate through a fixed angle. The resultant twist was induced at one point along the fiber by the heat generated from a CO_2 laser beam focused onto a spot of ~ 30 μm in diameter. The focused beam can be scanned, via a computer controlled two-dimensional optical scanner, transversely and longitudinally as instructed by a preprogrammed routing.

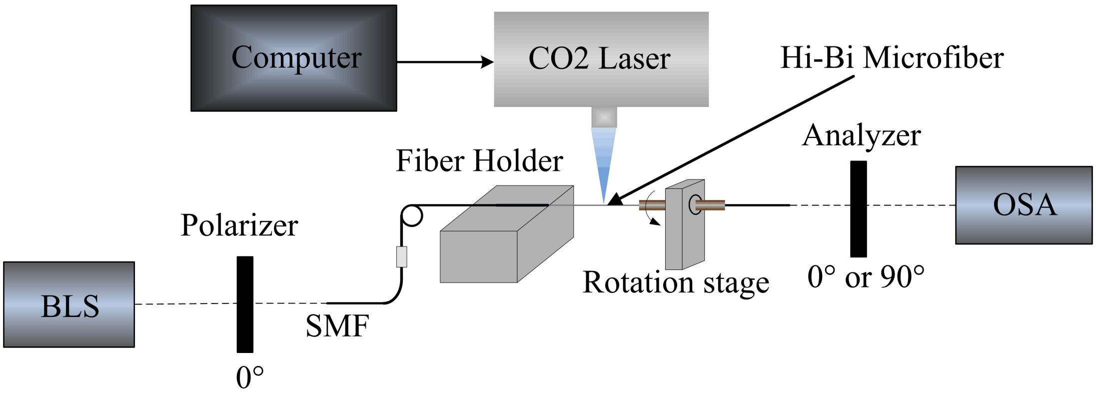

Fig. 6.20 Experimental setup to fabricate PRFs in Hi-Bi MNFs

We measured the transmission spectra of the rocking filters by launching polarized light from a broadband LED source along one of the birefringent axes of the fiber. After passing through a second polarizer which is parallel with the first polarizer, the signal was monitored with an optical spectrum analyzer. Fig. 6.21 shows the transmission spectrum from a rocking filter with 13 periods, each with a length of 240 μm (the length was 3.12 mm). The resonance wavelength was 1556.4 nm, the bandwidth at FWHM was 74 nm, and the measured peak conversion efficiency was 99%, representing 20 dB extinction. The drive rocking angle amplitude was set by the rotation motor to 30 degree, but not all this rotation is taken by the fiber. The rocking angle in radians required for 100% conversion can be determined [6] by the relation $\theta_{effective} = \pi/4N$, where N is the number of rocking periods. Thus, for the rocking filter of Fig. 6.21, the effective twist angle is 3.75°. The loss of 1.8 dB was measured in this way, which may induced by the large twist angle applied in very short pitch.

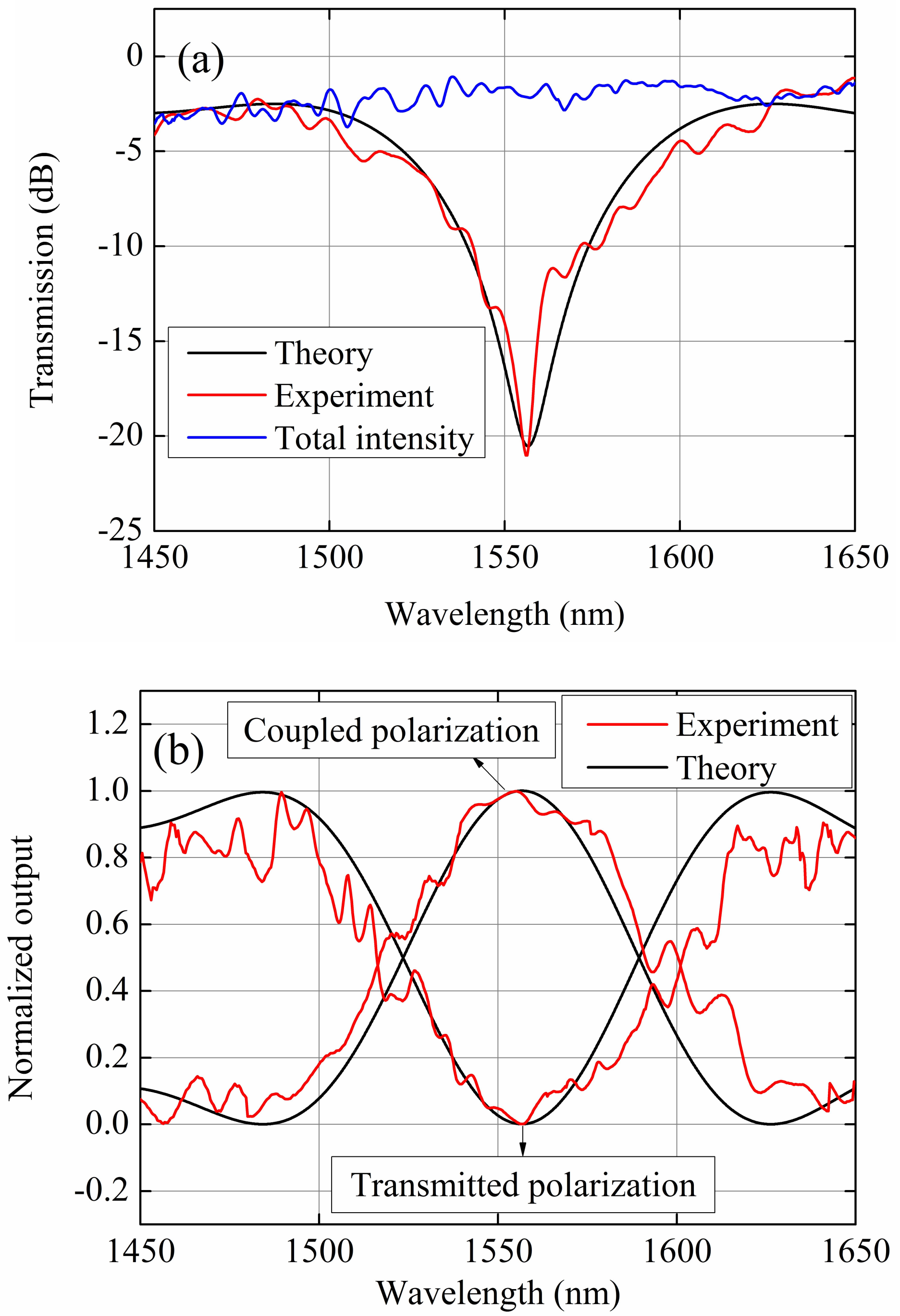

Fig. 6.21 Polarization-coupling spectra for a rocking filter with 3.46° twist angle and 13 coupling periods (a) in the original state of polarization. Red line: experiment, black line: theoretical result. (b) Normalized spectrums of coupled and transmitted polarizations in linear scale. Black lines: theory, red lines: experiment.

The spectrum calculated from Eq. 6.10 with m=1 and θ=3.46° is also shown in Fig. 6.21 (a) with the solid red line. There is excellent agreement between the experimental and the calculated results.

The transmission spectrum was also monitored with m=2, as shown in Fig. 6.22, the period and the rotate angle were set to be 460 μm and 20 degree separately. The resonance wavelength was 1609.3 nm, the bandwidth at FWHM was 21.9 nm, very high coupling efficiency of 32.434 dB (coupling ratio of 99.94%) was achieved with 17 periods and a effective twist angle of 2.6 degree. The loss of <1 dB was typical of filters made in this way.

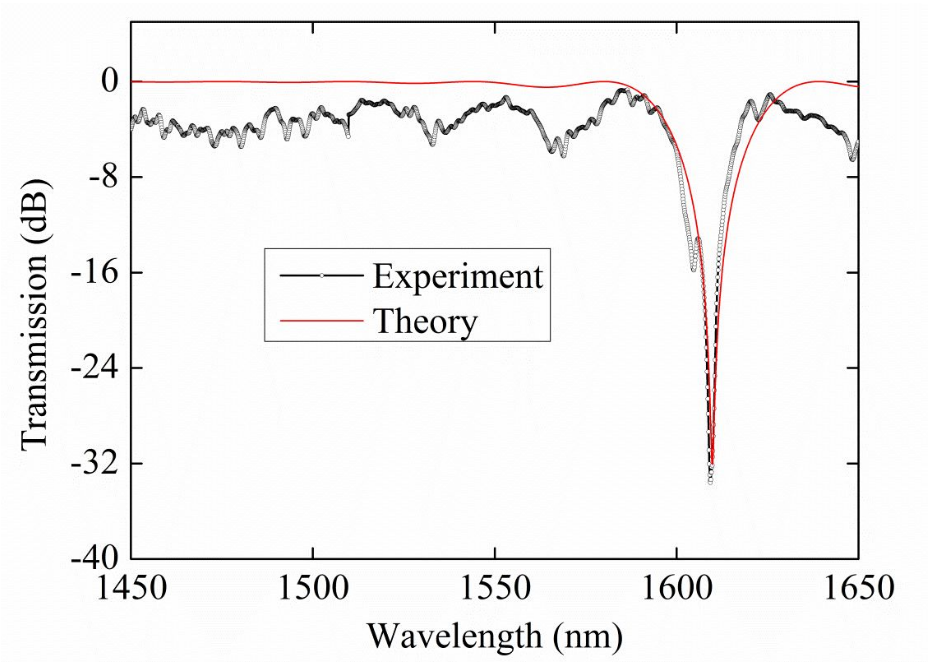

Fig. 6.22 Transmitted spectrum of a 2nd order rocking filter with 2.6° effective twist angle and 17 periods. Black line: measured results, red line : calculated results.

It is evident from the above analysis that the bandwidth can be adjusted by changing the parameter in fabricating the rocking filter, and for Hi-Bi MNF, there is a possibility of high order coupling between the two polarized eigenmodes for Hi-Bi MNF, which allows more flexibility in designing the rocking filters.

6.5.2 Refractive index sensitivity measurement

For the PRFs fabricated in Hi-Bi MNFs, one most important application is for refractive index sensing, whose sensitivity is similar to that of Sagnac loop interferometer with Hi-Bi MNF.

In our experiments, the length and depth of the "cut" region of the "preprocessed" SMF are respectively 22 μm and 3 mm. The Hi-Bi MNF tapers obtained in this investigation has a uniform waist of ~1.7 cm in length, and the major-diameter and cross-sectional ellipticity are respectively ~2.8 μm and ~0.7. At the wavelength of 1.55 μm, the phase birefringence is estimated to be 0.0065, corresponding to a polarization beat length of ~240 μm. Fig. 6.23 shows the phase and group birefringence as well as the polarization beat length as functions of optical wavelength. The group birefringence of this MNF was also measured experimentally by use of a Sagnac loop interferometer as described in above chapter 3, which agrees well with the calculated group birefringence. With the data from Fig. 6.23, we calculated the pitch of PRFs, and the result is shown as the solid blue line.

For the PRF with its transmission spectrum shown in Fig. 6.21, the resonance dips however disappeared when it was immersed in water. The existence of resonant couplings when the PRF is surrounded by water-like solution is important for a range of chemical and biological applications, however, for the smaller size MNF, it is difficult to achieve the phase-match condition with the small pitches predicted in Fig. 6.23. When the MNF is immersed in water environment (RI>1.3) because of the large change in outer refractive index, it means the birefringence of Hi-Bi MNF will be changed largely, the pitch required by the PRFs will become longer, so the resonance is likely to disappear when the refractive index of the environment surrounded the devices changes. We have realized high-order coupling of PRFs in Hi-Bi MNFs, the coupling resonance of PRFs in Hi-Bi MNF immersed in water may achieved with the longer pitch. We then performed refractive index measurement with the higher order PRFs.

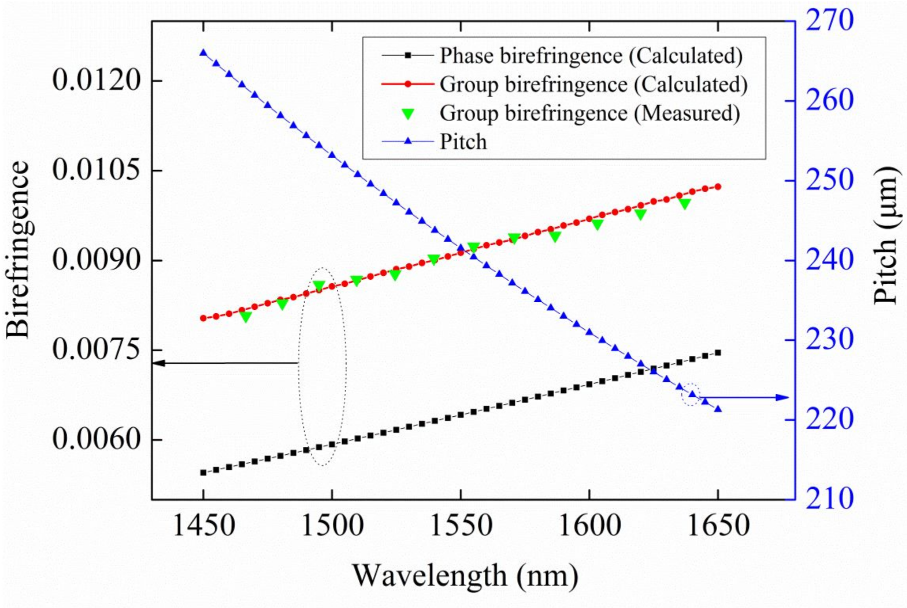

Fig. 6.23 Calculated phase (black line) and group (red line) birefringence, and polarization beat length (blue line) as functions of optical wavelength. The measured group birefringence are shown as the dark yellow point.

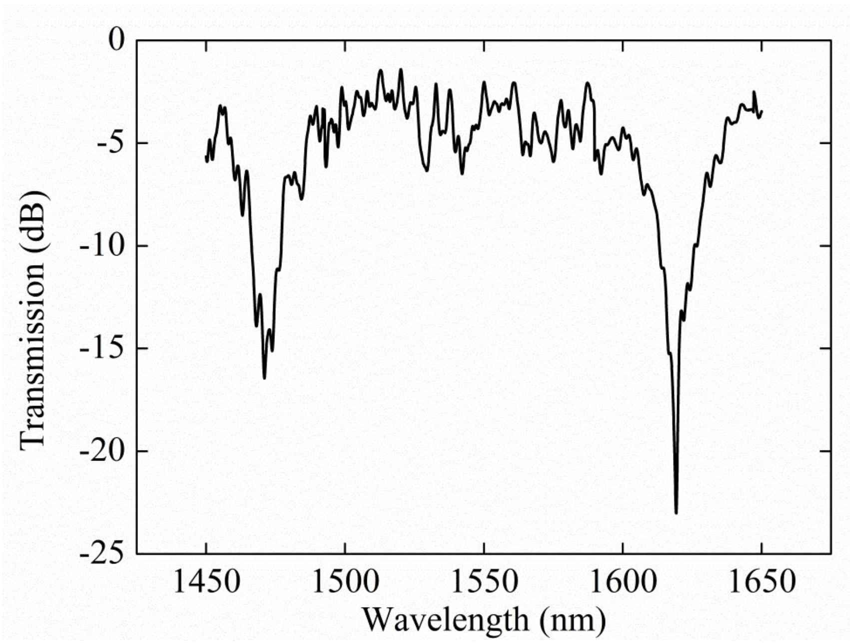

Fig. 6.24 Transmitted spectrum for a high-order PRF with pitch of 1400 µm (in air).

Fig. 6.24 shows the transmitted spectrum of a high order rocking filter in air, made in a MNF with slightly different parameters, the longer pitch required longer uniform Hi-Bi MNF, the tapering parameter need to be adjusted. The rocking period and the applied rotation angle are also changed to 1400 μm and 20 degree respectively. Resonance couplings occur at 1473.8 and 1619.3 nm, respectively, corresponding to probably m=5 or 6. The PRF was then immersed into 1 ml water, the transmission spectrum was changed, shown in black solid line in Fig. 6.25 (a).

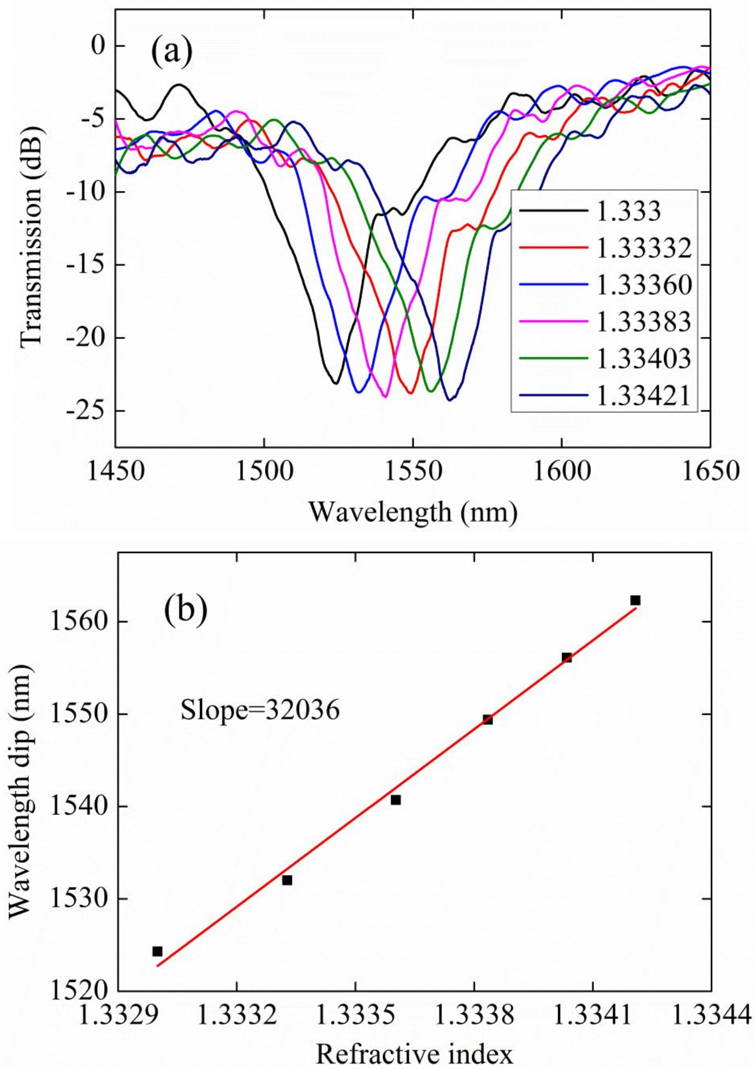

Fig. 6.25 (a) Measured transmission spectra when refractive index is varied from 1.333 to 1.33421. (b) Wavelength of the dip around 1548 nm as function of refractive index.

The response of the device to RI was measured by changed by adding saline solution to water, 0.1 to 0.5 ml of 2% saline solution was subsequently added into the water in step of 0.1 ml. The adding of saline solution changes the refractive index of the solution from 1.333 to 1.33421 [29], and results in a change in the resonant wavelength as shown in Fig. 6.25 (b). A linear relationship between the resonance wavelength and the refractive index is obtained and the refractive index sensitivity is calculated to be 32036 nm/RIU.

6.6 Summary

Rocking filter as a special gratings based on Hi-Bi MNF is analyzed theoretically to study on the coupling properties of the Hi-Bi MNF with different diameters and shapes, which show that the it would be possible to create this in-line devices by exploiting the coupling between the two polarization modes, the pitch can be ranged from tens of micrometers to hundreds of micrometers, compared with PRFs in conventional polarization maintaining fibers and Hi-Bi microstructured fibers, it is more flexible to be designed according to requirements for different applications.

PRFs in Hi-Bi MNFs are realized by inducing permanent twist with scanning a CO_2 laser beam transversely across the MNF while it is being twisted alternatively. A rocking filter with 13 periods, each with a length of 240 μm (the device length was 3.12 mm) was fabricated in Hi-Bi MNF with diameter of 2.8 μm. The resonance wavelength was 1556.4 nm, the bandwidth at FWHM was 74 nm, and the measured peak conversion efficiency was 99%, representing 20 dB extinction. The possibility of higher coupling is also realized and was used as refractive index sensor with sensitivity of 32036 nm/RIU.

References of Chapter 6

1. R. H. Stolen, A. Ashkin, W. Pleibel, and J. M. Dziedzic, ″In‐Line Fiber‐Polarization‐Rocking Rotator and Filter,″ Opt. Lett., Vol. 9, pp. 300‐302 (1984).
2. G. Kakarantzas, A. Ortigosa‐Blanch, T. A. Birks, P. S. Russell, L. Farr, F. Couny, and B. J. Mangan, ″Structural rocking filters in highly birefringent photonic crystal fiber,″ Opt. Lett., Vol. 28, pp. 158‐160 (2003).
3. G. Statkiewicz‐Barabach, A. Anuszkiewicz, W. Urbanczyk, and J. Wojcik, ″Sensing characteristics of rocking filter fabricated in microstructured birefringent fiber using fusion arc splicer,″ Opt. Express, Vol. 16, pp. 17258‐17268 (2008).
4. P. S. Russell, and D. P. Hand, ″Rocking Filter Formation in Photosensitive High Birefringence Optical Fibers,″ Electron. Lett., Vol. 26, pp.1846‐1848 (1990).
5. K. O. Hill, F. Bilodeau, B. Malo, and D. C. Johnson, ″Birefringent Photosensitivity in Monomode Optical Fiber ‐ Application to External Writing of Rocking Filters,″ Electron. Lett., Vol. 27, pp. 1548‐1550 (1991).
6. D. C. Psaila, F. Ouelette, and C. M. deSterke, ″Characterization of photoinduced birefringence change in optical fiber rocking filters,″ Appl. Phys. Letters, Vol. 68, pp. 900‐902 (1996).
7. M. Berwick, C. N. Pannell, P. S. Russell, and D. A. Jackson, ″Demonstration of Birefringent Optical Fiber Frequency Shifter Employing Torsional Acoustic-Waves,″ Electron. Lett., Vol. 27, pp. 713‐715 (1991).
8. K. J. Lee, H. C. Park, H. S. Park, and B. Y. Kim, ″Highly efficient all-fiber tunable polarization filter using torsional acoustic wave,″ Opt. Express, Vol. 15, pp. 12362-12367 (2007).
9. J. W. Evans, ″Solc birefringent filter,″ Journal of Optical Society of America, Vol.

48, pp. 142‐145 (1958).

10. L. T. Zang, “Structural Rocking Filters in Photonic Crystal Fiber,” Friedrich-Alexander-Universität Erlangen-Nürnberg (FAU), (2010).
11. H. Kubota, S. Kawanishi, S. Koyanagi, M. Tanaka, and S. Yamaguchi,″ Absolutely single polarization photonic crystal fiber,″ IEEE Photon. Technol. Lett., Vol. 16, pp. 182‐184 (2004).
12. K. Saitoh, and M. Koshiba, ″Single‐polarization single‐mode photonic crystal fibers,″ IEEE Photon. Technol. Lett., Vol. 15, pp. 1384‐1386 (2003).
13. J. Ju, W. Jin, and M. S. Demokan, ″Design of single‐polarization single‐mode photonic crystal fiber at 1.30 and 1.55 mu m,″ J. Lightwave Technol., Vol. 24, pp. 825‐830 (2006).
14. Y. P. Wang, H. Bartelt, M. Becker, S. Brueckner, J. Bergmann, J. Kobelke, and M. Rothhardt, ″Fiber Bragg grating inscription in pure‐silica and Ge‐doped photonic crystal fibers,″ Appl. Opt., Vol. 48, pp.1963‐1968 (2009).
15. Y. P. Wang, H. Bartelt, W. Ecke, R. Wilisch, J. Kobelke, M. Kautz, S. Brueckner, and M. Rothhardt, ″Sensing properties of fiber Bragg gratings in small‐core Gedoped photonic crystal fibers,″ Optics Communications, Vol. 282, pp. 1129‐1134 (2009).
16. Y. P. Wang, W. Jin, L. Jin, X. L. Tan, H. Bartelt, W. Ecke, K. Moerl, K. Schroeder, R. Spittel, R. Willsch, J. Kobelke, M. Rothhardt, L. Y. Shan, and S. Brueckner, ″Optical switch based on a fluid‐filled photonic crystal fiber Bragg grating,″ Opt. Lett., Vol. 34, pp. 3683‐3685 (2009).
17. T. Geernaert, T. Nasilowski, K. Chah, M. Szpulak, J. Szewski, G. Statkiewicz, J. Wojcik, K. Poturaj, W. Urbanczyk, M. Becker, M. Rothhardt, H. Bartelt, F. Berghmans, and H. Thienpont, ″Fiber Bragg gratings in germanium‐doped highly birefringent microstructured optical fibers,″ IEEE Photon. Technol. Lett., Vol. 20, pp. 554‐556 (2008).

18. P. Mcintyre, and A. W. Snyder, ″Light - Propagation in Twisted Anisotropic Media -Application to Photoreceptors,″ Journal of the Optical Society of America, Vol. 68, pp. 149 - 157 (1978).
19. M. Monerie, and L. Jeunhomme, ″Polarization Mode - Coupling in Long Single -Mode Fibers,″ Optical and Quantum Electronics, Vol. 12, pp. 449 - 461 (1980)
20. W. Jin; H. F. Xuan; W. Jin; L. Jin, "Rocking Long Period Gratings in Single Mode Fibers," *J. Lightwave Technol.,* vol.31, pp.3117-3122, (2013).
21. R. Ulrich and A. Simon, " Polarization optics of twisted single-mode fibers, " Appl. Opt., vol. 18, pp. 2241-2251 (1979).
22. Y. P. Wang, D. N. Wang, W. Jin, Y. J. Rao, and G. D. Peng, "Asymmetric long period fiber gratings fabricated by use of CO_2 laser to carve periodic grooves on the optical fiber, " Appl. Phys. Lett., vol. 89, 151105 (2006).
23. Y. P. Wang, "Review of long period fiber gratings written by CO_2 laser," J. Appl. Phys., vol. 108, 081101 (2010).
24. Gaspar M. Rego, Jose L. Santos, Henrique M. Salgado, "Polarization dependent loss of arc-induced long-period fibre gratings," Optics Communications, vol. 262, pp. 152–156 (2006).
25. R. Kaul, "Pressure sensitivity of rocking filters fabricated in an elliptical-core optical fiber," Opt. Lett., Vol. 20, pp. 1000-1001 (1995).
26. S. E. Kanellopoulos, V. A. Handerek, and A. J. Rogers, "Compact Mach-Zehnder fiber interferometer incorporating photoinduced gratings in elliptical-core fibers," Opt. Lett., Vol. 18, pp. 1013-1015 (1993).
27. S. E. Kanellopoulos, V. A. Handerek, and A. J. Rogers, "Simultaneous strain and temperature sensing employing a photogenerated polarisation coupler and low-order modes in an elliptically cored optical fibre," Electron. Lett., Vol. 30, pp. 1786–1787 (1994).

28. L. Zang, M. Kang, M. Kolesik, M. Scharrer, and P. Russell, "Dispersion of photonic Bloch modes in periodically twisted birefringent media," J. Opt. Soc. Am. B,Vol. 27, pp. 1742-1750 (2010).

29. Topac, Incorporated, “Relationship between salt solution and sugar concentration (Brix) and refractive index at 20°C,” www.topac.com/salinity_brix.html.

Chapter 7

Conclusion and future work

7.1 Conclusion

In this dissertation, we have carried out investigations on Hi-Bi MNFs and their applications in photonic sensors and devices.

The Hi-Bi MNFs are taper-drawn from the standard SMFs that are “pre-processed” by “cutting-away” parts of the silica cladding on opposite sides of the fiber with a femtosecond infrared laser. Such Hi-Bi MNFs have approximately elliptical cross-sections, which generate high birefringence up to 10^{-2}. These Hi-Bi MNFs have SMF pigtails and can be connected with other optical fiber components conveniently with low loss.

The Hi-Bi MNFs are characterized by splicing them into a Sagnac loop interferometer. Theoretical analysis with the Jones Matrix method revealed that the output spectrum of a Sagnac loop interferometer is closely related to the group birefringence of the MNF, which may be determined experimentally by measuring the output spectrum of the Sagnac loop interferometer. The measured values of group birefringence agree well with the calculated results from a FEM program..

Sagnac loop interferometers containing a single section of Hi-Bi MNF and two cascaded Hi-Bi MNFs are demonstrated as comb filters. The use of Hi-Bi MNFs instead of conventional Hi-Bi fibers allows more flexibility in controlling the transmission/reflection characteristics of the Sagnac loop interferometer by adjusting the MNF parameters as well as the refractive index surrounding the MNF**.** The lengths of the Hi-Bi MNFs used are on the order of centimeters, one to two orders of magnitude shorter than the conventional Hi-Bi fiber-based Sagnac loop interferometer devices. These compact devices could be useful for optical signal processing and switching, power equalization, and management for WDM networks.

A simple and effective technique for fabricating in-line photonic microcells with a tapered micro/nano meter-sized core encapsulated within a capillary tube is demonstrated. The encapsulation isolates MNFs from external contamination and prevents the quick degradation of the optical and mechanical properties of the MNFs. Moreover, the photonic microcells can still be filled with gas or liquid phase materials to realize robust photonic devices and sensors via evanescent field interaction. These photonic microcells are proved to be very robust, stable, and feasible for integration into conventional fiber-optic circuits.

By splicing an encapsulated Hi-Bi MNF to a Sagnac loop interferometer system, a gas RI sensor was demonstrated with a RI sensitivity of 2024 nm/RIU. A gas pressure sensor was also demonstrated with a pressure sensitivity of 599 pm/bar, which corresponds to a RI sensitivity of 2285 nm/RIU. When the capillary is filled with water, the RI sensitivity can be as high as 21231 nm/RIU. The ultrahigh RI sensitivity was turned into temperature sensitivity via thermo-optic effect by filling the capillary with a liquid with RI=1.3, and a very high temperature sensitivity of −6.99 nm/°C was demonstrated.

Two important types of in-line mode-coupling devices were fabricated in Hi-Bi MNFs, namely LPGs and PRFs. Coupling between guided modes in MNFs are realized by fabricating LPGs along the MNFs with a CO_2 laser and a femtosecond laser. By inducing periodic micro-tapers along the MNF with a pulsed CO_2-laser in combination with small longitudinal tensile strain applied to the fiber, mode couplings between fundamental mode and higher order mode were achieved. A 25-period LPG exhibits resonance wavelengths of 1445.5 and 1575.6 nm for orthogonal polarization modes, and the corresponding attenuation dips are 12.5 and 20 dB, respectively. The Hi-Bi MNFs with LPGs were encapsulated within capillary tubes, and the transmission spectra of these encapsulated devices remain unchanged for over a month.

LPGs were also fabricated by periodically modifying the surface along one side of a MNF by use of a femtosecond infrared laser to scan through the encapsulated MNF. A 15-period LPG made directly on an encapsulated elliptical Hi-Bi MNF with a major diameter of ~2.8 μm and a grating pitch of 20 μm demonstrated resonant coupling at 1532.7 and 1614.2 nm for the two orthogonal principal polarization states, and the corresponding resonant dips are respectively 19.2 and 15.2 dB. Such an LPG is a truly compact device with a grating length on the order of hundreds of micrometers, and it has small temperature sensitivity. A high order LPG was also made in MNF and demonstrated as a refractive index sensor with the sensitivity of 4623 nm/RIU. These LPGs could be used as MNF wavelength filters, gain equalizers for MNF amplifiers, and wavelength-encoded evanescent-wave biosensors.

MNF-based PRFs were investigated theoretically and experimentally. Theoretically analysis shows that it would be possible to create such devices by exploiting the coupling between the two principal polarization states in a Hi-Bi elliptical MNF. The pitch or rocking period depends on the ellipticity and size of the MNF and ranges from tens of micrometers to hundreds of micrometers. PRFs in a Hi-Bi MNF were fabricated by inducing periodic permanent twist by scanning a CO_2 laser beam transversely across the MNF while it is being twisted alternatively. A PRF was made on a Hi-Bi MNF with a diameter of 2.8 μm, with a period of 240 μm and 13 rocking periods, giving a device length of 3.12 mm. The resonance wavelength of the PRF is 1556.4 nm with a FWHM bandwidth of 74 nm, and the measured peak polarization conversion efficiency is 99%, representing 20 dB polarization extinction. A higher order PRF was also fabricated and used to measure the refractive index change surrounding the PRF, and achieved a RI sensitivity of 32036 nm/RIU around RI=1.33.

7.2 Future work

The in-line photonic microcells made by encapsulating tapered MNFs provide a robust platform to study light-matter interaction via the evanescent field. The potential applications of such photonic microcells are many and further work may be directed along the direction of developing novel photonic devices and sensors based on such photonic microcells. Possible future works include low loss evanescent-wave-coupled optical absorption and florescent cells and photoacoustic cells for chemical and environmental sensors, gain cells for amplifiers in the visible wavelength, and etc.

The in-line mode coupling devices fabricated in Hi-Bi MNFs identifies a direction to use the properties of LPGs and PRFs based on the Hi-Bi MNFs as sensors, filters and so on. We will make further investigation of the effect of fabrication techniques and parameters on the spectral, polarization and other characteristics, aiming to explore more applications of the LPGs and PRFs fabricated in this elliptical waveguide.